Washington University in St. Louis
Washington University Open Scholarship

Arts & Sciences Electronic Theses and Dissertations

Arts & Sciences

Spring 5-15-2020

Identification and Characterization of a Novel Non-homologous End Joining Factor MRI

Putzer Joseph Hung
Washington University in St. Louis

Follow this and additional works at: https://openscholarship.wustl.edu/art_sci_etds

 Part of the Allergy and Immunology Commons, Immunology and Infectious Disease Commons, and the Medical Immunology Commons

Recommended Citation

Hung, Putzer Joseph, "Identification and Characterization of a Novel Non-homologous End Joining Factor MRI" (2020). *Arts & Sciences Electronic Theses and Dissertations*. 2201.
https://openscholarship.wustl.edu/art_sci_etds/2201

This Dissertation is brought to you for free and open access by the Arts & Sciences at Washington University Open Scholarship. It has been accepted for inclusion in Arts & Sciences Electronic Theses and Dissertations by an authorized administrator of Washington University Open Scholarship. For more information, please contact digital@wumail.wustl.edu.

WASHINGTON UNIVERSITY IN ST. LOUIS

Division of Biology and Biomedical Sciences
Immunology

Dissertation Examination Committee:
Barry Sleckman, Chair
Gaya Amarasinghe
Brian Edelson
Takeshi Egawa
Nima Mosammaparast
Kenneth Murphy
Sheila Stewart

Identification and Characterization of a Novel Non-homologous End Joining Factor MRI

by
Putzer Joseph Hung

A dissertation presented to
The Graduate School
of Washington University in
partial fulfillment of the
requirements for the degree
of Doctor of Philosophy

May 2020
St. Louis, Missouri

© 2020, Putzer J. Hung

Table of Contents

List of Figures and Tables

Acknowledgements

Special thanks to my thesis advisor Dr. Barry Sleckman for his mentorship, for inspiring me to think more critically and positively (though I often err too much towards the critical side), and for teaching me enough immunology to realize that I cannot possibly be allergic to alcohol…

I am also grateful to the past and present members of the Sleckman lab, who all helped to catalyze my development as a scientist: Andrea Bredemeyer, Abigail Morales, Anthony Tubbs, Bo-Ruei Chen, Caitlin Purman, Caleb Lieberman, Ian Lamb, Issa Hindi, Jeff Bednarski, Rosmy George, Ryan Irwin, Shruthi Deivasigamani, Yinan Wang, etc.

I would like to thank the members of my committee and all our collaborators, particularly Drs. Gaya Amarasinghe and Nima Mosammaparast, for their invaluable guidance and assistance, without which a lot of the work described here would be possible.

I would also like to thank the Medical Scientist Training Program (MSTP) at Washington University for their continuous support and for believing in my potential nine years ago. Funding for these projects had been generously provided by training grants to the MSTP and Department of Pathology and Immunology.

Finally, my deepest gratitude goes to my friends and family, especially my sister Marian and my parents Shu-jean and Wei-Hsiu, who despite their initial reservations about my decision to pursue medicine and science, had always remained my greatest advocates and motivation.

Putzer J. Hung

Washington University in St. Louis

May 2020

List of Abbreviations

γ-H2AX	Gamma-phosphorylated H2AX (at serine 139)
aa	Amino acid
AEJ	Alternative end joining
CE	Coding end
CJ	Coding join
CRISPR	Clustered regularly interspaced short palindromic repeats
CSR	Class-switch recombination
DDR	DNA damage response
DSB	DNA double-strand break
gRNA	Guide RNA
HR	Homologous recombination
IR	Ionizing radiation
KBM	Ku-binding motif
Lig4	DNA ligase 4
MEF	Mouse embryonic fibroblast
MRI	Modulator of retrovirus infection
MRN	Mre11/RAD50/Nbs1 complex
NHEJ	Non-homologous end joining
PAXX	Paralog of XRCC4 and XLF
PCC	Post-cleavage complex
RSS	Recombination signal sequence
SE	Signal end
SJ	Signal join
TdT	Terminal deoxynucleotidyl transferase
XLF	XRCC4-like factor
XLM	XLF-like motif

Abstract of the Dissertation

Identification and Characterization of a Novel Non-homologous End Joining Factor MRI

by

Putzer Hung

Doctor of Philosophy in Biology and Biomedical Sciences

Immunology

Washington University in St. Louis, 2020

Professor Barry Sleckman, Chair

Non-homologous end joining (NHEJ) is the predominant DNA double-strand break (DSB) repair pathway in G1-phase cells. In particular, developing lymphocytes utilize NHEJ to repair physiologic DSBs generated during the processes of antigen receptor gene assembly and class-switch recombination (CSR). Thus, proper regulation of NHEJ is important not only for immune repertoire diversification, but also for the prevention of chromosomal translocations or deletions that can arise from misrepaired DSBs. The XRCC4-like factor (XLF) has been strongly implicated in promoting NHEJ, presumably by tethering broken DNA ends together in a sleeve-like complex, but its necessity appears to be cell context-dependent. While XLF is required for NHEJ in most cell types, it is dispensable for DSB repair in lymphocytes. Recently, it has been discovered that in lymphoid cells, XLF functions redundantly with other DNA damage response (DDR) proteins that were previously thought to play negligible roles in NHEJ, suggesting that novel NHEJ factors could be revealed in the setting of XLF deficiency.

To test this hypothesis, we carried out a genome-wide CRISPR/Cas9 screen in a XLF-deficient pre-B cell-line for proteins that would become essential for DNA end joining during

V(D)J recombination in the absence of XLF. We validated two hits from our screen: *paralog of XRCC4 and XLF* (PAXX), a newly identified NHEJ factor with significant structural homology to XLF, and *modulator of retrovirus infection* (MRI), an uncharacterized small peptide that been reported to bind to the DSB sensor Ku70/Ku80. We find that the combined genetic deficiency of MRI and XLF in mice leads to an embryonic lethal phenotype that is characteristic of defective NHEJ. Furthermore, we show that MRI is intrinsically disordered and interacts with diverse DDR proteins at both its termini to form large, multimeric complexes. MRI rapidly localizes to DSBs, where it promotes the retention of these DDR proteins on chromatin, and loss of MRI results in increased cellular sensitivity to ionizing radiation (IR). We propose that MRI functions as a multivalent adaptor that enhances the avidity of DDR proteins at DSBs to promote NHEJ.

Chapter 1: Introduction

1.1. DNA Repair by Non-homologous End Joining

In both prokaryotic and eukaryotic cells, DNA double-strand breaks (DSBs) are repaired primarily through either one of two competing mechanisms: homologous recombination (HR) or non-homologous end joining (NHEJ). HR utilizes the intact sequence on the sister chromatid as a template for precise repair and thus occurs exclusively during the G2 and S phases, while NHEJ involves the direct ligation of two DNA ends and operates continuously throughout the cell cycle (Lieber MR 2010). Exactly how the choice between HR and NHEJ is made in repairing a DSB is still an open question, but it is generally thought that the outcome is determined by a competition of different DSB sensor proteins at the exposed DNA ends. In this regard, DNA end structure and processing play a major role in dictating repair pathway choice, with relatively intact DNA ends being the preferred substrates for NHEJ and extensively resected single-stranded DNA ends being favored by HR, which uses the 3' overhangs at a DSB to search for homologous sequences on the sister chromatid (Symington LS and Gautier J 2011, Ceccaldi R et al. 2016, Chang HHY et al. 2017). Although considered more mutagenic than HR due to the lack of a template and the use of error-prone polymerases (discussed briefly below), NHEJ is performed with faster kinetics that is essential for preserving genomic stability, notably by suppressing oncogenic chromosomal translocations, and has evolved to become the predominant DSB repair pathway in mammalian cells (Difilippantonio MJ et al. 2000, Mao Z et al. 2008, Chiruvella, K.K. et al. 2013).

NHEJ is initiated by the DSB sensors Ku70 and Ku80, which together form a ring-shaped heterodimer (Ku70/80) that encircles broken DNA ends (Walker JR et al. 2004). The abundance of Ku70/80 in mammalian cells (estimated at ~400,000 molecules per cell), along with its high

affinity for DNA ends ($K_D = 6 \times 10^{-10}$ M), ensures that the complex is rapidly localized to DSBs (Lieber MR 2010, Chang HHY 2017). The binding of Ku70/80 to DNA ends serves not only to physically protect the ends from further resection by nucleases such as Exo1 and CtIP, but also to recruit downstream NHEJ factors to sites of DNA damage (Zhang Y et al. 2007, Clerici M et al. 2008, Zierhut C and Diffley JF 2008, Mimitou EP and Symington LS 2010). Conversely, the affinity of Ku70/80 for single-stranded DNA is poor, making resected DNA ends less efficient targets for NHEJ repair (Dynan WS & Yoo S 1998). Once bound to a DNA end, Ku70/80 adopts a conformational change that allows it to engage a variety of proteins with nuclease, polymerase, kinase, ligase, or DNA end stabilization activities in a flexible order depending on the structure of the DNA end. This adaptability enables NHEJ to process a wide range of substrates, ranging from hairpins to single-stranded overhangs, and generate diverse products that can be potentially beneficial for a biological purpose, such as antigen receptor gene assembly (Lieber MR 2010).

NHEJ repair of blunt DNA ends can be effectively carried out by Ku70/80 and the ligase complex consisting of DNA ligase 4 (Lig4) and XRCC4. Lig4 interacts with Ku80 through a pair of BRCT domains at its C-terminus and with XRCC4 through a short motif situated between the two BRCT domains (Grawunder U et al. 1998, Sibanda BL et al. 2001, Costantini S et al 2007). XRCC4 is a scaffold protein possessing a distinct structure shared by several other NHEJ factors, comprising a N-terminal globular head domain and a C-terminal coiled coil domain that supports homodimerization and binding to Lig4 (Sibanda BL et al. 2001). The precise role of XRCC4 in NHEJ is unclear, but it has been shown to enhance Lig4 protein stability and activity (Grawunder U et al. 1997). Collectively, Ku70/80, Lig4, and XRCC4 are often referred to as the "core NHEJ factors," as they represent the minimal set of proteins required for NHEJ. Indeed, loss of any one of these core factors completely abrogates NHEJ, demonstrated by the fact that mice deficient in

Lig4 or XRCC4 exhibit impaired lymphogenesis and late embryonic lethality resulting from the widespread demise of post-mitotic neurons, which presumably can only rely on NHEJ for DSB repair (though the source of DSBs in these cells remains elusive) (Frank KM et al. 1998, Gao Y et al. 1998, Frank KM et al. 2000).

For the majority of situations, in which the DNA ends are incompatible due to chemical modifications or mismatched overhangs, additional factors are required to mediate NHEJ. In this regard, Ku70/80 can recruit the large serine/threonine protein kinase DNA-PKcs to DSBs, where it undergoes autophosphorylation and activates many downstream effectors in the DNA damage response (DDR) pathway, one of them being the nuclease Artemis (Ma Y et al. 2005, Goodarzi AA et al. 2006, Spagnolo L et al. 2006). Upon phosphorylation by DNA-PKcs, Artemis, which otherwise functions as an exonuclease, gains both 5' and 3' endonuclease activities, enabling it to trim back DNA hairpins and overhangs so that sufficient microhomologies (short sequences of identical nucleotides adjacent to a DSB) can be exposed to allow for base pairing and alignment between two DNA ends prior to joining by Lig4 (Ma Y et al. 2002, Ma Y et al. 2004, Lu H et al. 2006). Although not absolutely necessary for NHEJ, DNA-PKcs/Artemis appear to be involved in the repair of a significant fraction of DSBs (~20-50%) generated by ionizing radiation (IR) and facilitate most of the limited DNA resection that occurs during NHEJ (Riballo E et al. 2004, Kurosawa A et al. 2008, Chang HH et al. 2015, Biehs R et al. 2017). Other nucleases that play a similar role in NHEJ include Mre11, CtIP, Exo1, WRN, and APLF (Biehs R et al. 2017, Chang HHY et al. 2017). Template-dependent and independent nucleotides are added by the error-prone Pol X family of DNA polymerases – consisting of Pol λ, Pol μ, and terminal deoxynucleotidyl transferase (TdT) – to fill in any gaps and create microhomologies for joining (Lieber MR 2010, Chang HHY et al. 2017).

Despite its apparent necessity, DNA resection is tightly constrained during NHEJ due to the presence of end protection proteins, such as Ku70/80, H2AX (a histone variant), and 53BP1, which physically block nuclease activities at DNA ends, and end stabilization proteins, such as XRCC4 and its structural homologs *XRCC4-like factor* (XLF) and *paralog of XRCC4 and XLF* (PAXX), which in part help to align DNA ends and reduce the dependence on microhomologies. XLF, which will be described in further detail later, has been shown to form mobile, sleeve-like complexes with XRCC4 around DSBs that prevent the broken DNA ends from diffusing apart prior to repair (Hammel M et al. 2011, Ropars V et al. 2011, Andres SN et al. 2012, Reid DA et al. 2015, Roy S et al. 2015, Brouwer I et al. 2017). PAXX, a recently identified binding partner of Ku70/80, has been shown to promote the recruitment or retention of other NHEJ components, including XLF and XRCC4, on damaged chromatin (Craxton S et al. 2015, Ochi T et al. 2015, Xing M et al. 2015). However, the loss of XLF or PAXX, unlike XRCC4, only modestly impairs NHEJ, suggesting that XLF and PAXX are required under specific contexts or that other factors can compensate for their functions (Li G et al. 2008). Additionally, the DSB sensor MRN, which consists of Mre11, RAD50, and Nbs1, and the DDR kinase ATM, which is recruited to DSBs by MRN, also participate in stabilizing DNA ends during the NHEJ-mediated repair of RAG DSBs (Bredemeyer AL et al. 2006, Helmink BA et al. 2009). On the other hand, MRN and ATM can concurrently promote HR – MRN through its nuclease activity, and ATM by activating CtIP – showing that proteins in the DDR pathway may possess multiple and sometimes opposing roles (Lamarche BJ et al. 2008, Helmink BA et al. 2011).

Abrogation of NHEJ leads to extreme cellular sensitivity to DNA damage (especially that caused by IR or radiomimetic drugs) and the emergence of a poorly understood third DSB repair mechanism, termed “alternative end joining” (AEJ). It is unclear exactly which proteins carry out

this process and whether AEJ is a bona fide pathway that serves as a "backup" to NHEJ and HR or just a stochastic reaction resulting from the appropriation of other DNA joining factors, such as those involved in base or nucleotide excision repair; another open question is whether AEJ is operational or being actively suppressed in the presence of NHEJ (Boboila C et al. 2012). Early evidence of AEJ came from studies demonstrating that linear plasmid substrates could be joined efficiently, albeit with large terminal deletions of up to hundreds of base pairs, in NHEJ-deficient cells (Boulton SJ and Jackson SP 1996, Kabotyansk EB et al. 1998). Moreover, NHEJ-deficient, p53-null mice (which are viable due to inactivation of the p53-dependent apoptotic pathway) are prone to developing pro-B cell lymphomas that contain over a dozen translocations, most notably between the *IgH* locus and *c-myc* gene (Zhu C et al. 2002). A distinguishing feature of AEJ is the reliance on longer stretches of microhomology, usually in the range of 4-20 nucleotides, thereby necessitating greater lengths of resection and loss of fidelity; by contrast, NHEJ rarely uses more than 4 nucleotides of microhomology (Pan-Hammarstrom Q et al. 2005). AEJ has been strongly implicated as a driver of genomic instability, especially in light of the observation that RAG and AID can generate DSBs at cryptic sites throughout the genome; thus, its mechanism, regulation, and physiologic role, if any, are emerging as topics of special interest in the field of DNA repair (Klein IA et al. 2011, Barlow JH et al. 2013, Qian J et al. 2013, Teng G et al. 2015).

Although HR appears to be the more "failsafe" method, there are several types of DSBs that are repaired exclusively by NHEJ – the most notable examples being the DSBs induced in developing lymphocytes by the RAG endonuclease during V(D)J recombination for assembling antigen receptor genes and by the cytidine deaminase AID during immunoglobulin class-switch recombination (CSR) for diversifying antibody isotypes (Chaudhuri J et al. 2007, Helmink BA and Sleckman BP 2011). However, while AEJ can compensate for NHEJ by repairing up to 50%

of the DSBs produced during CSR, V(D)J end joining is entirely dependent on NHEJ (Frank KM et al. 1998, Gao Y et al. 1998, Yan CT et al. 2007). The reason for this discrepancy is unknown but could perhaps be attributed to RAG DSBs being structurally inaccessible to AEJ factors or to the end protective effects of RAG itself (Corneo B et al. 2007, Gigi V et al. 2013). Nevertheless, this strict requirement makes V(D)J recombination an ideal system by which to study NHEJ in a physiological context.

1.2 V(D)J End Joining

V(D)J recombination is initiated when the RAG endonuclease (a heterodimer composed of RAG-1 and RAG-2) induces DSBs at recombination signal sequences (RSSs) – which consist of a conserved heptamer, 12 or 23-base pair spacer, and nonamer – adjacent to the variable (V), diversity (D), and joining (J) gene segments that collectively encode the antigen receptor variable region (Fugmann SD et al. 2000). RAG cleavage creates two types of DNA ends: a pair of blunt 5'-phosphorylated signal ends (SEs) and a pair of hairpin-sealed coding ends (CEs). Since RAG is only active during G1 (RAG-2 is periodically degraded at the G1-to-S transition stage), repair of RAG DSBs can only occur through NHEJ (Li Z et al. 1996, Jiang H et al. 2005). The ligation of compatible SEs to form signal joins (SJs) represents the simplest case of NHEJ and requires only the core factors Ku70/80, XRCC4, and Lig4 (Helmink BA and Sleckman BP 2011). On the other hand, CEs must first be opened by Artemis, which preferentially nicks the hairpins at the 3' side of the loop, before they can be repaired to yield coding joins (CJs) that ultimately constitute part of the antigen receptor gene (Ma Y et al. 2002). Thus, loss of either DNA-PKcs or Artemis activity in mice and humans results in radiosensitive severe combined immunodeficiency (SCID) due to the inability to mend CEs and complete V(D)J recombination (Gao Y et al. 1998, Rooney

S et al. 2002, Xiao Z et al. 2009). Furthermore, unlike SJs, which are formed with relatively little nucleotide gain or loss, CJs frequently contain random indels due to the addition of palindromic (P) nucleotides that arise from the asymmetric opening of CE hairpins by Artemis as well as the introduction of non-templated (N) nucleotides by the Pol X family of DNA polymerases (most prominently, TdT) following nucleolytic resection (Dudley DD et al. 2005). While the arbitrary nature of this process results in only a third of the rearrangements being in-frame and capable of producing a functional gene, it is critical for the diversification of the antigen receptor repertoire in developing lymphocytes.

The differential requirements for NHEJ repair of SEs and CEs are also evidenced in the setting of ATM deficiency. As aforementioned, ATM is a serine/threonine protein kinase, which, like DNA-PKcs, phosphorylates hundreds of substrates, including H2AX (at serine 139, forming γ-H2AX), 53BP1, CtIP, and the checkpoint kinase Chk2, in response to DNA damage (Matsuoka S et al. 2007). ATM is activated by RAG DSBs and functions in the repair of CEs by promoting their stability within RAG post-cleavage complexes (PCCs) until they can be ligated: in ATM-deficient ($ATM^{-/-}$) pre-B cells, ~10-20% of CEs dissociate from PCCs and are left unrepaired or become aberrantly joined to other loose DNA ends, most frequently nearby SEs, with which they are paired to form nonproductive hybrid joins (HJ) (Bredemeyer AL et al. 2006, Huang CY et al. 2007). In line with these observations, $ATM^{-/-}$ mice exhibit lymphopenia and a predisposition for thymic lymphomas with RAG-dependent translocations of the T cell receptor loci (Liao MJ and Van Dyke T 1999, Liyanage M et al. 2000, Petiniot LK et al. 2000). Conversely, SJ formation is unimpaired in $ATM^{-/-}$ pre-B cells, suggesting that other factors can compensate for ATM activity at SEs (Bredemeyer AL et al. 2006). In this regard, RAG has been shown to bind avidly to SEs following cleavage in vitro and could play a similar role during V(D)J recombination that makes

ATM stabilization dispensable (Agrawal A and Schatz DG 1997, Hiom K and Gellert, M 1998). DNA-PKcs can likewise form synaptic complexes around DSBs that help hold the DNA ends in close proximity, and while the singular deficiency of ATM or DNA-PKcs has minimal effects on SJ generation, the combined loss of both kinases completely abolishes SE repair, indicating that they carry out overlapping functions in V(D)J end joining (DeFazio LG et al. 2002, Gapud EJ et al. 2011, Zha S et al. 2011, Graham TG et al. 2016). As discussed in further detail later, this kind of redundancy appears to be an overarching theme throughout the process of NHEJ. Deficiency of MRN produces a phenotype similar to that of ATM with regards to V(D)J recombination: pre-B cells expressing hypomorphic mutants of Mre11 or Nbs1 exhibit defects in joining CEs but not SEs, even though ATM can still be robustly activated by RAG DSBs in these cells (presumably because low levels of MRN are sufficient to stimulate ATM), implying that MRN contributes to V(D)J end joining in ways independent of its ability to recruit ATM to DSBs (Helmink BA et al. 2009). Indeed, like DNA-PKcs, Mre11 has been implicated in bridging broken DNA ends prior to repair as a dimer (Williams JS et al. 2008).

The ATM substrates H2AX and 53BP1 also participate in V(D)J end joining and appear to be responsible for maintaining the integrity of broken DNA ends (Helmink BA and Sleckman BP 2011). H2AX is phosphorylated across kilobases of chromatin flanking a DSB and functions in part to retain other DDR factors, including MRN, 53BP1, and MDC1, at sites of DNA damage (Fernandez-Capetillo O et al. 2004). *H2AX*$^{-/-}$ mice display growth retardation, male infertility due to impaired spermatogenesis, radiation sensitivity, and reduced immunoglobulin class-switching post-immunization – characteristics suggestive of a defect in DSB repair (Celeste A et al. 2002). *53BP1*$^{-/-}$ mice are phenotypically akin to *H2AX*$^{-/-}$ mice; moreover, loss of 53BP1 nearly abolishes CSR and also compromises the efficiency of rare distal V to (D)J joining events, with unrepaired

CEs being subject to extensive degradation (Ward IM et al. 2003, Manis JP et al. 2004, Ward IM et al. 2004, Difilippantonio S et al. 2008). Although analyses of *H2AX*$^{-/-}$ and *53BP1*$^{-/-}$ pre-B cells did not reveal any ostensible deficits in SE or CE joining, haploinsufficiency of H2AX or 53BP1 in p53-null mice leads to an increased susceptibility to lymphomagenesis instigated by oncogenic V(D)J gene translocations (Bassing CH et al. 2003, Celeste A et al. 2003, Ward IM et al. 2005). This seeming discrepancy can be explained by the possibility that (1) H2AX and 53BP1 perform nonessential supportive functions in NHEJ such that the absence of either protein only modestly raises the chance of misrepair, or (2) H2AX and 53BP1 play essential specialized roles in NHEJ at certain types of DSBs, such as those that need to be joined across long distances during V(D)J recombination and CSR or those that are located within less accessible regions of the genome. In this regard, H2AX has been shown to inhibit CtIP-mediated resection of SEs and CEs in NHEJ-deficient pre-B cells, thereby preventing these ends from being joined through homology-driven AEJ pathways to form anomalous junctions containing large deletions (Helmink BA et al. 2011). The means by which H2AX blocks resection, given that its levels vary widely between 2-25% of the histone H2A pool across different cell types, remains unknown (Rogakou EP et al. 1998).

Two other ATM substrates MDC1 and KAP-1 make less obvious contributions to V(D)J end joining. MDC1 binds directly to γ-H2AX through its tandem C-terminal BRCT domains and positively regulates H2AX phosphorylation, either by retaining ATM/MRN on chromatin or by blocking phosphatase access to H2AX (Stewart GS et al. 2003, Stucki M et al. 2005, Lou et al. 2006). It has been shown in primary mouse lymphocytes that MDC1 is necessary for maintaining a high density of γ-H2AX within compartments of DNA proximal to RAG DSBs (Slavic V et al. 2009). In this regard, the ability of H2AX to inhibit DNA end resection in G1-phase pre-B cells is dependent on the presence of MDC1 (Helmink BA et al. 2011). Together, γ-H2AX and MDC1

recruit the RNF8 and RNF168 E3 ubiquitin ligases, which in turn enlist 53BP1 to sites of DNA damage (Bohgaki M et al. 2013). KAP-1, also known as TRIM28, is a transcriptional repressor that is phosphorylated by ATM at serine 824 in its C-terminus: this action disrupts the interaction between KAP-1 and the nucleosome remodeler CHD3, resulting in the dispersion of CHD3 from DNA and the relaxation of condensed chromatin to enable the efficient repair of DSBs generated within heterochromatic regions of the genome (Ziv Y et al. 2006, Goodarzi AA et al. 2008, Noon AT et al. 2010, Goodarzi AA et al. 2011). Surprisingly, it has also been demonstrated that KAP-1 promotes the resection of DNA ends not protected by H2AX or 53BP1 in G1-phase mouse pre-B cells, suggesting that KAP-1 might function as an inhibitor of NHEJ; however, this activity is abrogated by a single amino acid substitution (proline 548 → alanine) reflecting a polymorphism between primates and other mammals, indicating that significant species-specific variances exist in the regulation of DSB repair (Tubbs AT et al. 2014).

As previously mentioned, RAG has also been implicated in facilitating the joining step of V(D)J recombination. Specifically, the RAG-2 C-terminal "non-core" domain, so named because it is dispensable for RAG endonuclease activity in vitro, helps stabilize RAG PCCs in a manner similar to ATM; consequentially, loss of this domain impairs the ligation of RAG recombination substrates and results in the accumulation of DSBs that persist throughout the cell cycle (Steen SB et al. 1999, Qiu JX et al. 2001, Curry, JD and Schlissel M 2008, Deriano L et al. 2011). Mice expressing core RAG-2 in lieu of the full-length protein (*RAG2*$^{c/c}$) display partial blocks in B and T cell development due to a selective V to (D)J joining defect that also leads to the formation of HJs, and furthermore *RAG2*$^{c/c}$:*p53*$^{-/-}$ mice develop aggressive early-onset thymic lymphomas that harbor clonal translocations involving the antigen receptor loci (Deriano L et al. 2011).

XLF is another key participant in V(D)J end joining, though its exact mechanistic role is

ambiguous and masked by layers of functional redundancy, the details of which are only recently coming into the light of our understanding.

1.3 XLF and its Role in DSB Repair

Originally identified through a yeast two-hybrid screen for XRCC4-interacting factors and through cDNA complementation cloning of the mutated gene in a cohort of radiosensitive SCID patients who concurrently presented with growth retardation and microcephaly (features also seen in hypomorphic Artemis and Lig4 human syndromes), XLF – also known as Cernuous or Nhej1 – is a ~300 amino acid (aa)-long protein that possesses a high degree of structural, but not sequence, homology to its namesake XRCC4 (Ahnesorg P et al. 2006, Buck D et al. 2006). Like XRCC4, XLF consists of a N-terminal globular head domain (aa 1-135), an elongated α-helical stalk ("coiled coil") domain (aa 136-233), and a disordered C-terminal domain (aa 234-299) that contains a distinct patch of conserved basic and hydrophobic aa residues referred to as the "XLF-like motif" (XLM), which is also found in other DSB repair factors, such as WRN and PAXX (Li Y et al. 2008, Grundy GJ et al. 2016). Similarly, XLF tends to homodimerize through interactions between the stalk domains, with aa 125-224 forming the interface (Andres SN et al. 2007, Li Y et al. 2008). The globular head domains of XLF and XRCC4 support their binding to each other: as revealed by crystallography, leucine 115 of XLF fits into a hydrophobic pocket (aa 63-99) on XRCC4 (Li Y et al. 2008). Alternating XLF and XRCC4 dimers can thus be chained together to produce long, helical filaments (Hammel M et al. 2011). Finally, the unstructured C-terminal domain of XLF mediates its binding to DNA (possibly through Ku70/80) and ability to stimulate DSB repair by Lig4/XRCC4 (Andres SN et al. 2007). By itself, XLF can associate with a minimal DNA footprint of 83 base pairs in vitro, and this length requirement is decreased to 65

base pairs when Ku70/80 is added (Lu H et al. 2007, Yano K et al. 2008). A small deletion of the XLF C-terminal region containing the XLM (aa 290-300) completely abrogates XLF localization to DSBs and its interaction with Ku70/80, underscoring the functional importance of this domain (Yano K et al. 2011).

Despite their strong resemblances, the tertiary structures of XLF and XRCC4 diverge in two major ways. First, the angle between the globular head domain and the coiled coil domain in XLF is much larger than that in XRCC4: in XRCC4, these domains are linked at a ~45° angle to each other, whereas in XLF, they form a flattened, elongated surface that could potentially serve as a binding interface with another protein (Andres SN et al. 2011). Second, while the coiled coil domain in XRCC4 exists as a single helix that extends away from the head domain except for a small conformational deviation that constitutes the Lig4-binding site, the XLF stalk is split into three helices, two of which fold back onto the third of the opposing dimer subunit to generate a more compact structure that increases the dimer interface but precludes the binding of Lig4, and consistent with these data, XLF exhibits poor affinity for Lig4 in the absence of XRCC4 in vitro (Andres SN et al. 2011, Menon V and Povirk LF 2017). XLF is also structurally homologous to PAXX, a 204 aa-long NHEJ factor that is composed of a N-terminal globular head domain (aa 1-113) of unknown function that forms a ~45° angle with a homodimerizing single-α helix coiled coil stalk domain (aa 114-145) and a disordered C-terminal domain bearing a XLM (Ochi T et al. 2015, Xing M et al. 2015, Grundy GJ et al. 2016). Likewise, the PAXX coiled coil domain lacks the Lig4-binding site in XRCC4, and the PAXX C-terminal domain mediates its association with Ku70/80 such that the substitution of two conserved residues in the XLM (valine 199 → alanine, phenylalanine 201 → alanine) is sufficient to disrupt this interaction and prevent PAXX from being recruited to DSBs (Ochi T et al. 2015, Xing M et al. 2015). PAXX co-immunoprecipitates

with XLF, suggesting that they can form a single complex by binding to Ku70/80 simultaneously (Xing M et al. 2015).

What is the function of XLF? Currently, the prevailing model proposes that XLF works in tandem with XRCC4 to structurally align DNA ends prior to ligation – a utility that would be particularly useful for the repair of asymmetric DSBs, which require additional processing before they can be fixed and are at risk of diffusing irreversibly apart during the extended "downtime" if not securely held together. In this regard, XLF has been shown to enhance the efficiency of Lig4 in joining both compatible and noncohesive DNA ends by 10- to 150-fold in vitro, depending on the type and the degree of incongruity, with the largest effects being observed for mismatched 3' overhangs and the smallest for 5' blunt ends (Hentges P et al. 2006, Lu H et al. 2007, Tsai CJ et al. 2007). A follow-up study further reported that while the extent to which Lig4 can successfully anneal a pair of DNA overhangs is contingent on the complementarity of the terminal sequences, ligation of the least favorable sequences appeared to benefit the most from the presence of XLF, consistent with the notion that XLF can functionally compensate, or reduce the requirement, for microhomologies in stabilizing DNA ends (Gu J. et al. 2007). Another group also demonstrated, using human whole-cell extracts, that XLF is essential for the NHEJ-mediated repair of complex DSBs harboring chemically modified bases, such as thymine glycol (a frequent byproduct of IR-induced oxidation), which are sterically awkward substrates for Lig4 (Almohaini M et al. 2006). To catalyze the formation of a phosphodiester bond, Lig4 transfers an AMP molecule onto the 5' phosphate of a nucleobase and must undergo a rate-limiting recharging step prior to subsequent reactions. Interestingly, there is evidence that XLF facilitates the re-adenylation of Lig4 in vitro and could enhance the ligation of blunt DNA ends in an ATP-dependent and independent manner (Riballo E et al. 2008). Moreover, XLF can stimulate gap filling by Pol λ and μ during the repair

of non-complementary DNA ends, signifying that its capacity is not merely confined to the direct augmentation of Lig4 activity per se, but rather, involves promoting an optimal setting in which the entire process of NHEJ can be carried out (Akopiants K et al. 2009). Together, these findings support a major role for XLF in maintaining the synapsis of DNA ends that cannot be otherwise aligned by Lig4/XRCC4 or base pairing due to physical constraints.

Structural analyses of XLF largely reinforce this hypothesis. Crystal lattices composed of XLF and XRCC4 reveal that they are assembled into long, left-handed helical filaments and that these filaments can in turn be tethered side-by-side through hydrophobic interactions between the coiled coil domains of XLF and XRCC4 to create cylindrical tertiary complexes which resemble gear cogs, raising the intriguing possibility that two parallel filaments at a DSB can bind to each other and thus bridge the opposing DNA ends (Wu Q et al. 2011, Menon V and Povrik LF 2017). Imaging by super-resolution fluorescent microscopy confirmed that XLF/XRCC4 filaments do indeed accumulate at DSBs and can even adopt multiple dynamic configurations to increase the pairing probability of two DNA ends (Reid DA et al. 2015). Furthermore, a recent study utilizing optical tweezers combined with fluorescent microscopy showed that XLF stimulates the loading of XRCC4 onto DNA and that together they form stable yet highly mobile sleeve-like complexes around DSBs: these complexes are capable of holding the fragments in close proximity and can diffuse rapidly along the length of the DNA, leaving the ends accessible for processing by other repair factors (Brouwer I et al. 2016). Another study, employing single-molecule FRET analysis in *Xenopus* egg extracts, demonstrated that DNA end stabilization during NHEJ occurs in at least two distinct stages: an initial stage that promotes long-range synapsis, mediated by Ku70/80 and DNA-PKcs, and a subsequent stage that promotes short-range synapsis, mediated by DNA-PKcs kinase activity, XLF, and Lig4/XRCC4 (Graham TG et al. 2016). Despite these compelling data,

little has been done to substantiate the mechanistic role of XLF in vivo, and it is conceivable that XLF may possess additional functions independent of its ability to polymerize with XRCC4 in a less artificial biological setting.

Upon its recruitment to a DSB, XLF is phosphorylated at six serine/threonine residues in the C-terminal domain by DNA-PKcs and ATM (serines 132, 203, 245, 251, 263, and threonine 266), though the purpose of these modifications is unclear, as their abolishment (through alanine substitutions) neither impairs XLF binding to DNA nor affects cellular radiosensitivity (York Y et al. 2008). A later study found that mutating all the DNA-PKcs and ATM phosphorylation sites in the C-termini of XLF and XRCC4 simultaneously, but not separately, to the phosphomimetic residue aspartate promotes the dissociation of XLF/XRCC4 complexes from DNA and impedes their ability to bridge DNA ends in vitro; however, these mutations do not influence the repair of DSBs generated within episomal substrates in vivo, casting doubt on the physiological relevance of DNA-PKcs- and ATM-dependent XLF phosphorylation (Normanno D et al. 2017). XLF can also be phosphorylated by Akt, a kinase best known for its role in the mTOR signaling pathway, at threonine 181: in this case, phosphorylation of XLF causes it to dissociate from Lig4/XRCC4 and be retained in the cytoplasm, where it is ubiquitinated for degradation, thereby serving as an inhibitory mechanism on NHEJ (Liu P et al. 2015).

1.4 Functional Redundancy of XLF in V(D)J End Joining

1.4.1 A Lymphocyte-specific Role for XLF?

In spite of its seeming importance as a facilitator of DNA synapsis and end joining, XLF appears to be variably required for NHEJ in vivo, depending on cellular context. Whereas XLF-deficient primary human fibroblasts and XLF-deficient mouse embryonic fibroblasts (MEFs) and

embryonic stem (ES) cells are radiosensitive, contain multiple aberrant chromosomal alterations, and, when ectopically expressing RAG, exhibit a defect in joining both SEs and CEs on episomal substrates (though not to the extent of XRCC4-deficient cells), XLF-deficient mouse pre-B cells are able to carry out V(D)J recombination of episomal and chromosomal substrates as efficiently as wild-type (WT) pre-B cells (Buck D et al. 2006, Zha S et al. 2007, Li G et al. 2008, Vera G et al. 2013). Patients carrying mutations in XLF present with a progressive SCID phenotype that is less severe than that observed in patients with Artemis or Lig4 genetic hypomorphism; sequence analyses of V(D)J recombination substrates in XLF-deficient human fibroblasts revealed close to normal or reduced levels of SJ and CJ formation, but notably, these junctions exhibited little loss of nucleotides (mostly in the range of 5-20 base pairs) as compared to the extensive deletions and long P nucleotides typically found in other NHEJ-deficient settings (Rooney S et al. 2002, Buck D et al. 2006). On the other hand, *XLF*$^{-/-}$ mice are only slightly lymphophenic and display intact lymphoid progenitor compartments in their bone marrows and thymuses, in contrast to Artemis- and DNA-PKcs-deficient SCID mice, which show a severe block at the pro-B and T cell stage of lymphocyte development due to their inability to rearrange the heavy chain loci; moreover, *XLF*$^{-/-}$:*p53*$^{-/-}$ mice die less often from pro-B cell lymphomas caused by RAG-dependent translocations than from thymic lymphomas that arose due to other consequences of p53 deficiency, indicating that V(D)J end joining is relatively unperturbed in *XLF*$^{-/-}$ mouse lymphocytes (Li G et al. 2008). The discrepancy that XLF is necessary for V(D)J end joining in mouse non-lymphoid cells but not in mouse lymphoid cells signifies that there are lymphocyte-specific factors or mechanisms that can functionally compensate for XLF in this regard. Moreover, unlike V(D)J recombination, CSR is reduced in *XLF*$^{-/-}$ mouse B cells (by ~50%), suggesting that the requirement for XLF in NHEJ depends not only on cell type, but also on the nature of the DSB (Li G et al. 2008).

1.4.2 XLF is Functionally Redundant with the ATM Signaling Pathway

The finding that ATM is similarly involved in the stabilization of DNA ends in G1-phase lymphocytes led to the speculation that ATM could, in fact, be the putative "redundant factor." Indeed, *XLF*$^{-/-}$:*ATM*$^{-/-}$ mice exhibit a SCID phenotype, and B cell development in these mice can be rescued by the introduction of germline alleles containing prearranged immunoglobulin heavy and light chain genes, as would be expected for a defect that had occurred during the process of V(D)J recombination; additionally, *XLF*$^{-/-}$:*ATM*$^{-/-}$ pre-B cell-lines are severely impaired in their ability to repair SEs and CEs within chromosomal substrates, and likewise, treating *XLF*$^{-/-}$ pre-B cells with a pharmacological ATM kinase inhibitor strongly suppresses V(D)J end joining (Zha S et al. 2011). XLF/ATM double-deficiency also abolishes CSR in mature B cells and dramatically increases cytogenetic instability in MEFs, implicating a synergistic role for these two proteins in broader aspects of NHEJ (Zha S et al. 2011, Kumar V et al. 2014). Surprisingly, rearrangement of transient episomal substrates is not obstructed in *XLF*$^{-/-}$:*ATM*$^{-/-}$ pre-B cells, indicating that this functional overlap arises specifically in the context of chromatin (Zha S et al. 2011).

In this regard, it has subsequently been shown that XLF also operates redundantly with H2AX and 53BP1, two chromatin-associated targets of ATM. XLF/H2AX double-deficiency in mice leads to early embryonic lethality (before embryonic day 13.5), the cause of which remains to be determined and is likely related to the ATM-independent role of H2AX in post-replicative DSB repair; correspondingly, *XLF*$^{-/-}$:*H2AX*$^{-/-}$ pre-B cells are unable to efficiently carry out V(D)J recombination, though still to a greater degree than *XLF*$^{-/-}$:*ATM*$^{-/-}$ cells (Zha S et al. 2011, Kumar V et al. 2014). Furthermore, while unrepaired SEs and CEs remain largely intact in *XLF*$^{-/-}$:*ATM*$^{-/-}$ pre-B cells, these ends become extensively resected in *XLF*$^{-/-}$:*H2AX*$^{-/-}$ pre-B cells, consistent with

the notion that H2AX helps to protect the integrity of DNA ends, and microhomologies exposed by this resection could conceivably contribute to the limited joining observed in these cells (Zha S et al. 2011). Like *XLF*$^{-/-}$:*ATM*$^{-/-}$ mice, *XLF*$^{-/-}$:*53BP1*$^{-/-}$ mice are born live with a SCID phenotype resulting from a block in lymphopoesis that can be relieved by knocking in a set of preassembled antigen receptor genes, and in contrast to *XLF*$^{-/-}$ and *53BP1*$^{-/-}$ mice, they are prone to developing thymic lymphomas characterized by clonal translocations of the T cell receptor locus; like *XLF*$^{-/-}$:*H2AX*$^{-/-}$ pre-B cells, *XLF*$^{-/-}$:*53BP1*$^{-/-}$ pre-B cells display a profound defect in V(D)J end joining, with unrepaired SEs and CEs being substantially degraded (Liu X et al. 2012, Oksenych V et al. 2012). DNA end resection in *XLF*$^{-/-}$:*H2AX*$^{-/-}$ and *XLF*$^{-/-}$:*53BP1*$^{-/-}$ cells can be inhibited by the use of an ATM kinase inhibitor, indicating that ATM supports opposing activities during DSB repair (Helmink BA et al. 2011, Zha S et al. 2011, Liu X et al. 2012, Oksenych V et al. 2012). How one outcome is established in favor of the other is an important yet unresolved question.

1.4.2 XLF is Functionally Redundant with DNA-PKcs

DNA-PKcs shares numerous substrates with ATM (including H2AX) and has also been implicated in promoting DNA end synapsis at DSBs (DeFazio LG et al. 2002, Spagnolo L et al. 2006, Callen E et al. 2008). Moreover, as aforementioned, while the loss of ATM or DNA-PKcs alone has minimal effect on SE repair, the absence of both kinases abrogates SJ formation and precipitates early prenatal death in mice (Gapud EJ et al. 2011, Zha S et al. 2011). Thus, it came as little surprise when XLF and DNA-PKcs were later discovered to be functionally redundant in V(D)J end joining. *XLF*$^{-/-}$:*DNA-PKcs*$^{-/-}$ mice are viable but produced in sub-Mendelian ratios and perish within a week following birth, whereas *XLF*$^{-/-}$:*Artemis*$^{-/-}$ mice do not exhibit such lethality; in agreement with these findings, SE joining is significantly compromised in *XLF*$^{-/-}$:*DNA-PKcs*$^{-/-}$,

but not *XLF*$^{-/-}$:*Artemis*$^{-/-}$, pre-B cells, and analogously, in *XLF*$^{-/-}$ pre-B cells treated with a DNA-PKcs kinase inhibitor, suggesting that NHEJ relies on DNA-PKcs catalytic activity separate from the stimulation of Artemis (Oksenych V et al. 2013). Interestingly, free CEs are not appreciably degraded in *XLF*$^{-/-}$:*DNA-PKcs*$^{-/-}$, *XLF*$^{-/-}$:*Artemis*$^{-/-}$, and *XLF*$^{-/-}$:*XRCC4*$^{-/-}$ pre-B cells, implying that XLF is not essential for DNA end protection and is functionally distinct from H2AX and 53BP1 (Oksenych V et al. 2013, Kumar V et al. 2015).

1.4.3 XLF is Functionally Redundant with Non-core RAG-2

The non-core domain of RAG-2 has been shown to mediate the formation of stable PCCs that bind loose DNA ends together in a manner similar to the bridging of DSBs by XLF/XRCC4, raising the question of whether these two mechanisms would be functionally redundant (Deriano L et al. 2011, Coussens MA et al. 2013). As reported in a recent study, *XLF*$^{-/-}$:*RAG2*$^{c/c}$ mice are severely lymphopenic due to a block at the pro-B and T cell stage of differentiation; furthermore, *XLF*$^{-/-}$:*RAG2*$^{c/c}$ pre-B cells contain persistent DSBs at their immunoglobulin light chain loci and cannot properly rearrange chromosomally integrated V(D)J recombination substrates, with most of the unrepaired DNA ends undergoing considerable resection (Lescale C et al. 2016). Finally, *XLF*$^{-/-}$:*RAG2*$^{c/c}$:*p53*$^{-/-}$ mice are also characteristically susceptible to developing B cell lymphomas (even more so than *RAG2*$^{c/c}$:*p53*$^{-/-}$ mice) that harbor translocations and amplifications involving the immunoglobulin heavy chain and *c-myc* genes (Lescale C et al. 2016).

1.5 Discovery of Novel NHEJ Factors in the Absence of XLF

How can the functional redundancy between XLF and these DDR factors be explained? Since many of the proteins (ATM, DNA-PKcs, and RAG-2) contribute to DNA end stabilization

like XLF, one possibility is that they all superfluously perform the same general function and can compensate for the loss of one another. In this regard, ATM and DNA-PKcs are also functionally redundant with each other (Gapud EJ et al. 2011, Zha S et al. 2011). However, this model fails to account for H2AX and 53BP1, which are not significantly involved in DSB synapsis, but rather, in preventing the undesired nucleolytic processing of DNA ends. An alternative interpretation is that these proteins execute different functions, from bridging DNA ends to recruiting or retaining other DSB repair factors on chromatin, that cooperatively promote NHEJ: although the loss of a single component may reduce the efficiency of the reaction, NHEJ can still be completed without any observable deficits – it is only when two components are defective that the overall efficiency of NHEJ becomes visibly impaired. For example, in the absence of DNA end alignment by XLF, the kinetics of repair would be slowed, leaving time for nucleases to access the free DNA ends if not for the effects of H2AX and 53BP1. The inhibition of DNA end resection allows NHEJ to be carried out at a diminished rate. Of course, these two possibilities are not mutually exclusive and can be used to explain the interplay of XLF with separate proteins.

Regardless of its underlying nature, this functional redundancy suggests that the roles of many unidentified NHEJ factors might be masked in the presence of XLF. In fact, ATM, DNA-PKcs, H2AX, and 53BP1 were initially thought to participate only in the repair of certain rarely occurring DSBs, as genetic ablation of any one of these proteins did not broadly impair NHEJ: in the context of V(D)J recombination, deficiency of ATM or DNA-PKcs perturbs CE, but not SE, joining, while deficiency of H2AX or 53BP1 has no discernible consequences on either SJ and CJ formation (Helmink BA and Sleckman BP 2012). Yet, in the setting of XLF deficiency, they all become necessary for the repair of SEs and CEs, implicating a more general involvement in NHEJ than previously appreciated. We hypothesized that other NHEJ factors could be revealed

in the absence of XLF and therefore performed a genome-wide CRISPR/Cas9 screen to discover novel proteins that are functionally redundant with XLF in V(D)J end joining. Here, we describe the methodology of our screen and the characterization of a small peptide, named *modulator of retrovirus infection* (MRI), obtained from the assay. We find that MRI is highly disordered and interacts with diverse DDR proteins, including those in the NHEJ and ATM signaling pathways, to promote their retention on damaged chromatin, potentially within a multivalent complex.

Chapter 2: Materials and Methods

Mice: *MRI*$^{+/-}$ were generated by in vitro fertilization using cryopreserved *MRI*$^{-/-}$ sperm obtained from the Knockout Mouse Project (KOMP) Repository based at UC Davis (clone ID: 862138). The PCR primers used for genotyping the *MRI*$^{+}$ allele were: 5'-CCTTTCTTCCTTCCTTTGGG-3' and 5'-CAGGCCAGAGCCCAGTTTG-3'. The PCR primers used for genotyping the *MRI*$^{-}$ allele were 5'-CCTTTCTTCCTTCCTTTGGG-3' and 5'-GTCTGTCCTAGCTTCCTCACTG-3'. Mice were housed in a specific pathogen-free facility at Weill Cornell Medical College, and all animal protocols were approved by the institutional Animal Care and Use Committee.

Cell-line generation and culture conditions: WT (lines M51.1-22 and M63.1-7), *MRI*$^{-/-}$ (lines M66.1-24 and M46.3-19), *XLF*$^{-/-}$ (lines XA3-8-1 and XB1-5-8), and *Lig4*$^{-/-}$ (line B25-3-4) Abl pre-B cells were generated by culturing cells from the bone marrows of 3-5 week-old mice that harbor a Eμ-Bcl2 transgene with the pMSCV-v-abl retrovirus, infecting the stably transformed cells with the retroviral pMSCV-RSS-GFP-INV-Thy1.2 (MGINV) substrate, and selecting for clones that contain single MGINV integrants (Bredemeyer AL et al. 2006, Hung PJ et al. 2017). To induce V(D)J recombination, these cells were treated with 3 μM imatinib (Novartis) for the indicated times at a density of 10^6 cells/mL. For ATM and DNA-PKcs kinase inhibition, the cells were treated with 15 μM KU55933 (Selleckchem) and 5 μM NU7441 (Torcis), respectively, at a density of 10^6 cells/mL.

To generate inducible Cas9 cell-lines, WT and *XLF*$^{-/-}$ Abl pre-B cells were infected with the lentiviral vector pCW-Cas9 (Addgene, #50661), which carries a tetracycline-responsive Cas9 cDNA, and selected in 2 μg/mL puromycin before being sub-cloned by limiting dilution. Clones were treated with 2 μg/mL doxycycline for two days and screened for robust Cas9 expression by

anti-FLAG western blot. To generate *PAXX*$^{-/-}$ and *XLF*$^{-/-}$:*PAXX*$^{-/-}$ Abl pre-B cells, WT and *XLF*$^{-/-}$ Abl pre-B cells containing a single MGINV integrant and expressing high inducible Cas9 levels were transduced with the lentiviral vector pKLV (Addgene, #50946) bearing a gRNA that targets exon 3 of the mouse *PAXX* gene (5'-AGATATCCATTCCCGGTTC-3'). The cells were cultured with 2 µg/mL doxycycline for a week, sorted for BFP expression (a marker for pKLV), and sub-cloned by limiting dilution. Clones were screened for loss of PAXX expression by both western blot and PCR sequencing (using the primers: 5'-GTGAGTAACAGTGCTGGGGATA-3' and 5'-CTAAGGAGGGAGATGTGTGTTA-3'). *XLF*$^{-/-}$:*MRI*$^{-/-}$ Abl pre-B cells were similarly generated from *XLF*$^{-/-}$ Abl pre-B cells with a gRNA that specifically targets exon 3 of the mouse *MRI* gene (5'-GAAATGGTAGACGTGGCAC-3') and assessed for loss of MRI expression by western blot and PCR sequencing (using the primers: 5'-GTGCCCTGCCCCTGGACC-3' and 5'-AAAAACA TGGCTGGAAAGGTGAGG-3').

MRI$^{-/-}$:*PAXX*$^{-/-}$ abl pre-B cells were generated as previously described (Liu X et al. 2017). Briefly, a pair of gRNAs that target sequences flanking the entire mouse *PAXX* gene (gRNA 1: 5'-CTAAGGTGTTCGCTCGGCGG-3'; gRNA 2: 5'-GCAGTTTATTTGACGGAGAA-3') were cloned into the Cas9 vector pX330 (Addgene, #42230) and electroporated into *MRI*$^{-/-}$ Abl pre-B cells using the Nucleofector 2b device (Amaxa Human B Cell Kit, program X-001, Lonza). After four days, the cells were sub-cloned by limiting dilution, and individual clones were screened for deletion of the *PAXX* gene by PCR (using the primers: 5'-ATTGAAGAGCGGCAGATATGT-3' and 5'-AGCCAGAATCAACACAGTAGGT-3') and western blot.

WT (lines SZ and WT-1), *MRI*$^{-/-}$ (lines M61.2 and M61.7), and *XLF*$^{-/-}$ (lines X-SZ and X-AB) MEFs were generated from embryonic day 14.5-15.5 mice and immortalized by transfection with p-BABE-neo-SV50 (Addgene, #1780), after which they were selected in 400 µg/mL G418.

For IR sensitivity assays, MEFs were seeded in 48-well plates at a density of 2,000 cells/well and irradiated using a RS 2000 X-ray Irradiator (Rad Source Technologies), with cell survival being measured after four days by spectrophotometric analysis of PrestoBlue reagent (Thermo Fisher) metabolism according to the manufacturer's instructions.

CRISPR/Cas9-based genetic screen: The screen was carried out using the Yusa gRNA library (Addgene, #50947) according to the rationale presented in Chapter 2 and as previously described (Koike-Yusa H et al. 2014).

In vitro CSR assays: Naive B cells were purified from the spleens of 6-8 week-old mice using CD43 negative selection microbeads (Miltenyi Biotec, #130-090-862). The cells were seeded in 96-well plates at a density of 4 x 10^5 cells/mL and stimulated with either 25 µg/mL LPS (Sigma) or 1 µg/mL anti-CD40 antibody (eBioscience, #16-0402-81) plus 20 ng/mL recombinant mouse interleukin-4 (IL-4) (Peprotech, #214-14) for 3-4 days. For cell proliferation assays, naive B cells were first incubated with 10 µM CFSE (eBioscience, #65-0850-84) at a density of 10^6 cells/mL in 37℃ for 10 minutes, protected from light, and then quenched with fetal bovine serum (FBS) on ice for 10 minutes prior to stimulation with LPS or anti-CD40 and IL-4.

Retroviral cDNA expression: The murine *PAXX* and *MRI* coding sequences were amplified by PCR from the cDNA clones BC029214 and BC000168, respectively and cloned into a retroviral vector pOZ-FH-N downstream of a FLAG-HA tag and between a *XhoI* site and a *NotI* site. After transduction, cells containing the plasmid were sorted by human CD25 expression. To coexpress HA-tagged MRI and FLAG-tagged Ku80 in cells used for sequential immunoprecipitation (IP),

HA-MRI was generated by PCR and cloned into pOZ-FH-N without the FLAG-HA tag, whereas FLAG-Ku80 was cloned into another retroviral vector pBMN, which has a human CD2 marker, as previously described (Jiang W et al. 2015). PAXX and MRI mutant constructs were generated by overlapping PCR using the following primers and cloned into pOZ-FH-N:

$PAXX^{VF}$: 5′-GCCCTCGAGATGGCTCCTCCGTTGTTGTC-3′ and 5’-GCCGCGGCCGCTCA GGTCTCATCAGCGTCTGCACCAGCAGCTGGT-3’.

$MRI^{\Delta N}$: 5’-CCCTCGAGATGACCGCGCCGGTGG-3’ and 5’-TTGCGGCCGCTCAGCTGAAG AAGATTTCACGA-3’

$MRI^{\Delta C}$: 5’-ATGGAAACCCTGAAAAGCAA-3’ and 5’-TTGCGGCCGCTCACTTTTCCTCCT CCGGGCTAC-3’.

$MRI^{\Delta N\Delta C}$: 5’-CCCTCGAGATGACCGCGCCGGTGG-3’ and 5’-TTGCGGCCGCTCACTTTTC CTCCTCCGGGCTAC-3’.

Immunofluorescent detection of γ-H2AX foci: Abl pre-B cells were G1-arrested with imatinib for two days and then treated with 10 μg/mL bleocin (EMD Millipore, #203408) for two hours or 2 μg/mL etoposide (Sigma, #E1383) for one hour, after which they were washed with phosphate-buffered saline (PBS) and allowed to recover in fresh imatinib media for 24 hours. For γ-H2AX immunostaining, the cells were plated onto coverslips coated with Cell-Tak (Corning, #354240), fixed in 4% paraformaldehyde for 10 minutes, permeabilized with 0.1% Triton X-100 in PBS for five minutes, blocked with 3% bovine serum albumin (BSA) in PBS (w/v) at room temperature for one hour, incubated with mouse anti-γ-H2AX (EMD Millipore, #05–636) at 1:1,000 dilution in 4℃ overnight, washed with PBS, and incubated with Alexa Fluor 594 donkey anti-mouse IgG (Thermo Fisher, #A-21203) at room temperature for one hour. After washing the cells again with

PBS, the coverslips were mounted onto microscope slides in ProLong Gold Anti-Fade Mountant with DAPI (Thermo Fisher, #P36931). Images were acquired on an Olympus BX53 fluorescence microscope at 60X magnification.

Laser micro-irradiation and imaging: *MRI*$^{-/-}$ MEFs were stably transduced with a lentiviral vector pLV (Addgene, #36083) containing an MRI-GFP fusion protein, transiently transfected with 1.5 µg Ku80-RFP using Lipofectamine 2000 (Thermo Fisher), and imaged after 48 hours. To obtain reliable recruitment of GFP-Ku70 with the 405 nm laser, the transfected cells were sensitized with 10 µM BrdU for 24 hours. To arrest cells in G1, *MRI*$^{-/-}$ MEFs stably expressing MRI-GFP were serum-starved in DMEM (Gibco) supplemented with 0.5% FBS (Hyclone) for 72 hours prior to BrdU sensitization and imaging. Live cell imaging was carried out on a Nikon Ti Eclipse inverted microscope equipped with an A1 RMP confocal microscope system and Lu-N3 Laser Units (Nikon, Inc.). Laser micro-irradiation manipulation and time-lapse imaging were performed with the NIS Element High Content Analysis software (Nikon, Inc.) using a 405 nm laser at an energy level adequate for Ku70 accumulation. The relative intensity at laser-damaged sites was calculated as the ratio of the mean intensity at each of the micro-irradiated sites to the corresponding mean intensity of the nucleus as background (considering the entire nucleus). >20 individual cells were analyzed for each data point.

Brain immunohistochemistry: Embryonic day 14.5 and 16.5 mouse embryos were dissected in ice-cold PBS and fixed in 4% paraformaldehyde at 4℃ overnight. Tissues were rinsed with PBS, cryoprotected in 30% sucrose in PBS (w/v) at 4℃ overnight, embedded in Tissue-Tek (Sakura Finetek), frozen on dry ice, and stored at -80℃ before sectioning. Brains were cryosectioned at

18 μm and processed using PBS containing 1.5% donkey serum and 0.35% Triton X-100 for all subsequent steps, except for the washing steps where only PBS was used. Sections were blocked for 30 minutes and incubated with 1:200 dilution of rabbit anti-cleaved caspase 3 (Cell Signaling Technology, #9661) at 4°C overnight. After washing with PBS, 1:1,000 dilution of Cy3 donkey anti-rabbit IgG (Jackson ImmunoResearch, #711-165-152) was applied at room temperature for one hour. Nuclear counterstaining was performed with 100 ng/mL DAPI solution. An additional three washes were performed with PBS, and the slides were then coverslipped using VectaShield mounting medium (Vector Laboratories). Fluorescent images were taken on a Fluoview FV3000 confocal laser scanning microscope (Olympus, Inc.). The following mice were analyzed: $MRI^{-/-}$:$XLF^{+/-}$ (n = 2) and $MRI^{-/-}$:$XLF^{-/-}$ (n = 2) littermates at embryonic day 14.5, and $MRI^{-/-}$:$XLF^{+/-}$ (n = 1) and $MRI^{-/-}$:$XLF^{-/-}$ (n = 2) littermates at embryonic day 16.5. Five coronal sections per animal were observed for a total of 35 sections.

Flow cytometric analyses: Antibodies used (all at 1:500) for lymphocyte staining were: Pacific Blue anti-B220 (BioLegend, #103227), APC anti-CD43 (BioLegend, #143208), PE/Cy7 anti-IgM (BioLegend, #406514), Pacific Blue anti-CD4 (BioLegend, #100531), PE/Cy7 anti-CD8 (BioLegend, #100722), FITC anti-CD3ε (BioLegend, #100306), APC anti-TCRβ (eBioscience, # 17-5961-82), PE anti-IgG2b (BioLegend, #406707), and APC anti-IgG1 (BioLegend, #406609). Single-cell suspensions from bone marrow, thymus, and spleen were incubated with Fc block (BD Pharmingen, # 553141) at a density of 10^6 cells/mL on ice for 15 minutes prior to staining. Analyses of the G2/M checkpoint using DNA content (7-AAD, BD Biosciences, #559925) and anti-phospho-histone H3 serine 10 (EMD Millipore, #06-570) were performed as previously described (Xu B et al. 2011). Data were acquired on a LSR II flow cytometer (BD Biosciences)

and analyzed using FlowJo (FlowJo, LLC).

Southern blot analyses: Genomic DNA from cells containing MGINV were digested with *NheI* or *XbaI* and hybridized to a ^{32}P-labeled Thy1 or GFP probe as previously described (Bredemeyer AL et al. 2006, Hung PJ et al. 2017). The Thy1 probe is a ~800-base pair Thy1.1 cDNA (which differs from Thy1.2 by only a single aa residue) fragment, and the GFP probe is a ~700-base pair GFP cDNA fragment.

Nuclear extraction and immunoprecipitation (IP): Cells were lysed in cytoplasmic extraction (CE) buffer (10 mM Tris-HCl pH 7.4, 10 mM KCl, 1.5 mM $MgCl_2$, 1 mM EDTA, 0.05% Triton X-100) supplemented with a protease inhibitor cocktail (Sigma) on ice for 15-20 minutes. After centrifugation (3,000 rpm, five minutes), the nuclear pellet was washed with CE buffer (without Triton X-100) and incubated in 0.5X pellet volume of nuclease buffer (20 mM Tris-HCl pH 7.4, 1.5 mM $MgCl_2$, 25% v/v glycerol) with 5 U/μL benzonase (Sigma) on ice for one hour to digest genomic DNA. 1X pellet volume of nuclear extraction (NE) buffer (20 mM Tris-HCl pH 7.4, 500 mM KCl, 1.5 mM $MgCl_2$, 0.2 mM EDTA, 25% v/v glycerol) was then added, and the pellet was ground using a dounce homogenizer (Sigma) before incubation with gentle rotation at 4℃ for one hour. The homogenate was clarified by centrifugation (14,800 rpm, 30 minutes), and the supernatant was dialyzed in excess BC100 buffer (20 mM Tris-HCl pH7.4, 100 mM KCl, 0.2 mM EDTA, 20% v/v glycerol) at 4℃ overnight using the Pur-A-Lyzer Maxi 6000 Kit (Sigma). The dialyzed supernatant was clarified by centrifugation (14,800 rpm, 30 minutes) and incubated with 30 μL bed volume of EZView Red HA (Sigma, #E6779) or FLAG (Sigma, #F2426) affinity gel on a rotator at 4℃ for four hours. The beads were washed four times with TAP buffer (50

mM Tris-HCl pH 7.4, 100 mM KCl, 5 mM $MgCl_2$, 0.2 mM EDTA, 10% v/v glycerol, 0.1% v/v Triton X-100) and eluted by boiling in LDS sample buffer (Thermo Fisher) for SDS-PAGE and western blot analysis. For IP of endogenous MRI, nuclear extract was first incubated with ~5 µg nonspecific Armenian hamster IgG (BioLegend, #400940) or anti-mouse MRI (13E10.E12.C10) at 4℃ overnight and then with Pierce Protein L magnetic beads (Thermo Fisher, # 88849) at 4℃ for two hours.

For proteomic analysis, the anti-FLAG beads were eluted with 0.4 mg/mL FLAG peptide (Sigma, #F3290) in TAP buffer on a rotator at 4℃ for one hour. The MRI-containing complexes were visualized by SDS-PAGE and silver staining before being precipitated by TCA. Associated proteins were then identified by LC-MS/MS at the Taplin Mass Spectrometry Facility (Harvard Medical School) using an LTQ Orbitrap Velos Pro ion-trap mass spectrometer (Thermo Fisher) and SEQUEST software (Eng JK et al. 1994).

For sequential IP, nuclear extract from WT Abl pre-B cells expressing HA-tagged MRI and FLAG-tagged Ku80 was incubated with EZView Red HA affinity gel beads at 4℃ for four hours, after which the beads were washed four times with TAP buffer and eluted with 0.5 mg/mL HA peptide (Sigma, #I2149) in TAP buffer at 4℃ for one hour. The eluate was incubated with 4 µg mouse IgG1 (Santa Cruz, #sc-3877) or mouse anti-FLAG (Sigma, #F1804) at 4℃ overnight and then with 30 µL bed volume of Dynabeads Protein G (Thermo Fisher, #10003D) at 4℃ for two hours. The beads were washed four times with TAP buffer and boiled in LDS sample buffer for SDS-PAGE and western blot analysis.

Size-exclusion chromatography (SEC) was performed using an AKTA Pure FPLC on a Superose 6 Increase 10/300 GL column (GE Healthcare, #29-0915-96). Anti-FLAG-precipitated MRI complexes (500 µL) were loaded onto the pre-equilibrated column and eluted with TAP

buffer at a flow rate of 0.5 mL/minute. 0.5 mL fractions were collected and concentrated using StrataClean resin (Agilent) before SDS-PAGE and western blot analysis.

Chromatin fractionation: Cells were first pre-extracted in CSK buffer (100 mM NaCl, 10 mM PIPES pH 6.8, 3 mM $MgCl_2$, 300 mM sucrose) with 0.05% Triton X-100 on ice for 15 minutes. After centrifugation (1,500 x g, five minutes), the chromatin pellet was washed with PBS and incubated in CSK buffer with 0.5% Triton X-100 and 0.1 µg/mL RNase A (Sigma, #R4875) at room temperature for 10 minutes and on ice for 20 minutes. After centrifugation (1,500 x g, five minutes), the pellet was washed with PBS and incubated in CSK buffer with 5 U/µL benzonase on ice for one hour. The chromatin fraction was boiled in LDS sample buffer and then analyzed by SDS-PAGE and western blotting.

Western blot analyses: The primary antibodies and dilutions used for western blotting were: anti-cytoskeletal actin (1:10,000, Bethyl Laboratories, #A300-485A), anti-FLAG (1:5,000, Sigma, #F7425), anti-HA (1:5,000, Santa Cruz, #sc-805), anti-DNA-PKcs (1:2,000, Thermo Fisher, # MS-423-P), anti-Ku80 (1:2,000, Cell Signaling Technology, #2753S), anti-Ku70 (1:2,000, Cell Signaling Technology, #4588S), anti-XLF (1:2,000, Bethyl Laboratories, #A300-730A), anti-C9orf142 (PAXX) (1:1,000, Abcam, #ab126353), anti-XRCC4 (1:1,000, Santa Cruz, #sc-8285), anti-ATM (1:2,000, Sigma, #A1106), anti-RAD50 (1:1,000, Abcam, #ab89), anti-Mre11 (1:5,000, Novus Biologicals, #NB100-142), anti-Nbs1 (1:5,000, Abcam, #ab23996), anti-KAP-1 (1:5,000, GeneTex, #GTX102226), anti-ATR (1:1,000, Novus Biologicals, #NB100-323), anti-ATRIP (1:1,000, Sigma, #SAB4503325), anti-tubulin (1:10,000, Sigma, #T5168), anti-H2AX (1:5,000, EMD Millipore, #07-627), anti-γH2AX (1:10,000, EMD Millipore, #05-

636), anti-AID (1:1,000, generated by Chaudhuri lab), and anti-MRI (supernatant from clonal hybridoma line 13E10.E12.C10, generated in-house).

MRI protein expression and purification: The coding regions of the mouse *MRI* and human *MRI* genes were codon-optimized for expression in *E. coli* (Genscript) and used as templates to sub-clone the coding regions into a modified pET15b vector (Novagen). Peptide truncations were generated by overlapping PCR and validated by sequencing. Mouse MRI and human MRI proteins were expressed in BL21(DE3) *E. coli* cells (Novagen), cultured in Luria Broth media at 37℃, induced at an OD600 (optical density at 600 nm) of 0.6 with 0.5 mM IPTG, and grown for 12-15 hours at 18℃. Cells were harvested, resuspended in lysis buffer (20 mM Tris-HCl pH 7.5, 250 mM NaCl, 5 mM 2-mercaptoethanol), and lysed using an EmulsiFlex-C5 homogenizer (Avestin), after which the resulting lysate was clarified by centrifugation (47,000 x g at 4℃, 40 minutes). Proteins were purified using a series of affinity and ion-exchange chromatographic columns (GE Healthcare). Following TEV protease digestion to separate the maltose-binding protein (MBP) fusion, the resulting sample was purified further by sequential ion-exchange and SEC. Protein purity was assessed by Coomassie staining of SDS-PAGE and mass spectrometry.

Hydrogen deuterium exchange mass spectrometry (HDX-MS): MRI samples were buffer-exchanged with PBS pH 7.4. Deuterium labeling was initiated by diluting samples (50 μM, 2 μL) 10-fold with either D_2O buffer or H_2O buffer for measuring no-deuterium control samples. At eight different time intervals (10, 30, 60, 120, 360, 900, 3600, and 14400 seconds), the labeling reaction was quenched by rapidly adjusting the pH to 2.5 with 30 μL of quench buffer (3 M urea, 0.6% trifluoroacetic acid, H_2O) at 4℃. The protein mixture was then immediately injected into a

custom-built HDX device and passed through a column containing immobilized pepsin (2 mm × 20 mm) at a flow rate of 100 μL/minute in 0.1% formic acid, and the resulting peptic peptides were captured on a ZORBAX Eclipse XDB C8 column (2.1 mm × 15 mm, Agilent) for desalting (three minutes). The C8 column was then switched in-line with a Hypersil Gold C18 column (2.1 mm × 50 mm, Thermo Fisher), and a linear gradient (4-40% acetonitrile, 0.1% formic acid, 50 μL/minute flow rate for five minutes) was used to separate the peptides and direct them to a LTQ FT-ICR mass spectrometer (Thermo Fisher) equipped with an electrospray ionization source. Valves, columns, and tubing for protein digestion and peptide separation were submerged in an ice-water bath to minimize back-exchange.

The resulting data were processed and peptides identified by exact mass analysis and LC-MS/MS using Mascot (Matrix Science). The raw HDX spectra and peptide sets were submitted to HDX Workbench for calculation and data visualization in a fully automated fashion (Pascal BD et al. 2012). Peptides for each run were assessed based on their relative representation and statistical validation; only the top six peptides from each MS scan were used in the final analysis. Deuterium uptake at each time point was calculated by subtracting the centroid of the isotopic distribution of the undeuterated peptide from that of the deuterated peptide. Relative deuterium uptake was plotted versus labeling time to afford kinetic curves.

Circular Dichroism (CD): CD wavelength scans were taken using a Chirascan CD spectrometer (Applied Photophysics). The changes in molar ellipticity of 10 μM MRI protein samples were monitored at 4°C. All samples were prepared in 25 mM Na_3PO_4 pH 7, 150 mM NaCl, and 5 mM 2-mercaptoethanol buffer containing 0-50% 2,2,2-trifluorethanol (TFE). All experiments were performed in triplicate.

Multi-angle light scattering-size exclusion chromatography (MALS-SEC): Standard MALS experiments were carried out on a Superdex 200 10/300 GL column (GE Healthcare) connected in-line to a Dawn Heleos II MALS detector (Wyatt Technologies). 100 µL samples (2 mg/mL) were injected at a flow rate of 0.3 mL/minute into a column equilibrated in 10 mM HEPES pH 7.5, 150 mM NaCl, and 2 mM *tris*(2-carboxyethyl)phosphine (TCEP) buffer. Molecular weights and standard deviations were determined using Astra software package version 6.1 (Wyatt Technologies). All experiments were performed at room temperature and in triplicate.

MRI-ATM co-IP: 40 nM purified recombinant biotin-FLAG-ATM was incubated with MBP-tagged human MRI, $MRI^{\Delta N}$, or $MRI^{\Delta C}$ (50, 100, or 200 nM) and 100 ng bovine serum albumin (BSA, New England Biolabs) in A buffer (25 mM Tris-HCl pH 8.0, 100 mM NaCl, 10% v/v glycerol) at room temperature for 15 minutes with a final volume of 30 µL. 2 µL of Dynabeads M-280 Streptavidin (Life Technologies) were pre-washed with 1 mg/mL BSA and 1% CHAPS (Sigma). The samples were then added to the bead mixture with 0.1% CHAPS in A buffer and incubated on ice for 15 minutes. After three washes with 2 µg/mL BSA in A buffer with 0.1% CHAPS, proteins bound to the beads were resolved by SDS-PAGE using NuPAGE 4-12% Bis-Tris (Thermo Fisher), followed by western blotting with primary anti-ATM antibody (Santa Cruz, #sc-135663) or anti-MBP antibody (GeneTex, #GTX50060) and secondary anti-mouse IgG antibody (Thermo Fisher, #A32730) or anti-rabbit IgG antibody (Thermo Fisher, #A21076).

Hybridoma generation: Armenian hamsters (Cytogen Research and Development, Cambridge, MA) were immunized s.c. with 50 µg each of four KLH-conjugated peptides (GenScript), listed

below, emulsified in Freund's adjuvant (CFA then IFA at two-week intervals), followed by one injection of peptides with Alhydrogel (InvivoGen) (Sheehan K et al. 1989). The sequences of the four KLH-conjugated peptides were: GAP-122 (LKSKTKTRVLPSWMTAPVDERKVC), GAP-123 (KQTAAWAQRVGAATRAPATEC), GAP-124 (GRKQEKPWEQRSLEATDKLQC), and GAP-125 (EEKEEEDALKYVREIFFS) – which encompass the entire length of the mouse MRI protein. Immune serum showed positive titers by ELISA using peptide-coated plates and also by western blot analysis of recombinant protein. Three days prior to fusion, animals were boosted i.v. with 25 µg each of the KLH-conjugated peptides solubilized in endotoxin-free PBS. Immune splenocytes were fused to the P3X63Ag8.653 murine myeloma line using standard procedures. Cultures were screened initially by ELISA using individual peptides and then by western blotting of WT and *MRI*$^{-/-}$ Abl pre-B cell lysates. Antigen-reactive wells were sub-cloned via two rounds of limiting dilution to ensure clonal populations. Isotype analysis were performed using cassettes provided by Antagen Pharmaceuticals. Monoclonal antibodies were purified and concentrated by Protein A affinity chromatography using standard methods (Sheehan K et al. 1989).

13E10.E12.C10 is an IgG3-type antibody that recognizes the GAP-124 antigen.

Chapter 3: A Genetic Screen for Novel NHEJ Factors

3.1 Background

Although XLF has long been implicated as a major NHEJ factor, presumably involved in the alignment of broken DNA ends, its requirement for DSB repair in vivo appears to be variable depending on cell type. In particular, XLF-deficient lymphocytes can undergo V(D)J end joining without any detectable loss of efficiency, and correspondingly, XLF-deficient mice show normal lymphocyte maturation (Li G et al. 2008). Conversely, XLF-deficient MEFs and ES cells display an impaired ability to rearrange episomal V(D)J recombination substrates when expressing RAG ectopically and are highly sensitive to IR (Zha S et al. 2007, Li G et al. 2008). These paradoxical observations can be explained by the possibility that a lymphocyte-specific mechanism somehow can compensate for XLF function. Indeed, in XLF-deficient lymphocytes, the DDR kinase ATM and its downstream targets H2AX and 53BP1 become absolutely essential for V(D)J end joining, even though, like XLF, these factors are otherwise dispensable for the repair of RAG DSBs (Zha S et al. 2011). In fact, the specific roles of these proteins are accentuated by the absence of XLF: notably, *XLF*$^{-/-}$:*H2AX*$^{-/-}$ and *XLF*$^{-/-}$:*53BP1*$^{-/-}$ pre-B cells exhibit excessive resection of DNA ends, suggesting that H2AX and 53BP1 operate in part to preserve junctional integrity at DSBs (Zha S et al. 2011, Liu X et al. 2012, Oksenych V et al. 2012). Moreover, while DNA-PKcs has mainly been implicated in CE joining due to its necessity for stimulating Artemis, *XLF*$^{-/-}$:*53BP1*$^{-/-}$ pre-B cells demonstrate a block in both SJ and CJ formation, suggesting that DNA-PKcs also functions to promote general DSB repair in a manner independent of Artemis activation (Oksenych V et al. 2013). We speculated that XLF deficiency creates a setting in which NHEJ is compromised such that it must increasingly rely on other compensatory factors, such as ATM and DNA-PKcs; thus,

it is plausible that new components of the NHEJ pathway could be uncovered in a XLF-deficient background. To this end, we developed a CRISPR/Cas9-based genetic screen to look for hits that would prevent V(D)J end joining in XLF-deficient lymphocytes.

3.2 Set-up of the Screen

3.2.1 Establishment of a Reporter Cell-line System

To create a cellular system by which we could assay for V(D)J end joining, we generated Abelson murine leukemia virus-transformed (Abl) pre-B cell-lines from the bone marrows of 3-5 week-old WT and *XLF*$^{-/-}$ mice that carried an Eμ-Bcl2 transgene (which inhibits apoptotic signals triggered by DSBs). Upon treatment with the Abl kinase inhibitor imatinib, Abl pre-B cells arrest in G1, express RAG, and undergo recombination at their immunoglobulin kappa light chain (Igκ) loci (Muljo SA and Schlissel MS 2003, Bredemeyer AL et al. 2006). We transduced these cells with a retroviral V(D)J recombination substrate MGINV, which contains a pair of RSSs flanking an anti-sense GFP cDNA; rearrangement is mediated by inversion and places the GFP cDNA in the sense direction, enabling its expression (Figure 1A). An added advantage of this approach is that it allows us to track the repair of RAG DSBs over time by Southern blot, using probes which hybridize with the GFP and Thy1.2 cDNAs in the substrate (Figure 1A). As expected, in WT Abl pre-B cells, RAG DSBs were efficiently ligated to produce SJs and CJs, leading to robust GFP expression, whereas in *Lig4*$^{-/-}$ Abl pre-B cells, they accumulated as free SEs and CEs, precluding the formation of intact GFP sequences (Figure 1B-D). Finally, we introduced into WT and *XLF*$^{-/-}$ Abl pre-B cells a lentiviral vector with a Cas9 gene under the control of a tetracycline-responsive promoter and selected for clones in which we could reliably induce Cas9 expression (Figure 1E).

3.2.2 Implementation of the Screen

We infected WT and *XLF*$^{-/-}$ Abl pre-B cells harboring a single integrant copy of MGINV and the inducible Cas9 cassette with the Yusa lentiviral library of 87,897 guide RNAs (gRNAs) targeting 19,150 mouse protein-coding genes to achieve >1,000X coverage (Koike-Yusa H et al. 2014). The cells were cultured with doxycycline for one week (ensuring sufficient time to knock out both alleles of a gene) before being treated with imatinib to stimulate V(D)J recombination. After four days, we sorted the cells into GFP+ and GFP- populations, representing cells that had successfully and unsuccessfully rearranged the MGINV substrate, respectively, and performed deep sequencing of the bar-coded gRNAs (using Illumina HiSeq) to obtain a read count for each gRNA in the two populations (Figure 2A). We then searched for genes with at least two gRNAs that were enriched by ≥1.8-fold in the GFP- population as compared to the GFP+ population and ranked them according to their mean fold-enrichment. Encouragingly, the top scoring hits in both WT and *XLF*$^{-/-}$ Abl pre-B cells included many positive control genes, such as *Rag1*, *Rag2*, *Xrcc4*, *Lig4*, *Dclre1c* (Artemis), and *Prkdc* (DNA-PKcs), conferring us with a high degree of confidence in the sensitivity of our assay (Figure 2B). On the other hand, a large fraction of our common hits also turned out to be genes involved in cell cycle regulation (e.g. *Pten*), but this is not unexpected since disrupting genes that prevent G1 entry or arrest would likely obstruct V(D)J recombination without necessarily affecting DSB repair by causing RAG destabilization (Li Z et al. 1996, Jiang H et al. 2005). Ultimately, we decided to pursue two unique hits found in *XLF*$^{-/-}$ Abl pre-B cells: **PAXX**, a structural homolog of XRCC4 and XLF, and **MRI**, a poorly characterized peptide with a putative N-terminal Ku-binding motif (KBM) and a C-terminal XLM that is likewise present in XLF and PAXX (Grundy GJ et al. 2016).

3.3 PAXX is Functionally Redundant with XLF

3.3.1 Combined XLF/PAXX Deficiency Inhibits V(D)J End Joining

To validate that PAXX is indeed necessary for the repair of RAG DSBs in XLF-deficient lymphocytes, we generated *PAXX*$^{-/-}$ and *XLF*$^{-/-}$:*PAXX*$^{-/-}$ Abl pre-B cells by using a gRNA to target exon 3 of the murine *PAXX* gene in our WT and *XLF*$^{-/-}$ reporter cell-lines and screened for clones with both alleles of *PAXX* knocked out by western blot and PCR sequencing (Figure 3A and data not shown). After imatinib treatment, *PAXX*$^{-/-}$ Abl pre-B cells were able to rearrange the MGINV substrate as efficiently as WT and *XLF*$^{-/-}$ Abl pre-B cells, as measured by GFP expression; on the other hand, like *Lig4*$^{-/-}$ Abl pre-B cells, *XLF*$^{-/-}$:*PAXX*$^{-/-}$ Abl pre-B cells exhibited a major block in V(D)J recombination, with <5% of cells expressing GFP at four days post-treatment (Figure 3B). Correspondingly, Southern blot analysis revealed that WT, *PAXX*$^{-/-}$, and *XLF*$^{-/-}$ Abl pre-B cells all successfully made SJs and CJs without any observable evidence of unrepaired RAG DSBs, while *XLF*$^{-/-}$:*PAXX*$^{-/-}$ Abl pre-B cells showed undetectable levels of SJ and CJ formation with abundant accumulation of loose SEs and CEs in a manner similar to *Lig4*$^{-/-}$ Abl pre-B cells (Figure 3C-D and 4). This defect could be reversed by the ectopic expression of WT PAXX, but not a PAXX mutant with two substitutions in the C-terminal XLM (valine 199 → alanine, phenylalanine 201 → alanine) that abrogate its interaction with Ku70/80 (Figure 5A-D). These results indicate that PAXX operates redundantly with XLF in V(D)J end joining and that its activity in this context depends on the presence of Ku70/80. PAXX has been demonstrated to promote the association of Ku70/80 and many of its binding partners, including DNA-PKcs and Lig4, with chromatin at DSBs, so it could be that PAXX can carry out a general function to compensate for that of XLF, or that PAXX is responsible for recruiting to DNA another protein which has an overlapping role with XLF (Ochi T et al. 2015).

3.3.2 Combined XLF/PAXX Deficiency Prevents Genotoxic DSB Repair

To assess whether the V(D)J end joining defect in *XLF*$^{-/-}$:*PAXX*$^{-/-}$ Abl pre-B cells reflects a broader NHEJ deficiency, we monitored the repair of genotoxic DSBs, using nuclear γ-H2AX as a surrogate marker for DNA damage, in G1-arrested WT, *PAXX*$^{-/-}$, *XLF*$^{-/-}$, *XLF*$^{-/-}$:*PAXX*$^{-/-}$, and *Lig4*$^{-/-}$ Abl pre-B cells treated with the radiomimetic agent bleocin or the topoisomerase II poison etoposide, both of which generate DSBs through distinct mechanisms. After a 24-hour recovery period, a significant percentage of WT, *PAXX*$^{-/-}$, and *XLF*$^{-/-}$ Abl pre-B cells were able to resolve the genotoxic DSBs, as indicated by decreased γ-H2AX foci counts, whereas *XLF*$^{-/-}$:*PAXX*$^{-/-}$ and *Lig4*$^{-/-}$ Abl pre-B cells displayed little to no decline in γ-H2AX signals, implying that DSB repair is severely compromised, or even abolished, in these cells (Figure 6A-D). Together, our findings show that NHEJ is impaired on a scope beyond V(D)J recombination in the absence of both XLF and PAXX. In agreement, several concurrent studies reported that XLF:PAXX double-deficiency in mice leads to embryonic lethality characterized by extensive neuronal apoptosis – a phenotype that also characteristically manifests in *Lig4*$^{-/-}$ and *XRCC4*$^{-/-}$ mice (Balmus G et al. 2016, Kumar V et al. 2016, Lescale C et al. 2016, Tadi SK et al. 2016, Hung PJ et al. 2017, Liu X et al. 2017, Abramowski V et al. 2018).

Although it might be tempting to speculate that PAXX functions identically to XLF due to their structural homology, there are clear differences in their contributions to NHEJ, as PAXX deficiency often results in less prominent defects: for example, *PAXX*$^{-/-}$ MEFs do not display any overt signs of cytogenetic instability, in contrast to *XLF*$^{-/-}$ MEFs, which occasionally present with chromosomal and chromatid breaks during metaphase, and while *PAXX*$^{-/-}$ B cells undergo CSR at normal frequencies, *XLF*$^{-/-}$ B cells consistently demonstrate a ~50% reduction in CSR efficiency

(Kumar V et al. 2016, Liu X et al. 2017). Furthermore, unlike XLF, PAXX does not appear to be functionally redundant with ATM or DNA-PKcs: *PAXX*$^{-/-}$:*ATM*$^{-/-}$ mice are phenotypically similar to *ATM*$^{-/-}$ mice and do not exhibit SCID, and inhibition of ATM or DNA-PKcs kinase activity in *PAXX*$^{-/-}$ Abl pre-B cells only has a modest effect on V(D)J recombination, suggesting that PAXX possesses a role distinct from that of XLF in NHEJ (Balmus G et al. 2016, Liu X et al. 2017). As PAXX had already been described in detail by other groups, we did not follow up on it; however, the discovery of PAXX in our screen provided a concrete proof-of-concept that we could identify non-core components of the NHEJ pathway in a XLF-deficient setting.

3.4 MRI is Functionally Redundant with XLF

3.4.1 Lymphocyte Development in MRI-deficient Mice

MRI$^{+/-}$ mice harboring a *MRI*$^{-}$ allele in which the entire protein-coding region of the *MRI* gene (encompassing exons 2-4) is replaced by a *LacZ* cassette were derived from cryopreserved sperm supplied by the Knockout Mouse Project (KOMP) Repository and intercrossed to produce *MRI*$^{+/+}$, *MRI*$^{+/-}$, and *MRI*$^{-/-}$ offspring (Figure 7A-B). In collaboration with the Hybridoma Center at Washington University School of Medicine, we raised an Armenian hamster monoclonal IgG3 antibody (13E10.E12.C10) against murine MRI and verified the loss of MRI protein expression in MEFs generated from *MRI*$^{-/-}$ mice by western blot: the antibody recognized a single ~30-kDa band in *MRI*$^{+/+}$, but not *MRI*$^{-/-}$, MEF lysates (Figure 7C). *MRI*$^{-/-}$ mice were born in the predicted Mendelian ratios and displayed no gross physiological or reproductive abnormalities (Figure 7D and data not shown). As compared to their *MRI*$^{+/+}$ littermates, 6 week-old *MRI*$^{-/-}$ mice contained similar distributions and numbers of pro-B (B220^{+}CD43^{+}IgM^{-}), pre-B (B220^{+}CD43^{-}IgM^{-}), naive B (B220^{low}CD43^{-}IgM^{+}), and re-circulating B (B220^{high}CD43^{-}IgM^{+}) cells in their bone marrows

(Figure 7E-F) as well as double-negative T ($CD4^-CD8^-$) and double-positive T ($CD4^+CD8^+$) cells in their thymuses (Figure 7G-H). There were also no significant differences in the frequencies of mature splenic B and T cells between $MRI^{+/+}$ and $MRI^{-/-}$ mice (Figure 7I-J). Thus, akin to $XLF^{-/-}$, $PAXX^{-/-}$, $H2AX^{-/-}$, and $53BP1^{-/-}$ mice, $MRI^{-/-}$ mice demonstrate no apparent defects in lymphocyte development, indicating that the loss of MRI has a negligible impact on V(D)J recombination.

3.4.2 Combined XLF/MRI Deficiency is Embryonically Lethal in Mice

To determine whether XLF/MRI double-deficiency would disrupt V(D)J recombination, we sought to generate $XLF^{-/-}$:$MRI^{-/-}$ mice by intercrossing $XLF^{+/-}$:$MRI^{+/-}$ or $XLF^{+/-}$:$MRI^{-/-}$ breeding pairs. However, we were unable to obtain any viable $XLF^{-/-}$:$MRI^{-/-}$ progeny from these matings in >200 births (Figure 8A-B). Analyses of litters from $XLF^{+/-}$:$MRI^{-/-}$ intercrosses at embryonic days 14.5 and 16.5 revealed the presence of $XLF^{-/-}$:$MRI^{-/-}$ mice at near Mendelian ratios, though these mice were considerably smaller in size than their littermates (Figure 8C-D). Moreover, similar to $Lig4^{-/-}$, $XRCC4^{-/-}$, and $XLF^{-/-}$:$PAXX^{-/-}$ mice, which all succumb in utero after embryonic day 16.5, $XLF^{-/-}$:$MRI^{-/-}$ exhibited widespread apoptosis of post-mitotic neurons in the cortex and ganglionic eminences, as evidenced by cleaved caspase-3 immunostaining, suggesting that the cause of their deaths might be related to a critical deficit in NHEJ (Figure 8E) (Frank KM et al. 1998, Gao Y et al. 1998, Balmus G et al. 2016, Liu X et al. 2017, Abramowski V et al. 2018).

3.4.3 Combined XLF/MRI Deficiency Inhibits V(D)J End Joining

To confirm that the embryonic lethality of $XLF^{-/-}$:$MRI^{-/-}$ mice arose due to a deficiency in NHEJ, we generated $MRI^{-/-}$ Abl pre-B cells from $MRI^{-/-}$ mice and $XLF^{-/-}$:$MRI^{-/-}$ Abl pre-B cells by employing a gRNA to target exon 3 of the *MRI* gene in $XLF^{-/-}$ pre-B cells (Figure 9A). Like WT

and *XLF*$^{-/-}$ Abl pre-B cells, *MRI*$^{-/-}$ Abl pre-B cells showed robust GFP expression and efficient SJ and CJ formation after imatinib treatment, consistent with our previous data that MRI deficiency produces insignificant consequences for V(D)J recombination in mice (Figure 9B-D and 10A-C). Conversely, like *Lig4*$^{-/-}$ Abl pre-B cells, *XLF*$^{-/-}$:*MRI*$^{-/-}$ Abl pre-B cells displayed a severe defect in V(D)J recombination, with only ~5-20% of cells able to express GFP at four days post-treatment (Figure 9B and 10A). As expected, *XLF*$^{-/-}$:*MRI*$^{-/-}$ Abl pre-B cells accumulated unrepaired SEs and CEs, yielding very low levels of SJs and CJs (Figure 9C-D and 10B-C). Thus, *XLF*$^{-/-}$:*MRI*$^{-/-}$ Abl pre-B cells are indeed unable to effectively carry out NHEJ, but interestingly, do not demonstrate a complete block in V(D)J end joining as with *Lig4*$^{-/-}$ Abl pre-B cells, suggesting that the absence of XLF and MRI, rather than abolishing NHEJ, slows the kinetics of DNA end ligation or allows persistent RAG DSBs to be repaired inefficiently through AEJ pathways. To examine the nature of these rare junctions, we performed PCRs covering the SJ sequences in WT, *MRI*$^{-/-}$, *XLF*$^{-/-}$, and *XLF*$^{-/-}$:*MRI*$^{-/-}$ Abl pre-B cells and digested the products with the restriction enzyme *ApaL1*. Intact SJs formed by direct RSS-to-RSS links comprise a palindromic site that is recognized by *ApaL1* (Figure 11A). While most of the 200-base pair SJ products from WT, *MRI*$^{-/-}$, and *XLF*$^{-/-}$ Abl pre-B cells were cleaved by *ApaL1* into 100-base pair fragments, the SJ products from *XLF*$^{-/-}$:*MRI*$^{-/-}$ Abl pre-B cells were largely resistant to *ApaL1* activity, indicating that these SJs are imprecise (Figure 11B). Correspondingly, preliminary analyses of SJ sequences from *XLF*$^{-/-}$:*MRI*$^{-/-}$ Abl pre-B cells revealed deletions of up to ~70 base pairs and the use of 3-4 base pairs of microhomology (Figure 11C). However, as NHEJ and AEJ are both capable of generating DNA joins that fit this description, we cannot definitively rule out the possibility that these aberrant SJs are the outcome of dysregulated NHEJ. A more thorough investigation of MRI function in a true NHEJ-deficient setting will be warranted.

3.5 Conclusion

Based on our hypothesis that XLF deficiency compromises NHEJ to the extent by which novel NHEJ factors can be revealed, we ran an unbiased CRISPR/Cas9-based genetic screen for hits that would significantly impair V(D)J end joining in *XLF*$^{-/-}$, but not necessarily WT, Abl pre-B cells. The principal challenges of studying V(D)J recombination in a population of developing lymphocytes are two-fold. First, RAG DSBs are asynchronously generated and repaired in a pool of dividing lymphoid progenitors at one time, making it difficult to acquire clear "snapshots" of antigen receptor loci rearrangement in chronological progression. Second, RAG DSBs are made randomly (albeit with some preferences) at different combinations of V, D, and J gene segments in individual cells, rendering the analyses of V(D)J recombination by sequence-specific methods, such as PCR and Southern blotting, nigh impossible to interpret. Our Abl pre-B cell-line system allows us not only to derive cells from mice of the desired genotypes, but also to overcome these two obstacles: by treating Abl pre-B cells with imatinib, we are able to uniformly arrest them in G1 and stimulate V(D)J recombination; moreover, by integrating a V(D)J recombination reporter substrate (MGINV) into Abl pre-B cells, we are able to track the efficiency and configurations of RAG-mediated gene rearrangement by flow cytometry and Southern blotting, respectively.

Here, we identified and validated two additional NHEJ factors, PAXX and MRI, in *XLF*$^{-/-}$ Abl pre-B cells. The loss of PAXX or MRI minimally affects V(D)J end joining in WT Abl pre-B cells but strongly inhibits the repair of RAG DSBs in *XLF*$^{-/-}$ Abl pre-B cells. Whereas *PAXX*$^{-/-}$ and *MRI*$^{-/-}$ mice are phenotypically normal, *XLF*$^{-/-}$:*PAXX*$^{-/-}$ and *XLF*$^{-/-}$:*MRI*$^{-/-}$ mice exhibit prenatal lethality in a manner reminiscent of other NHEJ-deficient mice, suggesting that PAXX and MRI operate broadly in NHEJ. Unlike ATM, DNA-PKcs, H2AX, 53BP1, and RAG, PAXX and MRI

share several structural features in common with XLF: PAXX similarly consists of a N-terminal globular head domain, a coiled coil domain, and a disordered C-terminal domain bearing a XLM, while MRI also harbors a XLM at its C-terminus (Grundy GJ et al. 2016). However, PAXX has been demonstrated to stabilize other NHEJ factors on damaged chromatin – a role different from the one proposed for XLF in aligning DNA ends (Ochi T et al. 2015). Furthermore, PAXX is not functionally redundant with ATM, implying that it works by a distinct mechanism (Balmus G et al. 2016, Liu X et al. 2017). We conjectured that MRI, a hitherto uncharacterized small peptide, likewise fulfills a unique activity which helps to enhance the efficiency of NHEJ – a premise that will be explored in the next chapter.

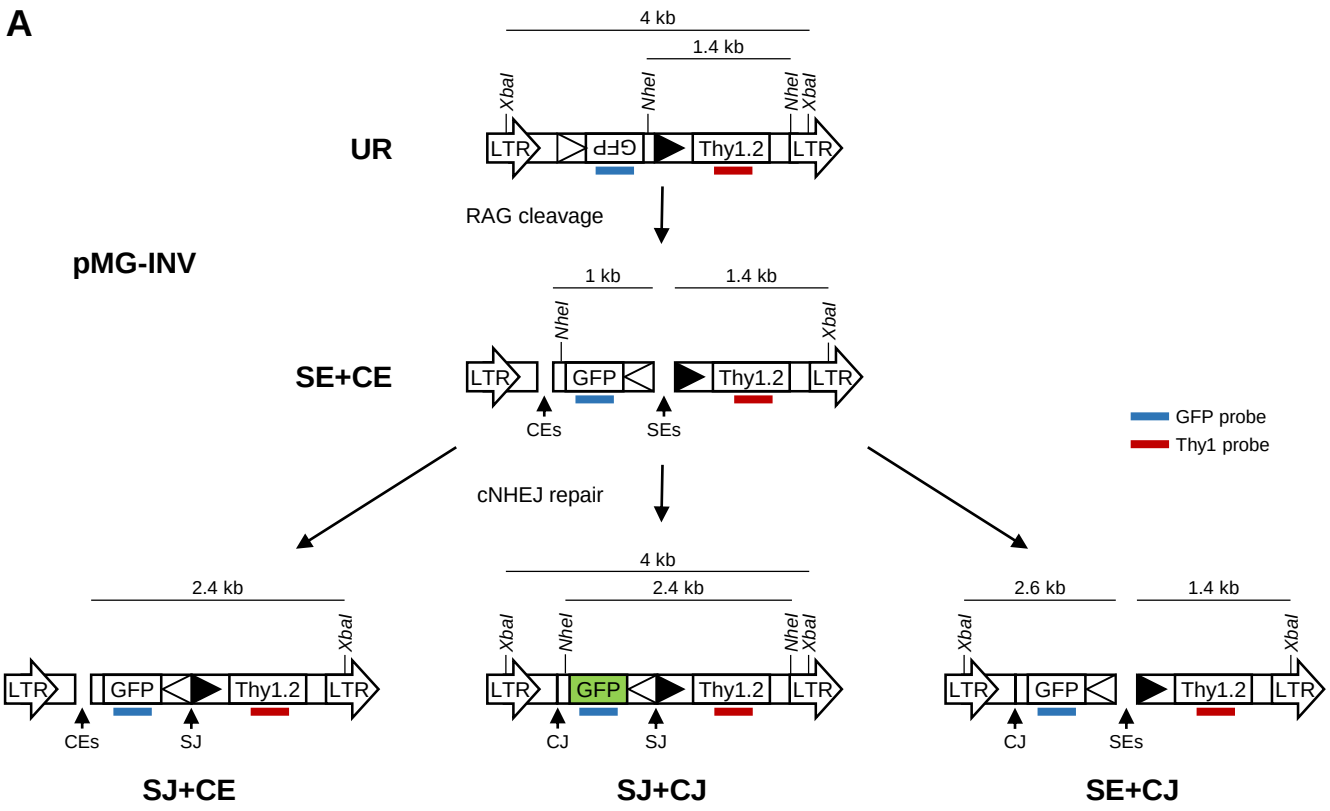
A
4 kb
1.4 kb
XbaI
NheI
NheI
XbaI
UR
LTR
GFP
Thy1.2
LTR
RAG cleavage
pMG-INV
1 kb
1.4 kb
NheI
XbaI
SE+CE
LTR
GFP
Thy1.2
LTR
CEs
SEs
GFP probe
Thy1 probe
cNHEJ repair
4 kb
2.4 kb
2.6 kb
1.4 kb
XbaI
NheI
XbaI
CEs
SJ
CJ
SJ
CJ
SEs
SJ+CE
SJ+CJ
SE+CJ

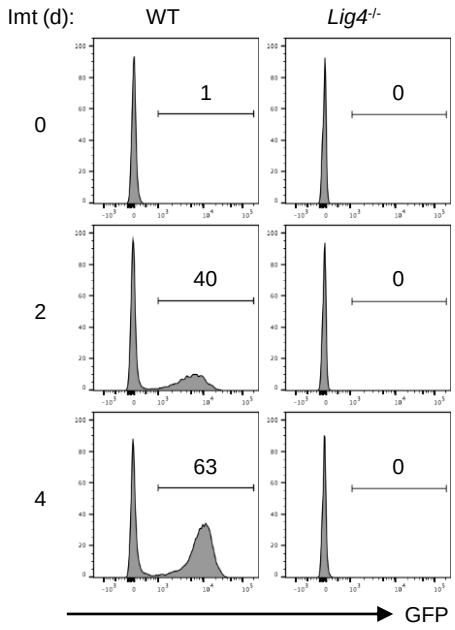
B
Imt (d):
WT
Lig4-/-
0
2
4
1
0
40
0
63
0
GFP

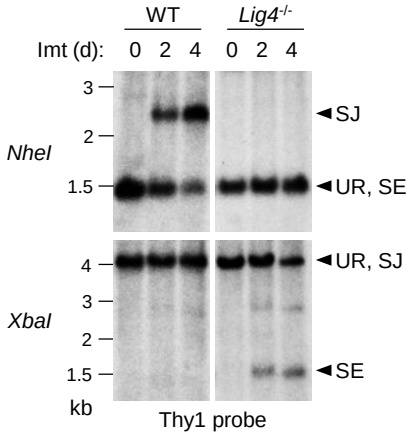
C
WT
Lig4-/-
Imt (d):
0 2 4 0 2 4
NheI
3
2
1.5
SJ
UR, SE
XbaI
4
3
2
1.5
UR, SJ
SE
kb
Thy1 probe

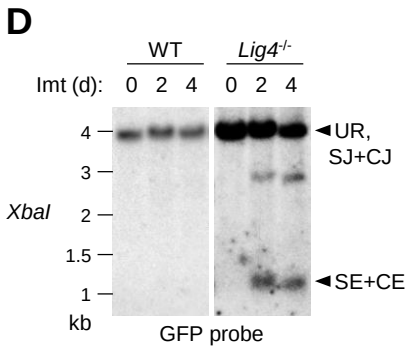
D
WT
Lig4-/-
Imt (d):
0 2 4 0 2 4
XbaI
4
3
2
1.5
1
UR,
SJ+CJ
SE+CE
kb
GFP probe

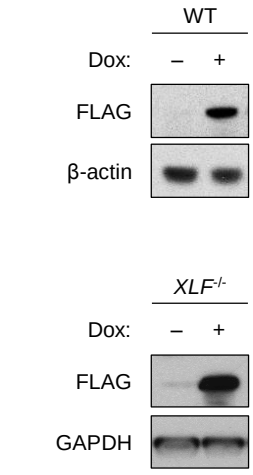
E
WT
Dox:
–
+
FLAG
β-actin
XLF-/-
Dox:
–
+
FLAG
GAPDH

Figure 1

Figure 1: Generation of a V(D)J recombination reporter cell-line system. (A) Schematic of the unrearranged (UR) MGINV V(D)J recombination substrate, its signal end (SE) and coding end (CE) intermediates following RAG cleavage, and the resulting signal join (SJ) and coding join (CJ) products. The long-terminal repeats (LTR), *NheI* and *XbaI* restriction sites, recombination signals (RSs, depicted by open and filled triangles), GFP cDNA, Thy1.2 cDNA, and Thy1 (red) and GFP (blue) probes are shown. The sizes of fragments generated by *NheI* or *XbaI* digests are also indicated. **(B)** Flow cytometric analysis of GFP expression in WT and *Lig4*$^{-/-}$ Abl pre-B cells that were treated with imatinib (Imt) for the indicated lengths of time (days). The percentages of GFP+ cells are specified. **(C)** Southern blot analysis of genomic DNA from cells in (B) that were digested with *NheI* (top) or *XbaI* (bottom) and hybridized to the Thy1 probe. Bands that correspond to UR, SJs, and unrepaired SEs are indicated at the right. **(D)** Southern blot analysis of genomic DNA from cells in (B) that were digested with *XbaI* and hybridized to the GFP probe. Bands that correspond to UR, both SJs and CJs (SJ+CJ), and both SEs and CEs (SE+CE) are indicated at the right. Molecular weights (kilobases) are also shown. **(E)** Western blot analysis of FLAG-tagged Cas9 in untreated and doxycycline (Dox)-treated WT and *XLF*$^{-/-}$ Abl pre-B cells stably transduced with a tetracycline-responsive Cas9 expression cassette. β-actin and GAPDH are shown as protein loading controls.

A

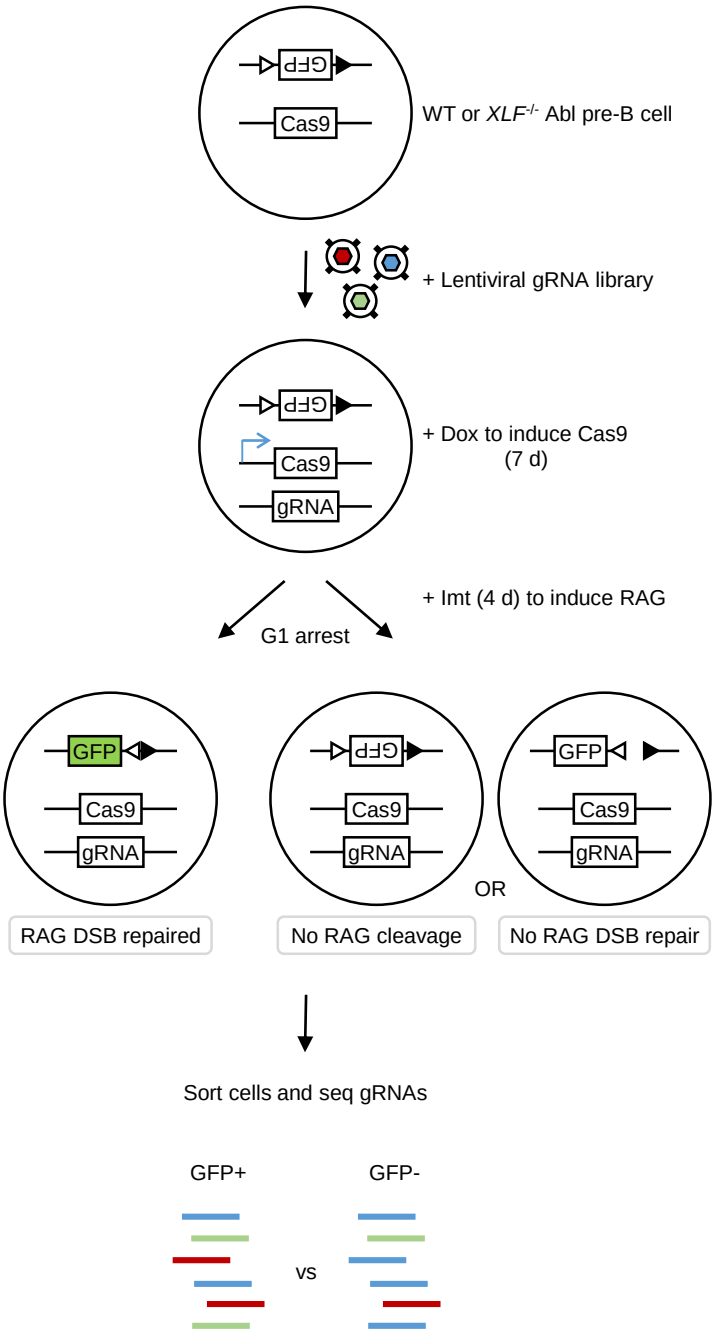

B

WT

Gene	GFP-/GFP+
Rag1	27.77
Rag2	19.93
Xrcc4	9.27
Lig4	8.69
Dclre1c (Artemis)	8.40
Pten	5.93
Mre11a	5.08
Prkdc (DNA-PKcs)	3.91
Nbn (Nbs1)	3.17
Xrcc6 (Ku70)	2.55
Xrcc5 (Ku80)	1.95

XLF$^{-/-}$

Gene	GFP-/GFP+
Rag2	10.88
Rag1	9.02
Xrcc4	7.49
Xrcc6 (Ku70)	5.96
Dclre1c (Artemis)	5.70
Paxx	5.55
Prkdc (DNA-PKcs)	5.54
Lig4	5.30
Nbn (Nbs1)	5.22
Mri	5.10
Mre11a	3.68
Xrcc5 (Ku80)	3.19
Atm	3.10
Trp53bp1 (53BP1)	2.02

Figure 2

Figure 2: A CRISPR/Cas9-based genetic screen for novel NHEJ factors. (A) Flowchart of the procedure: WT and *XLF*$^{-/-}$ Abl pre-B cells were infected with a lentiviral gRNA library, cultured with doxycycline (Dox) for seven days, and treated with imatinib (Imt) for four days to stimulate rearrangement of the MGINV substrate. Cells were then sorted into GFP+ and GFP- populations, and read counts of the gRNAs in each population were obtained by next-generation sequencing. **(B)** List of several top scoring hits from the genetic screen in WT (top) and *XLF*$^{-/-}$ (bottom) Abl pre-B cells. The average enrichment of gRNAs in the GFP- population as compared to the GFP+ population (expressed as a ratio GFP-/GFP+) for gene is indicated.

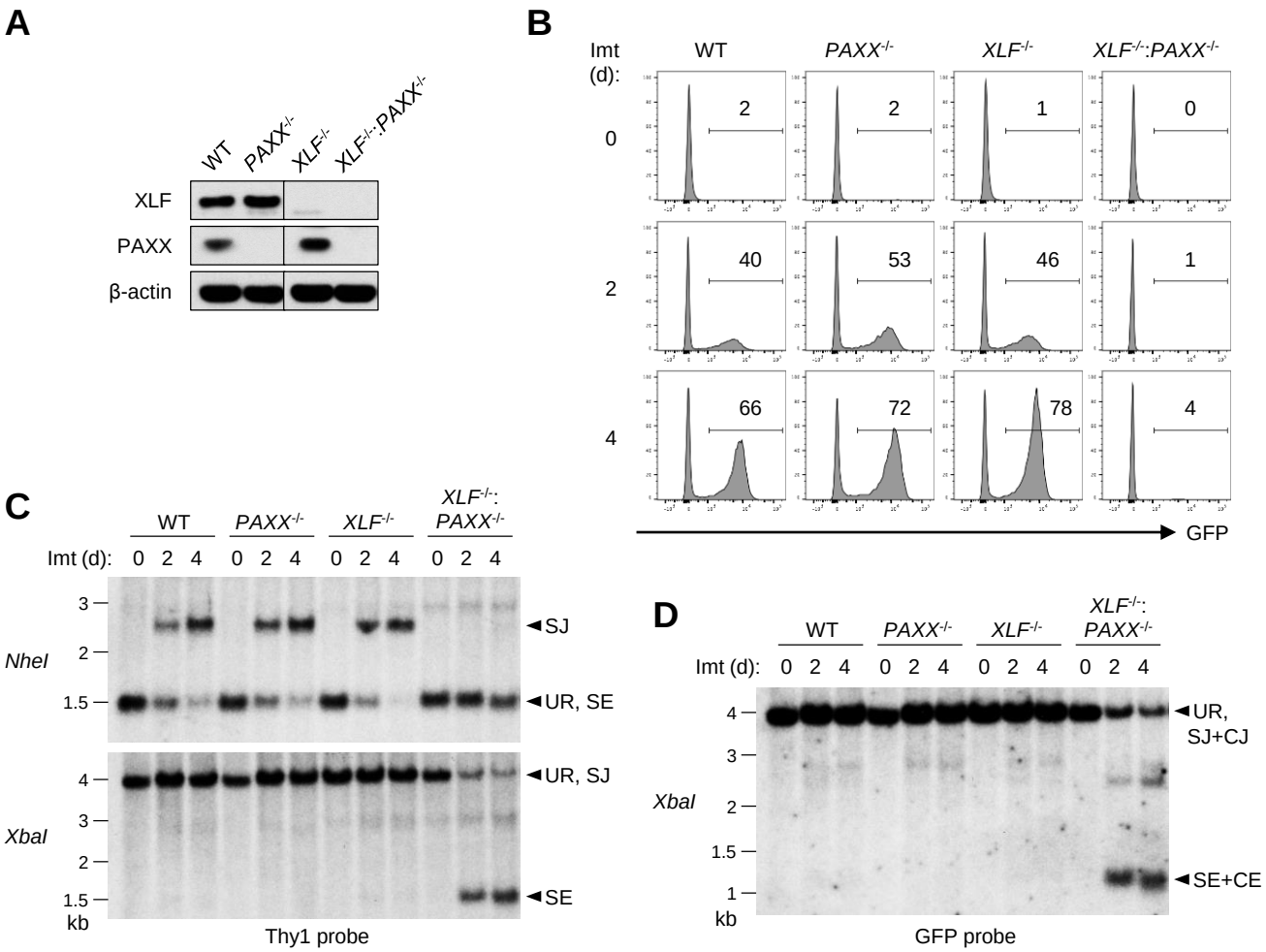
A
WT
PAXX-/-
XLF-/-
XLF-/-:PAXX-/-
XLF
PAXX
β-actin
B
Imt (d):
WT
PAXX-/-
XLF-/-
XLF-/-:PAXX-/-
0
2
4
2
2
1
0
40
53
46
1
66
72
78
4
GFP
C
WT
PAXX-/-
XLF-/-
XLF-/-: PAXX-/-
Imt (d): 0 2 4 0 2 4 0 2 4 0 2 4
NheI
3
2
1.5
SJ
UR, SE
XbaI
4
3
2
1.5
kb
UR, SJ
SE
Thy1 probe
D
WT
PAXX-/-
XLF-/-
XLF-/-: PAXX-/-
Imt (d): 0 2 4 0 2 4 0 2 4 0 2 4
XbaI
4
3
2
1.5
1
kb
UR, SJ+CJ
SE+CE
GFP probe

Figure 3

Figure 3: Combined XLF/PAXX deficiency inhibits V(D)J end joining. (A) Western blot analysis of XLF and PAXX in WT, *PAXX*$^{-/-}$, *XLF*$^{-/-}$, and *XLF*$^{-/-}$:*PAXX*$^{-/-}$Abl pre-B cells. *PAXX*$^{-/-}$ and *XLF*$^{-/-}$:*PAXX*$^{-/-}$ Abl pre-B cells were created from WT and *XLF*$^{-/-}$ Abl pre-B cells, respectively, using CRISPR/Cas9. β-actin is shown as a protein loading control. **(B)** Flow cytometric analysis of GFP expression in WT, *PAXX*$^{-/-}$, *XLF*$^{-/-}$, and *XLF*$^{-/-}$:*PAXX*$^{-/-}$ Abl pre-B cells that were treated with imatinib (Imt) for the indicated lengths of time (days). **(C)** Southern blot analysis of genomic DNA from cells in (B) that were digested with *NheI* (top) or *XbaI* (bottom) and hybridized to the Thy1 probe. **(D)** Southern blot analysis of genomic DNA from cells in (B) that were digested with *XbaI* and hybridized to the GFP probe. Bands corresponding to different MGINV arrangements are indicated at the right as described in Figure 1. Molecular weights (kilobases) are also shown.

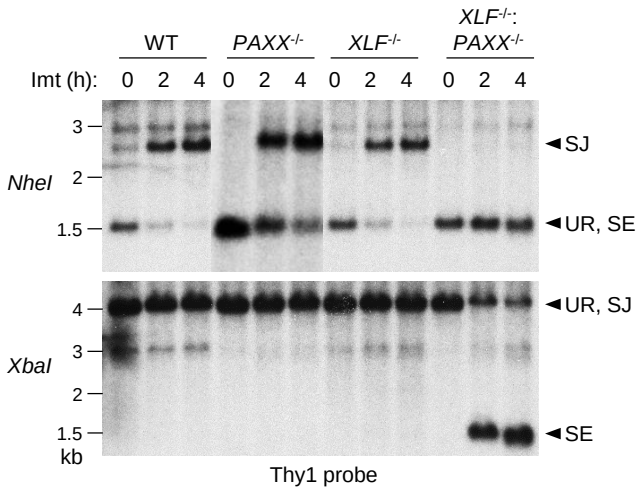
WT
PAXX-/-
XLF-/-
XLF-/-: PAXX-/-
Imt (h): 0 2 4 0 2 4 0 2 4 0 2 4
NheI
3
2
1.5
SJ
UR, SE
XbaI
4
3
2
1.5
kb
UR, SJ
SE
Thy1 probe

Figure 4

Figure 4: Combined XLF/PAXX deficiency inhibits V(D)J end joining (related to Figure 3). Independent clones of WT, *PAXX*$^{-/-}$, *XLF*$^{-/-}$, and *XLF*$^{-/-}$:*PAXX*$^{-/-}$ Abl pre-B cells distinct from those presented in Figure 3 were treated with imatinib (Imt) for the indicated lengths of time (days) and assayed by Southern blotting as described in Figure 1.

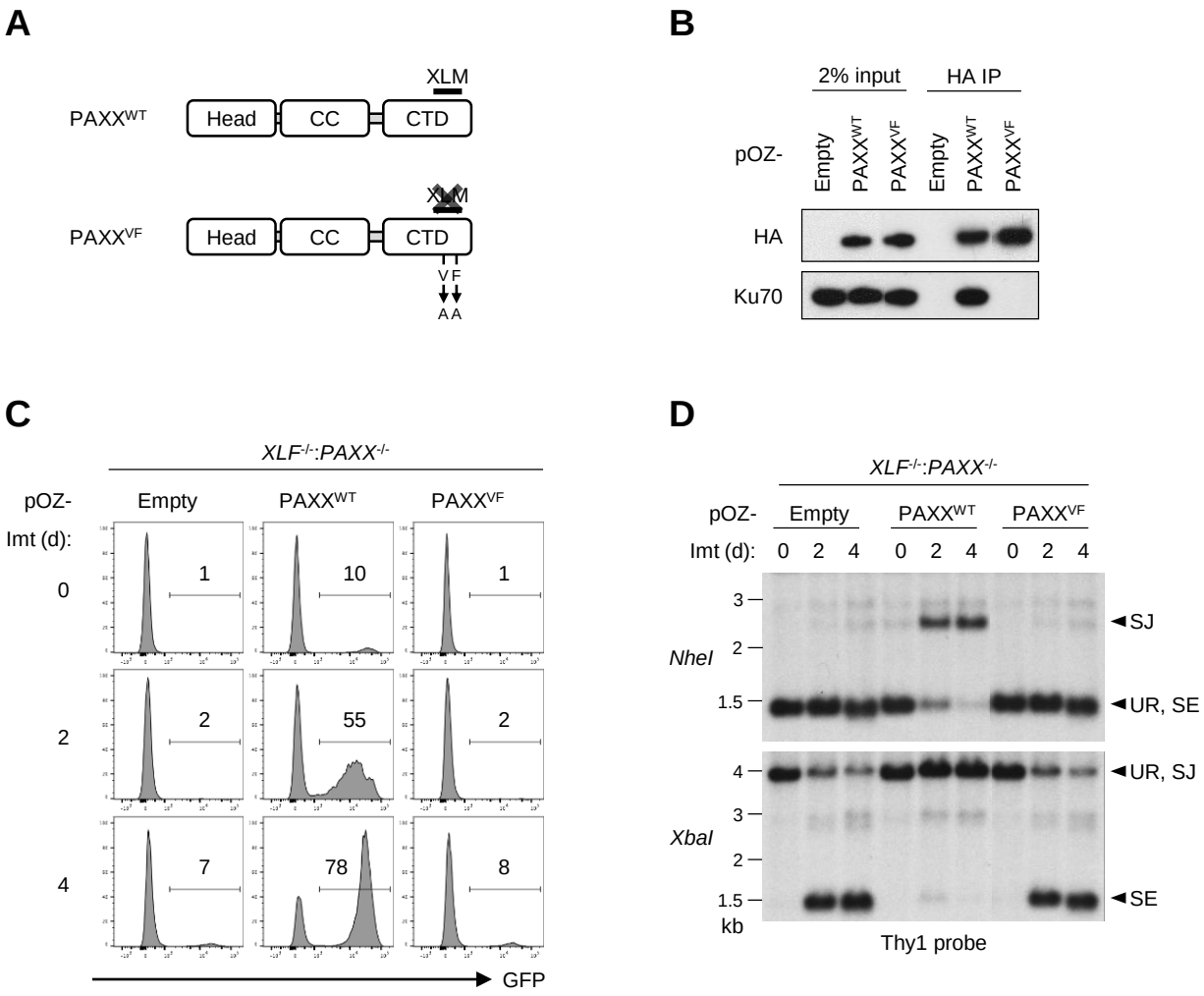
A
XLM
PAXX^WT
Head
CC
CTD
XLM
PAXX^VF
Head
CC
CTD
V F
A A
B
2% input
HA IP
pOZ-
Empty
PAXX^WT
PAXX^VF
Empty
PAXX^WT
PAXX^VF
HA
Ku70
C
XLF-/-:PAXX-/-
pOZ-
Empty
PAXX^WT
PAXX^VF
Imt (d):
0
2
4
1
10
1
2
55
2
7
78
8
GFP
D
XLF-/-:PAXX-/-
pOZ-
Empty
PAXX^WT
PAXX^VF
Imt (d):
0 2 4 0 2 4 0 2 4
NheI
3
2
1.5
SJ
UR, SE
XbaI
4
3
2
1.5
UR, SJ
SE
kb
Thy1 probe

Figure 5

Figure 5: The Ku70/80-binding XLM is essential for PAXX function in XLF-deficient pre-B cells. (A) Schematic of the WT PAXX ($PAXX^{WT}$) and XLM-mutant PAXX ($PAXX^{VF}$) proteins. The three major structural domains of PAXX – the N-terminal globular head domain, the coiled coil domain (CC), and the disordered C-terminal domain (CTD) – and the aa substitutions in the XLM of $PAXX^{VF}$ are shown. **(B)** Western blot analysis of Ku70 association with FLAG-HA-tagged $PAXX^{WT}$ and $PAXX^{VF}$ immunoprecipitated by anti-HA from WT Abl pre-B cell lysates. **(C)** Flow cytometric analysis of GFP expression in $XLF^{-/-}$:$PAXX^{-/-}$ Abl pre-B cells expressing $PAXX^{WT}$ or $PAXX^{VF}$ that were treated with imatinib (Imt) for the indicated lengths of time (days). **(D)** Southern blot analysis of genomic DNA from cells in (C) that were digested with *NheI* (top) or *XbaI* (bottom) and hybridized to the Thy1 probe. Bands corresponding to different MGINV arrangements are indicated at the right as described in Figure 1. Molecular weights (kilobases) are also shown.

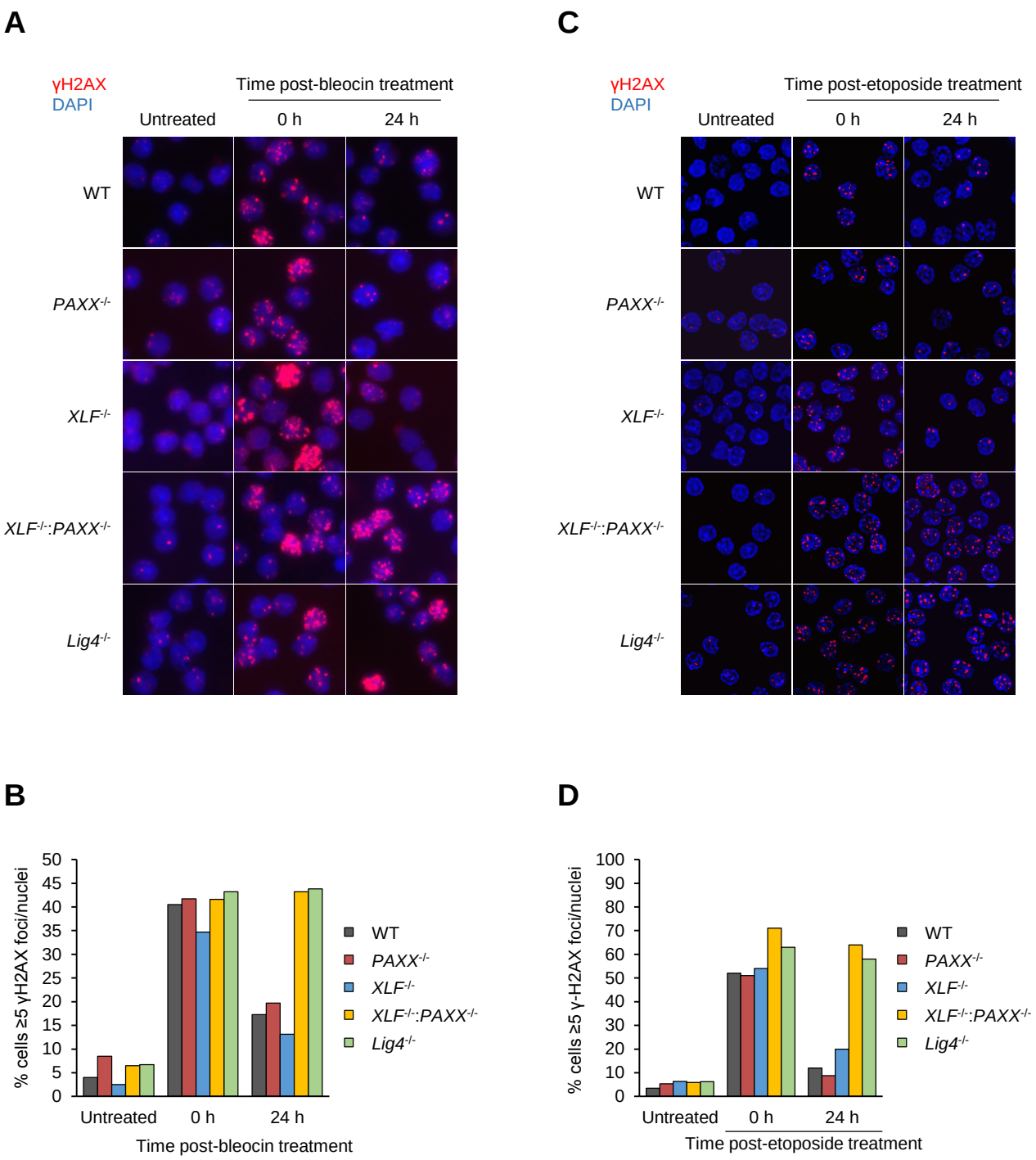
A
γH2AX
DAPI
Time post-bleocin treatment
Untreated
0 h
24 h
WT
PAXX-/-
XLF-/-
XLF-/-:PAXX-/-
Lig4-/-
C
γH2AX
DAPI
Time post-etoposide treatment
Untreated
0 h
24 h
WT
PAXX-/-
XLF-/-
XLF-/-:PAXX-/-
Lig4-/-
B
% cells ≥5 γH2AX foci/nuclei
50
45
40
35
30
25
20
15
10
5
0
Untreated
0 h
24 h
Time post-bleocin treatment
WT
PAXX-/-
XLF-/-
XLF-/-:PAXX-/-
Lig4-/-
D
% cells ≥5 γ-H2AX foci/nuclei
100
90
80
70
60
50
40
30
20
10
0
Untreated
0 h
24 h
Time post-etoposide treatment
WT
PAXX-/-
XLF-/-
XLF-/-:PAXX-/-
Lig4-/-

Figure 6

Figure 6: Combined XLF/PAXX deficiency prevents genotoxic DSB repair in lymphocytes. **(A and C)** Representative micrographs of γ-H2AX foci in G1-phase WT, *PAXX*$^{-/-}$, *XLF*$^{-/-}$, *XLF*$^{-/-}$:*PAXX*$^{-/-}$, and *Lig4*$^{-/-}$ Abl pre-B cells that were untreated or treated with bleocin (A) or etoposide (C) and rested in fresh media for 0 or 24 hours. **(B and D)** Quantification of cells in (A) or (C) with ≥5 γ-H2AX foci per nucleus. At least 100 nuclei were scored for each condition. Data shown is representative of three replicate experiments.

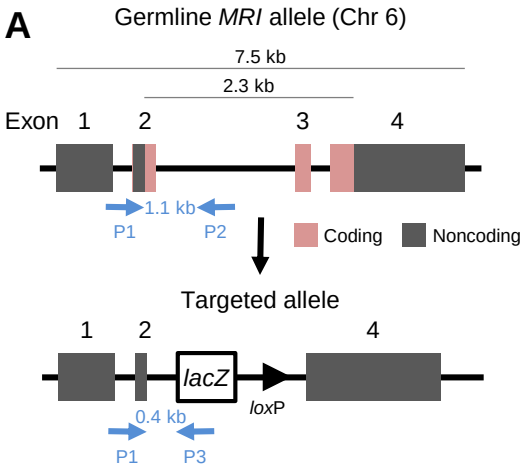

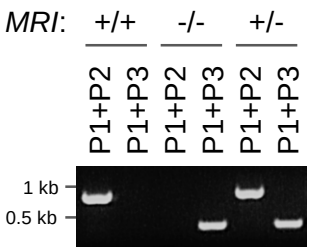

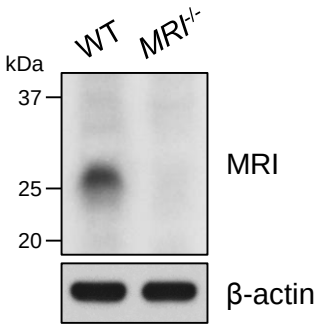

D

MRI	Expected	Actual
+/+	40	41
+/-	80	84
-/-	40	35
Total		**160**

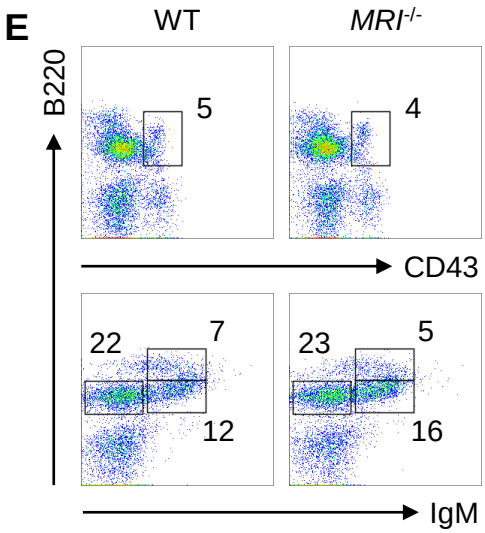

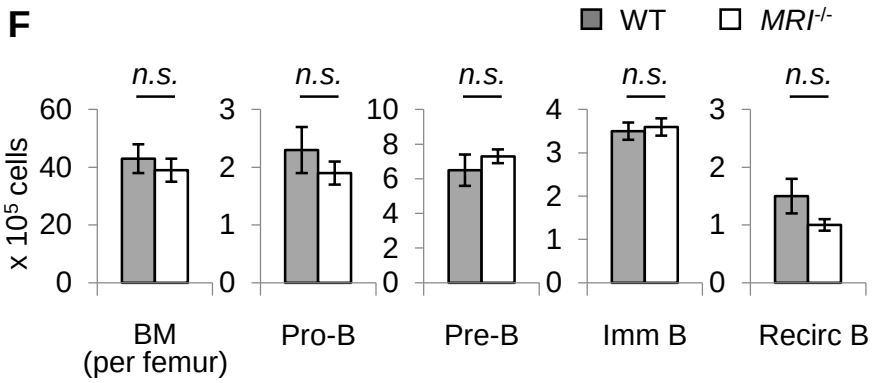

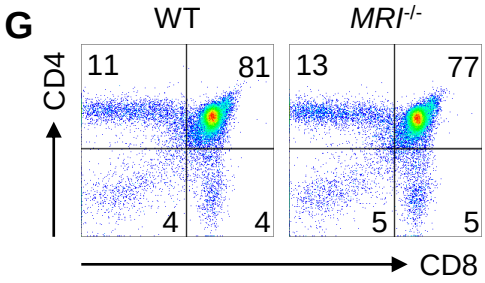

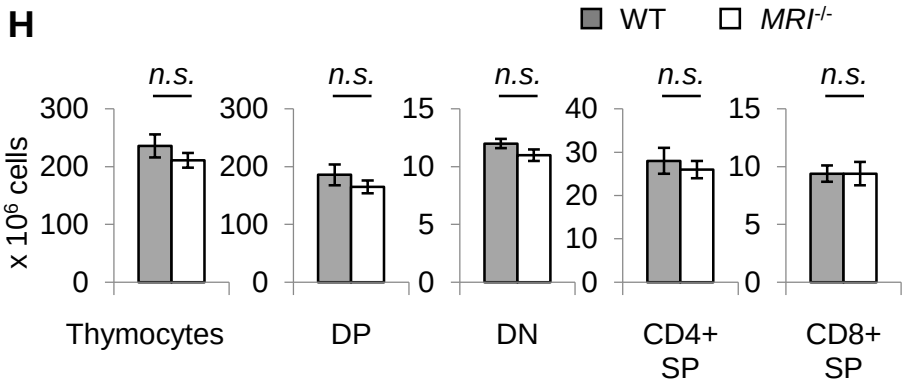

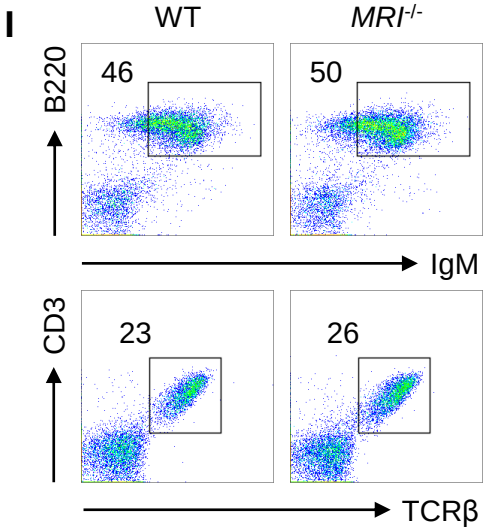

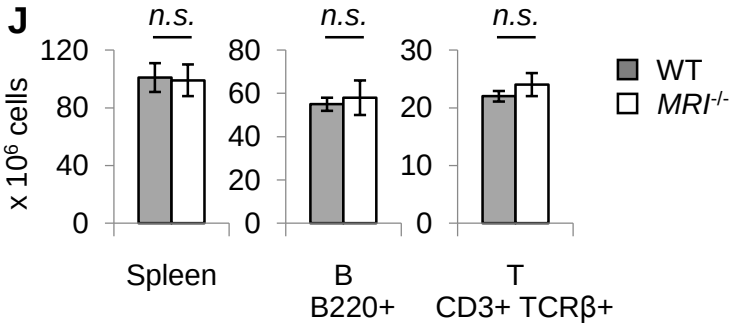

Figure 7

Figure 7: Lymphocyte development in *MRI*$^{-/-}$ mice. (A) Schematic of the mouse *MRI* gene (top) and the targeted allele in which the entire protein-coding region is replaced by a *LacZ* cassette (bottom). Coding and non-coding regions are depicted as pink and gray boxes, respectively. Primers used for genotyping are shown as blue arrows (P1, P2, and P3). **(B)** PCR analysis of genomic DNA from *MRI*$^{+/+}$, *MRI*$^{-/-}$, and *MRI*$^{+/-}$ mice using the indicated primer pairs. **(C)** Western blot analysis of MRI in MEFs derived from WT and *MRI*$^{-/-}$ mice using the 13E10.E12.C10 monoclonal antibody generated against murine MRI. β-actin is shown as a protein loading control. **(D)** Numbers of live births produced from intercrossing *MRI*$^{+/-}$ mice. **(E)** Flow cytometric analysis of pro-B ($B220^{+}CD43^{+}IgM^{-}$), pre-B ($B220^{+}CD43^{-}IgM^{-}$), immature B ($B220^{low}CD43^{-}IgM^{+}$), and re-circulating B ($B220^{high}CD43^{-}IgM^{+}$) cells in the bone marrows (BM) of 6-week old WT and *MRI*$^{-/-}$ littermates. The percentage of cells in each gate is indicated. **(F)** Quantification of total BM, pro-B, pre-B, immature B, and re-circulating B cells per femur. **(G)** Flow cytometric analysis of double-positive (DP, $CD4^{+}CD8^{+}$), double-negative (DN, $CD4^{-}CD8^{-}$), and single-positive (SP, $CD4^{+}CD8^{-}$ or $CD4^{-}CD8^{+}$) thymocytes in 6-week old WT and *MRI*$^{-/-}$ mice. The percentage of cells in each quadrant is indicated. **(H)** Quantification of total, DP, DN, $CD4^{+}$ SP, and $CD8^{+}$ SP thymocytes. **(I)** Flow cytometric analysis of mature B ($B220^{+}IgM^{+}$) and T ($CD3^{+}TCR\beta^{+}$) cells in the spleens of 6-week old WT and *MRI*$^{-/-}$ mice. **(J)** Quantification of mature B and T cells in the spleen. All data are mean ± SEM (n = 5).

A

MRI	*XLF*	Expected	Actual
+/+	+/+	10	9
+/+	+/-	19	22
+/+	-/-	10	10
+/-	+/+	19	30
+/-	+/-	38	34
+/-	-/-	19	15
-/-	+/+	10	14
-/-	+/-	19	20
-/-	-/-	10	0
Total			**154**

B

MRI	*XLF*	Expected	Actual
-/-	+/+	28	35
-/-	+/-	56	77
-/-	-/-	28	0
Total			**112**

C

E14.5			
MRI	*XLF*	Expected	Actual
-/-	+/+	5	7
-/-	+/-	9	7
-/-	-/-	5	5
Total			**19**

E16.5			
MRI	*XLF*	Expected	Actual
-/-	+/+	6	2
-/-	+/-	13	16
-/-	-/-	6	7
Total			**25**

D

MRI$^{-/-}$ *XLF*$^{-/-}$:*MRI*$^{-/-}$

E

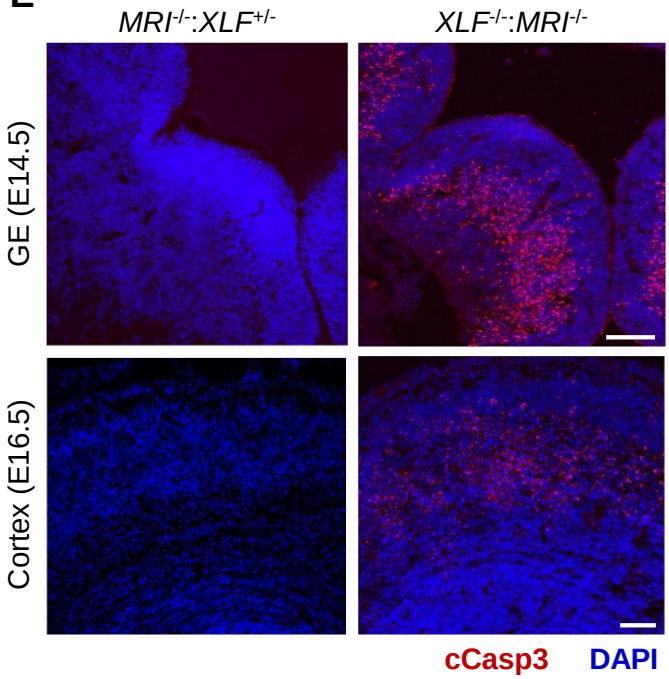

Figure 8

Figure 8: Combined XLF/MRI deficiency is embryonically lethal in mice. (A) Numbers of live births produced from intercrossing $XLF^{+/-}$:$MRI^{+/-}$ mice. **(B)** Numbers of live births produced from intercrossing $XLF^{+/-}$:$MRI^{-/-}$ mice. **(C)** Numbers of mice from $XLF^{+/-}$:$MRI^{-/-}$ intercrosses at embryonic days 14.5 (top) and 16.5 (bottom). **(D)** Photograph of $MRI^{-/-}$ and $XLF^{-/-}$:$MRI^{-/-}$ littermates at embryonic day 16.5. Scale bar, 1 cm. **(E)** Representative micrographs of the ganglionic eminence (GE, top row) and cortex (bottom row) in $XLF^{+/-}$:$MRI^{-/-}$ and $XLF^{-/-}$:$MRI^{-/-}$ mice at embryonic days 14.5 and 16.5, respectively, stained with DAPI (blue) and anti-cleaved caspase 3 antibody (red). Scale bar, 100 μm.

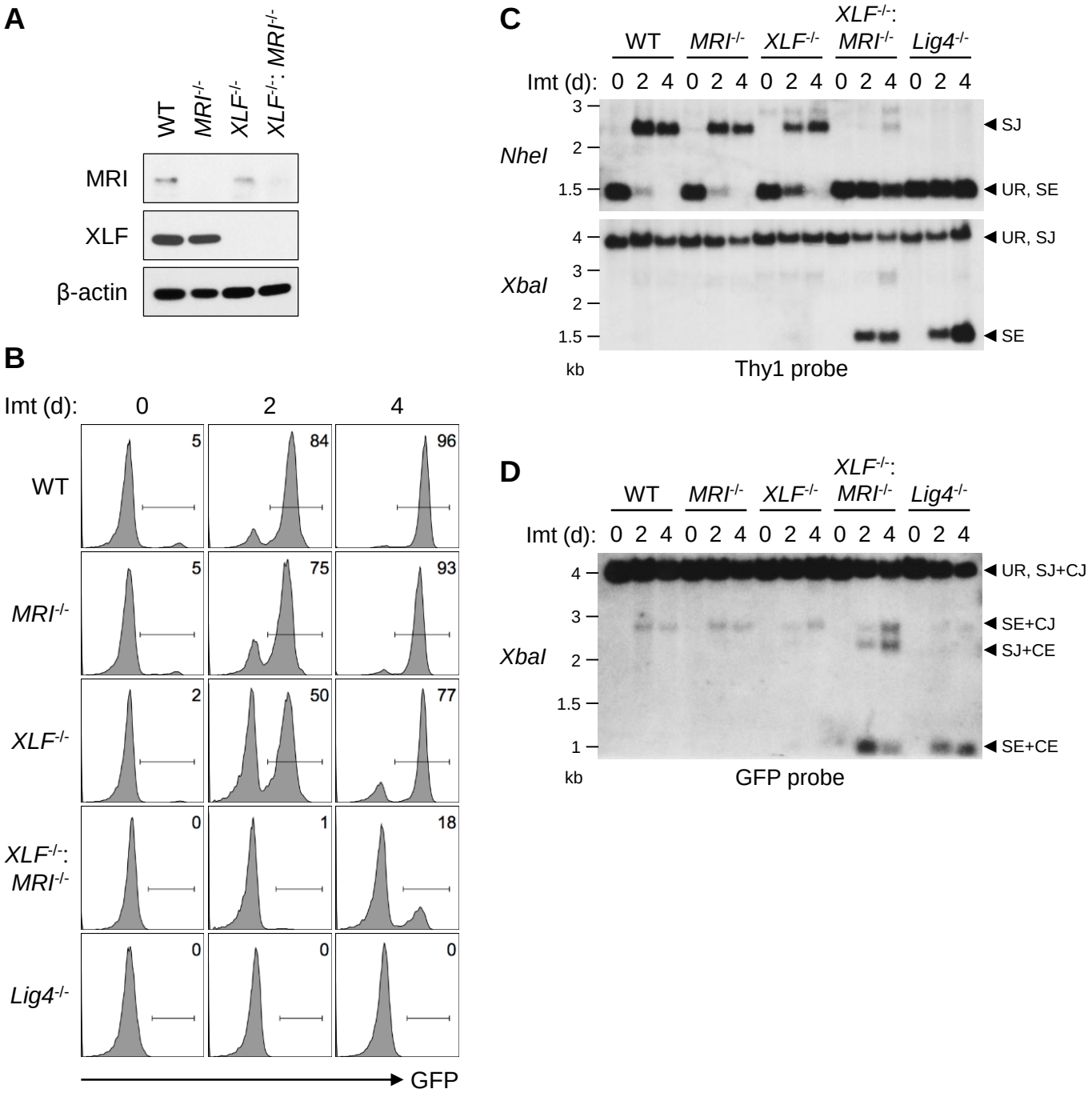
A
WT
MRI-/-
XLF-/-
XLF-/-: MRI-/-
MRI
XLF
β-actin
B
Imt (d): 0 2 4
WT
MRI-/-
XLF-/-
XLF-/-: MRI-/-
Lig4-/-
5
84
96
5
75
93
2
50
77
0
1
18
0
0
0
GFP
C
WT
MRI-/-
XLF-/-
XLF-/-: MRI-/-
Lig4-/-
Imt (d): 0 2 4 0 2 4 0 2 4 0 2 4 0 2 4
NheI
3
2
1.5
SJ
UR, SE
XbaI
4
3
2
1.5
UR, SJ
SE
kb
Thy1 probe
D
WT
MRI-/-
XLF-/-
XLF-/-: MRI-/-
Lig4-/-
Imt (d): 0 2 4 0 2 4 0 2 4 0 2 4 0 2 4
XbaI
4
3
2
1.5
1
UR, SJ+CJ
SE+CJ
SJ+CE
SE+CE
kb
GFP probe

Figure 9

Figure 9: Combined XLF/MRI deficiency inhibits V(D)J end joining. (A) Western blot analysis of MRI and XLF in WT, *MRI*$^{-/-}$, *XLF*$^{-/-}$, and *XLF*$^{-/-}$:*MRI*$^{-/-}$ (generated by CRISPR/Cas9) Abl pre-B cells. β-actin is shown as a protein loading control. **(B)** Flow cytometric analysis of GFP expression in WT, *MRI*$^{-/-}$, *XLF*$^{-/-}$, *XLF*$^{-/-}$:*MRI*$^{-/-}$, and *Lig4*$^{-/-}$ Abl pre-B cells that were treated with imatinib (Imt) for the indicated lengths of time (days). **(C)** Southern blot analysis of genomic DNA from cells in (B) that were digested with *NheI* (top) or *XbaI* (bottom) and hybridized to the Thy1 probe. Bands that correspond to UR, SJs, and unrepaired SEs are indicated at the right. **(D)** Southern blot analysis of genomic DNA from cells in (B) that were digested with *XbaI* and hybridized to the GFP probe. Bands that correspond to UR, both SJs and CJs (SJ+CJ), both SEs and CEs (SE+CE), and either SEs or CEs (SE+CJ or SJ+CE) are indicated at the right. Molecular weights (kilobases) are also shown.

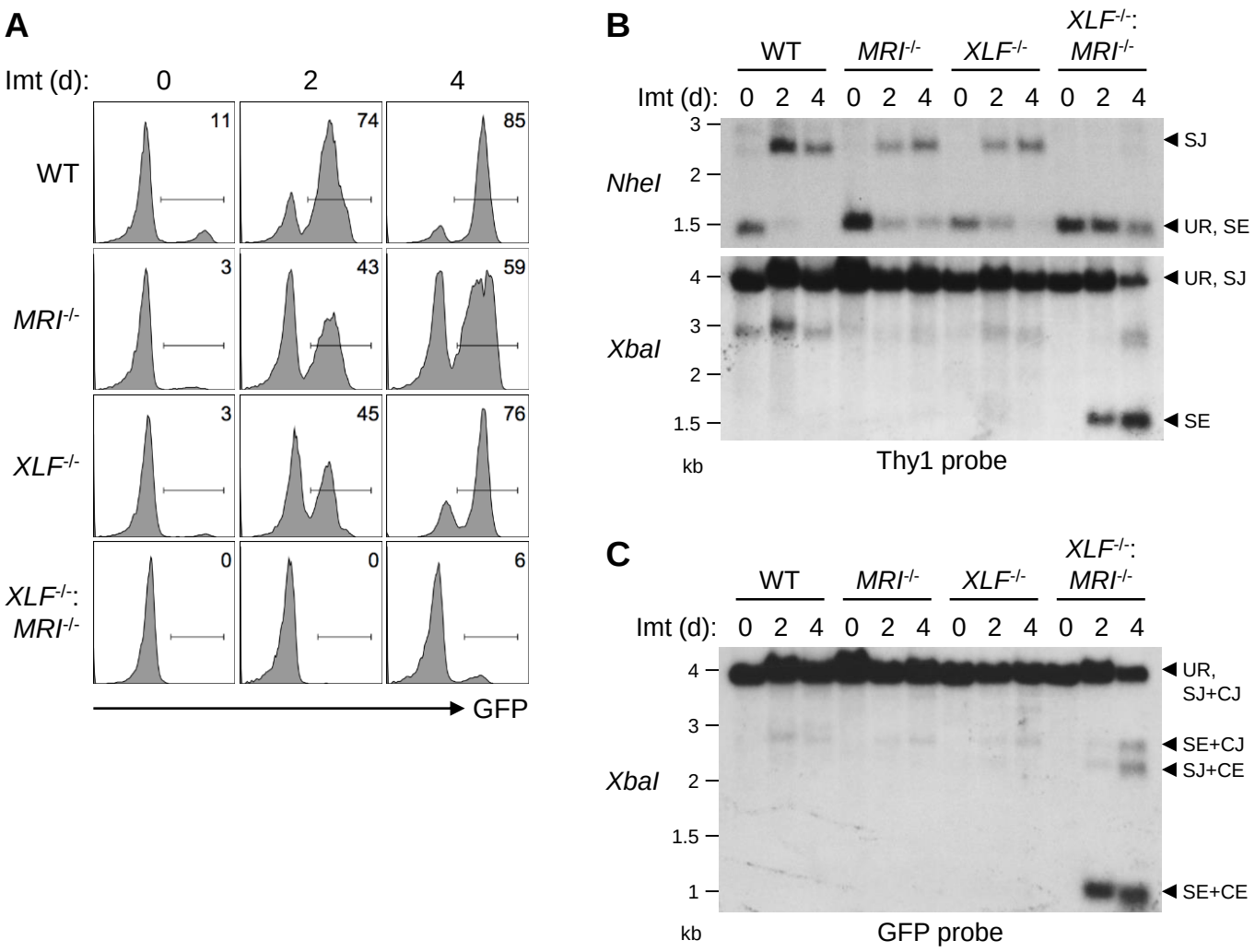
A
Imt (d): 0 2 4
WT
MRI-/-
XLF-/-
XLF-/-: MRI-/-
11
74
85
3
43
59
3
45
76
0
0
6
GFP
B
WT
MRI-/-
XLF-/-
XLF-/-: MRI-/-
Imt (d): 0 2 4 0 2 4 0 2 4 0 2 4
NheI
XbaI
3
2
1.5
4
3
2
1.5
SJ
UR, SE
UR, SJ
SE
kb
Thy1 probe
C
WT
MRI-/-
XLF-/-
XLF-/-: MRI-/-
Imt (d): 0 2 4 0 2 4 0 2 4 0 2 4
XbaI
4
3
2
1.5
1
UR, SJ+CJ
SE+CJ
SJ+CE
SE+CE
kb
GFP probe

Figure 10

Figure 10: Combined XLF/MRI deficiency inhibits V(D)J end joining (related to Figure 9). **(A)** Independent clones of WT, *MRI*$^{-/-}$, *XLF*$^{-/-}$, and *XLF*$^{-/-}$:*MRI*$^{-/-}$ Abl pre-B cells distinct from those presented in Figure 9 were treated with imatinib (Imt) for the indicated lengths of time (days) and assayed for GFP expression by flow cytometry **(B)** Southern blot analysis of genomic DNA from cells in (A) that were digested with *NheI* (top) or *XbaI* (bottom) and hybridized to the Thy1 probe. **(C)** Southern blot analysis of genomic DNA from cells in (A) that were digested with *XbaI* and hybridized to the GFP probe. Bands corresponding to different MGINV arrangements are indicated at the right as described in Figure 1. Molecular weights (kilobases) are also shown.

A

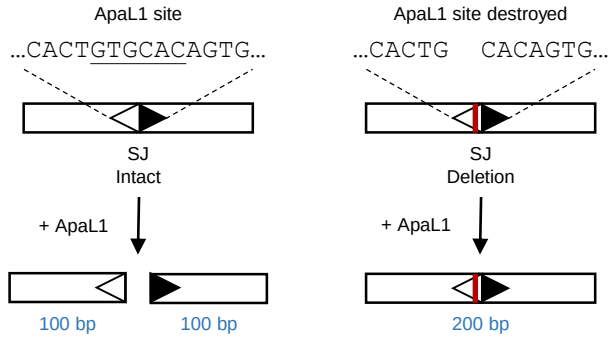

B

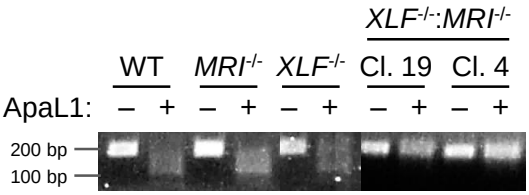

C

```
Ref: GTGGAGTACTAC CACTGTGCACAGTG CTACAGACTGGAACAAAAACAGA
XM1: GTGGAGTACTACCACTG                GAACAAAAACAGA
```

```
Ref: GTGGTTTTTGTACAGCCAGACAGTGGAGTACTACCACTGTGCACAGTGCTACAGACTGGAACAAAAACAGACCCTCGTTGG
XM2: GTG                                                                        GTTGG
```

```
Ref: TGGAGTACTACCACTGTGCACAGTGC
XM4: TGGAGTACTAC      CACAGTGC
```


Figure 11

Figure 11: Imprecise SJ formation in XLF/MRI double-deficient lymphocytes. (A) Schematic of an intact SJ (left), which forms an *ApaL1* restriction site at its junction, and an imprecise SJ (right), which contains a deletion that destroys the *ApaL1* restriction site. PCR products covering an intact SJ can be digested by *ApaL1* to yield two ~100-base pair fragments, whereas PCR products covering an imprecise SJ are resistant to *ApaL1* cleavage. **(B)** *ApaL1* digestion of PCR products spanning the SJ sequences in WT, $MRI^{-/-}$, $XLF^{-/-}$, and $XLF^{-/-}$:$MRI^{-/-}$ (two independent clones) Abl pre-B cells that were treated with imatinib for four days. **(C)** PCR sequencing of SJs formed in $XLF^{-/-}$:$MRI^{-/-}$ Abl pre-B cells (XM). A reference representing an intact SJ sequence is provided (Ref). The RSS heptamers that are joined together at a SJ are bolded, and nucleotides that constitute potential microhomologies are underlined.

Chapter 4: MRI is a Multivalent NHEJ Adaptor

4.1 Background

Originally identified in a mutagenesis screen as a factor that enables retroviral integration into mammalian cells, MRI has since been increasingly implicated in the regulation of NHEJ, but its function remains largely unknown (Agarwal S et al. 2006). In humans, MRI is encoded by the *C7orf49* gene and has three isoforms: MRI-1 produces the full-length, 157 aa-long protein that is highly conserved among mammalian species, while MRI-2 and MRI-3 generate shorter peptides that lack the first ~100 aa from the N-terminus and last ~50 aa from the C-terminus, respectively, of MRI-1 (Agarwal S et al. 2006, Arnoult N et al. 2017). MRI-1 appears to be the dominant form of MRI since it is expressed six to seven times more abundantly than MRI-2, whereas MRI-3 is translated at undetectable levels, as measured by western blot analysis of endogenously epitope-tagged MRI isoforms in the HT1080-6TG human fibrosarcoma cell-line (Arnoult N et al. 2017). On the other hand, in mice, MRI is encoded by the *3110062M04Rik* gene on chromosome 6 and has two splice variants, the first of which makes a 157 aa-long product that is homologous to the one in humans, while the second yields a 184 aa-long product that is identical to the first but with a ~20-aa insertion at position 74. Hereafter, we will focus on the 157 aa-long MRI peptide, as its transcript is the most evolutionarily preserved, and thus likely the most functionally relevant, of all the known isoforms. Available RNA-seq and protein expression data from the Human Protein Atlas (https://www.proteinatlas.org) the EBI Expression Atlas (https://www.ebi.ac.uk/gxa) reveal that MRI is ubiquitously present in different human and mouse tissues, with modest enrichment in lymphoid (bone marrow, spleen, thymus) and reproductive organs. Similarly, our preliminary analyses by western blot show that MRI protein expression is relatively higher in the spleens and

thymuses of adult WT mice (Figure 12).

Human MRI has been demonstrated to interact directly with Ku80 through a 16-base pair sequence (KBM) at its N-terminus that is similarly found in other Ku70/80-binding factors, such as the histone chaperone APLF and the DNA helicase WRN (Slavoff SA et al. 2014, Grundy GJ et al. 2016). Moreover, MRI forms complexes with DNA and Ku70/80 in vitro and can stimulate the ligation of radiolabeled DNA duplexes in Ramos (Burkitt's lymphoma) cell extracts in both a DNA-PKcs- and XRCC4-dependent manner, suggesting that it functions to promote DSB repair by NHEJ, a notion consistent with its previously described role in facilitating retroviral infection, as integration of foreign DNA into the host genome necessitates the generation and resolution of a DSB intermediate, usually via NHEJ (Skalka AM and Ratz RA 2005, Slavoff SA et al. 2014). However, a recent study has disputed this and proposed that MRI, which the authors renamed as cell cycle regulator of NHEJ (CYREN), specifically inhibits NHEJ during the S/G2 phases of the cell cycle by sequestering Ku70/80 from DSBs, thus biasing repair pathway choice towards HR: strikingly, depletion of MRI in HT1080 6TG cells with deprotected (shelterin-free) telomeres led to increased chromatid-type (S/G2), but not chromosome-type (G1), fusions mediated by NHEJ (Arnoult N et al. 2017). The authors reported that although MRI expression remained unchanged throughout the cell cycle, the MRI-Ku70/80 interaction peaked during S/G2, prompting them to conclude that MRI acts as a negative regulator of Ku70/80 activity; furthermore, by sequencing across different types of Cas9-induced DSBs in WT and *MRI*$^{-/-}$ cells, they found that the lengths of deletions at both 5' and 3' DNA overhangs were increased in the absence of MRI, suggesting that MRI also prevents the processing of single-stranded DNA ends to maintain a favorable local environment for HR (Arnoult N et al. 2017). On the contrary, in this chapter, we describe a novel role for MRI in augmenting the efficiency of NHEJ during G1.

4.2 MRI Promotes NHEJ-mediated DSB Repair

4.2.1 MRI Localizes to Sites of DNA Damage

To trace the localization of MRI in vivo, we generated a GFP-tagged MRI fusion protein (GFP-MRI) construct and expressed it in *MRI*$^{-/-}$ MEFs. GFP-MRI showed a predominantly pan-cellular distribution, as expected of small proteins <30 kDa, which can diffusely freely between the nucleus and cytoplasm through nuclear pore complexes (based on its peptide length, MRI has a predicted size of 17-kDa but runs at ~30-kDa on SDS-PAGE due to its high content of basic aa residues giving it an overall net positive charge) (Figure 13A-B, no IR) (Timney BL et al. 2016). However, MRI-GFP rapidly localized to sites of DNA damage induced by laser microirradiation within a minute and remained there in discrete foci for up to 45 minutes (Figure 13A-B, post-IR). Additionally, GFP-MRI localization coincided physically and kinetically with that of Ku80-RFP and occurred robustly even in serum-starved G1-phase MEFs, suggesting that MRI is involved in NHEJ-mediated repair at laser-induced DSBs (Figure 13A-C).

4.2.2 MRI Deficiency Compromises NHEJ

To verify that MRI functions in NHEJ, we performed survival assays on WT and *MRI*$^{-/-}$ MEFs exposed to different doses of IR. *MRI*$^{-/-}$ MEFs demonstrated increased radiosensitivity as compared to WT MEFs, though not to the same degree as *XLF*$^{-/-}$ MEFs, confirming that MRI is indeed required for DSB repair in mammalian cells (Figure 14A-B). Moreover, *MRI*$^{-/-}$ splenic B cells exhibited moderate, but consistent, defects in immunoglobulin CSR after stimulation with either lipopolysaccharide (LPS) or anti-CD40 plus interleukin-4 (IL-4) in vitro (Figure 15A-D). The absence of MRI in these cells did not affect AID expression or cell proliferation, suggesting

that the block in CSR had arisen during the repair of AID-induced DSBs – a step which is largely carried out through NHEJ (Figure 15E-F). Together, these results indicate that MRI plays a role specifically in NHEJ that helps to enhance the efficiency of the reaction.

4.3 MRI Forms Multimeric DDR Complexes

4.3.1 MRI Possesses Adaptor Features

The N- and C-terminal regions, including the KBM (aa 4-19) and XLM (aa 147-157), of MRI are highly conserved across species, especially among mammals, while the central region is relatively non-conserved (Figure 16A). In fact, the amino acid composition of the central region suggests that MRI is an intrinsically disordered peptide, which, with its conserved termini, could potentially act as an adaptor to bind and nucleate heterogeneous protein complexes (Wright PE and Dyson HJ 2015). To test this hypothesis, we generated recombinant mouse MRI from *E. coli* and analyzed the protein by hydrogen-deuterium (H/D) exchange-mass spectrometry (HDX-MS) in collaboration with Dr. Gaya Amarasinghe's lab at Washington University School of Medicine (Keppel TR et al. 2015). Pepsin digestion yielded peptic peptides encompassing 85% of the MRI protein; these peptides all exhibited high levels, averaging 50-100%, of deuterium uptake (Figure 16B). Kinetic analyses revealed that most of the peptides spanning the entire length of MRI had close to maximal deuterium uptake at the earliest time point observed (10 seconds) (Figure 16C). Collectively, these data demonstrate that MRI is intrinsically disordered in solution. Notably, the N-terminal peptides, including aa 1-25 which comprise the KBM, were more protected from H/D exchange (50-75%) than the rest, suggestive of a tendency to adopt secondary structures (Figure 16B-C). Indeed, while circular dichroism (CD) spectroscopy also showed that MRI is disordered, the addition of trifluoroethanol (TFE), a helix-inducing crowding agent, unexpectedly resulted in

CD spectra with helical characteristics, implicating that MRI has the potential to establish helical structures (Figure 16D) (Lopes JL et al. 2014). Finally, size-exclusion chromatography coupled with multi-angle light scattering (SEC-MALS) revealed that, in solution, MBP-tagged MRI can exist as a monomer, dimer, or multimer (Figure 16E). We reasoned that these structural features of MRI make it well-suited to recruiting and stabilizing multi-protein complexes during NHEJ.

4.3.2 MRI Binds Distinct DDR Proteins at Both Termini

Since MRI has physical properties resembling those of an adaptor, we sought to elucidate its function by determining its binding partners. To this end, we carried out immunoprecipitation coupled with mass spectrometry (IP-MS) analysis to identify proteins that associate with FLAG-HA-tagged versions of full-length MRI (MRI), MRI with a deletion of 17 N-terminal aa residues comprising the KBM ($MRI^{\Delta N}$), and MRI with a deletion of 15 C-terminal aa residues comprising the XLM ($MRI^{\Delta C}$) in WT Abl pre-B cells (Figure 16A and 17A-B). Remarkably, our IP-MS data revealed that MRI interacts with a diverse set of DDR proteins, including members of the NHEJ and ATM signaling pathways, preferentially at either its N- or C-terminus (Figure 17C and Table 1). Immunoprecipitation (IP) of endogenous MRI from WT Abl pre-B cell nuclear extracts using our anti-mouse MRI antibody subsequently confirmed many of these associations (Figure 17D). To further validate our IP-MS results, we expressed FLAG-HA-tagged MRI, $MRI^{\Delta N}$, $MRI^{\Delta C}$, or $MRI^{\Delta N\Delta C}$ in WT Abl pre-B cells and performed anti-HA IP of these proteins followed by western blotting. The canonical NHEJ factors, such as DNA-PKcs, Ku70/80, XLF, PAXX, and XRCC4, were pulled down with MRI or $MRI^{\Delta C}$, but not with $MRI^{\Delta N}$ or $MRI^{\Delta N\Delta C}$, indicating that they are bound to MRI through its N-terminal KBM (Figure 17E). Conversely, ATM, its substrate KAP-1, and all three components of the MRN complex (Mre11, RAD50, and Nbs1) were pulled down

with MRI or MRI$^{\Delta N}$, but not with MRI$^{\Delta C}$ or MRI$^{\Delta N\Delta C}$, indicating that they interact with MRI via its C-terminal XLM (Figure 17E). Notably, while MRI associates with ATM and its DSB sensor MRN and with DNA-PKcs and its DSB sensor Ku70/80, it does not appear to bind to the kinase ATR or its DSB sensor ATRIP, which are activated in response to replicative DNA damage (e.g. stalled or reversed replication forks), suggesting that MRI operates specifically in NHEJ (Figure 17F). Interestingly, although MRI, XLF, and PAXX all possess C-terminal XLMs and co-IP with the NHEJ factors DNA-PKcs, Ku70/80, and XRCC4, only MRI binds to ATM and MRN (Figure 17F). Instead, analogous to the KBM in MRI, the XLMs in XLF and PAXX had been previously shown to mediate their interactions with Ku70/80 (Yano K et al. 2011, Ochi T et al. 2015, Xing M et al. 2015). Therefore, like an adaptor, MRI can bind to, and potentially link together, distinct groups of proteins at its termini and likely plays a role separate from those of XLF and PAXX in NHEJ (see Section 4.4.1).

4.3.3 MRI Multi-protein Complexes

We explored the prospect that MRI could nucleate multimeric protein complexes in vivo by several different approaches. Since Ku70/80 binds to almost all of the known canonical NHEJ factors, we wondered whether it would be required for promoting any of the protein interactions with MRI. To address this question, we expressed FLAG-HA-tagged MRI in *Ku70*$^{-/-}$ Abl pre-B cells that are deficient in both Ku70 and Ku80 (as Ku monomers are unstable by themselves) and performed anti-HA IP to look at MRI-associated proteins in these cells. Remarkably, all the MRI N-terminal interactions, including those with DNA-PKcs, XLF, PAXX, and XRCC4, were lost in the absence of Ku70/80, while the C-terminal interactions with ATM, MRN, and KAP-1 were unperturbed (Figure 18A). Hence, MRI can form complexes with Ku70/80 and at least one other

NHEJ factor at its N-terminus. To extend our findings, we correspondingly pulled down FLAG-HA-tagged MRI in *Mre11*$^{A/A}$ Abl pre-B cells, which express a hypomorphic Mre11 product that is present at extremely low levels (RAD50 and Nbs1 are similarly destabilized when not part of the MRN complex) (Theunissen JW et al. 2003). However, MRN deficiency did not noticeably affect any MRI protein interactions, including that with ATM, whose recruitment to chromatin is essentially dependent on MRN (Figure 18A). In collaboration with Dr. Tanya Paull's lab at the University of Texas at Austin, we found that the MRI C-terminus binds directly to ATM in vitro, as removal of the XLM abolished this association, in agreement with our IP experiments (Figure 18B). The lack of DNA-PKcs or ATM also did not alter MRI protein interactions, indicating that DNA-PKcs is linked to MRI through Ku70/80 but not vice versa and that ATM and MRN could bind to MRI separately of one another, thereby raising the intriguing possibility that MRI exists in different protein complexes mediating distinct functions (Figure 18C).

To assess whether MRI can simultaneously interact with proteins at its N- and C-termini, we performed sequential IPs of Ku80 and MRI by expressing both FLAG-tagged Ku80 and HA-tagged MRI in *MRI*$^{-/-}$ Abl pre-B cells, purifying Ku80 complexes by anti-FLAG IP, and carrying out anti-HA IP on the Ku80 complexes to obtain Ku80 complexes that also contain MRI (Figure 18C). Western blot analysis revealed the presence of ATM in these Ku80/MRI complexes, along with DNA-PKcs and Ku70, indicating that MRI can concomitantly associate with Ku70/80 and DNA-PKcs at its N-terminus and with ATM at its C-terminus (Figure 18D). Consistent with this notion, size-exclusion chromatography (SEC) showed that MRI protein complexes in Abl pre-B cells migrated in fractions ranging from ~100 kDa to >1 mDa in size, with MRI itself being most abundant in the 200-kDa fractions with Ku70 only and in the >1-mDa fractions with DNA-PKcs, ATM, Mre11 (presumably MRN), and Ku70 (Figure 18E). Taken together, these results suggest

that MRI forms diverse multimeric complexes mediated through *cis*- (e.g. Ku70/80 and XRCC4) and *trans*- (Ku70/80 and ATM) interactions at its termini.

4.3.4 MRI Function Depends on Both the KBM and XLM

To clarify the requirements for the MRI N- and C-terminal protein interactions in NHEJ, we assayed V(D)J recombination in *XLF*$^{-/-}$:*MRI*$^{-/-}$ Abl pre-B cells reconstituted with XLF, MRI, MRI$^{\Delta N}$, MRI$^{\Delta C}$, or MRI$^{\Delta N\Delta C}$. Expression of XLF or MRI fully restored V(D)J recombination in *XLF*$^{-/-}$:*MRI*$^{-/-}$ Abl pre-B cells, as evidenced by the significantly increased percentages of GFP-positive after imatinib treatment (Figure 19A). Southern blot analysis confirmed that these cells were able to form SJs and CJs with barely any signs of unrepaired RAG DSBs (Figure 19B-C). In contrast, expression of MRI$^{\Delta N}$ or MRI$^{\Delta C}$ only partially reversed the V(D)J end joining defect, whereas expression of MRI$^{\Delta N\Delta C}$ had no effect at all (Figure 19A). Indeed, *XLF*$^{-/-}$:*MRI*$^{-/-}$ Abl pre-B cells transduced with the MRI$^{\Delta N}$, MRI$^{\Delta C}$, or MRI$^{\Delta N\Delta C}$ constructs still accumulated large amounts (albeit reduced with MRI$^{\Delta N}$ or MRI$^{\Delta C}$) of free SEs and CEs following imatinib treatment (Figure 19B-C). Therefore, we conclude that the protein interactions maintained by the N-terminal KBM and C-terminal XLM are necessary for distinct functions of MRI in NHEJ such that the loss of a terminal motif cannot be compensated for by the other.

4.4 The Functional Role of MRI in NHEJ

4.4.1 MRI is Functionally Distinct from XLF

Since MRI has a XLM in its C-terminus like XLF and operates redundantly with XLF in NHEJ, we asked whether MRI and XLF perform overlapping activities in DSB repair, reasoning that if they did, then the requirements for efficient V(D)J end joining should be similar in *XLF*$^{-/-}$

and *MRI*$^{-/-}$ Abl pre-B cells. However, while ATM kinase inhibition blocked V(D)J recombination in *XLF*$^{-/-}$ Abl pre-B cells as previously described, it had only similarly modest effects on WT and *MRI*$^{-/-}$ Abl pre-B cells (Figure 20A) (Zha S et al. 2011). Indeed, in contrast to *XLF*$^{-/-}$:*ATM*$^{-/-}$ mice, which present with a SCID phenotype, *MRI*$^{-/-}$:*ATM*$^{-/-}$ mice displayed minor defects in lymphocyte development resembling those of *ATM*$^{-/-}$ mice, clearly demonstrating that MRI, unlike XLF, does not function redundantly with ATM signaling (data not shown) (Zha S et al. 2011). Likewise, we and others had established that XLF/PAXX double-deficiency greatly impairs V(D)J end joining in lymphocytes (Balmus G et al. 2016, Kumar V et al. 2016, Lescale C et al. 2016, Tadi SK et al. 2016, Hung PJ et al. 2017, Liu X et al. 2017, Abramowski V et al. 2018). As PAXX also bears a C-terminal XLM, we thought it would be more probable that MRI and PAXX carry out the same general function which can compensate for XLF. To test this possibility, we used CRISPR/Cas9 to excise the entire *PAXX* coding region in *MRI*$^{-/-}$ Abl pre-B cells to generate *MRI*$^{-/-}$:*PAXX*$^{-/-}$ Abl pre-B cells (Figure 20B-C). However, whereas *XLF*$^{-/-}$:*PAXX*$^{-/-}$ Abl pre-B cells exhibited a severe block in V(D)J recombination, *MRI*$^{-/-}$:*PAXX*$^{-/-}$ Abl pre-B cells were able to rearrange the MGINV substrate as efficiently as WT, *MRI*$^{-/-}$, and *PAXX*$^{-/-}$ Abl pre-B cells following imatinib treatment (Figure 20D). Moreover, while unrepaired SEs and CEs were readily detected in *XLF*$^{-/-}$:*PAXX*$^{-/-}$ Abl pre-B cells, there were no apparent indications of residual RAG DSBs in *MRI*$^{-/-}$:*PAXX*$^{-/-}$ Abl pre-B cells at four days post-treatment, as determined by Southern blot analysis (Figure 20E-G). Thus, *MRI*$^{-/-}$ Abl pre-B cells do not share the dependencies of *XLF*$^{-/-}$ Abl pre-B cells on ATM and PAXX, suggesting that MRI has unique functions that distinguish it from XLF in NHEJ.

4.4.2 MRI Deficiency Does Not Impair DDR Signaling

Since MRI interacts with the two major DDR kinases ATM and DNA-PKcs, we surmised

that it might play a role in regulating the DDR signaling pathway. To explore this hypothesis, we irradiated G1-phase WT and *MRI*$^{-/-}$ Abl pre-B cells and analyzed by western blot the ATM- and DNA-PKcs-dependent phosphorylations of H2AX at serine 139 (γ-H2AX) and KAP-1 at serine 824; however, there were no significant differences in the induction or resolution of γ-H2AX and phospho-KAP-1 signals between WT and *MRI*$^{-/-}$ Abl pre-B cells (Figure 21A-C). Similar results were also observed for WT and *MRI*$^{-/-}$ MEFs, indicating that the absence of MRI has no effect on ATM or DNA-PKcs activity, though our assay is admittedly limited to these two readouts due to the lack of specific antibodies which can detect DNA damage-induced phosphorylation events in mouse cells (data not shown). We therefore looked at another clear outcome of ATM activation: the enforcement of the G2/M checkpoint (Xu B et al. 2001). Prior to irradiation, the frequencies of WT, *MRI*$^{-/-}$, and *ATM*$^{-/-}$ Abl pre-B cells entering mitosis were comparable (~2%), as measured by flow cytometric analysis of total DNA content and phospho-histone H3 (at serine 10) (Figure 21D). After being exposed to a low dose of IR, *MRI*$^{-/-}$ Abl pre-B cells, like WT Abl pre-B cells, exhibited a robust G2/M checkpoint, with considerably less percentages of cells able to undergo mitosis, while *ATM*$^{-/-}$ Abl pre-B cells showed little to no change in the proportion of mitotic cells, signifying that the ATM-dependent G2/M checkpoint is not disrupted by the loss of MRI (Figure 21D). Taken together, these observations suggest that MRI, like XLF and PAXX, is not required for the initiation or transduction of DDR signaling in mammalian cells (Zha S et al. 2011, Liu X et al. 2017).

4.4.3 MRI Promotes the Association of DDR Proteins on Chromatin

Since MRI interacts with the DSB sensors Ku70/80 and MRN, which bind to DNA ends and subsequently enlist other DDR proteins to chromatin, we speculated that MRI could function

in the recruitment or retention of its associated factors at DSBs. To examine this possibility, we isolated chromatin fractions from G1-phase WT and *MRI*$^{-/-}$ Abl pre-B cells before and after being exposed to IR. Western blot analysis revealed that MRI deficiency markedly impaired the ability of DNA-PKcs, Ku70, XLF, PAXX, XRCC4, and MRN to assemble on chromatin in response to DNA damage without affecting the overall stability of these proteins (Figure 22A). On the other hand, MRI deficiency did not affect the association of MDC1 with chromatin. This could be due to the fact that, unlike the other mentioned DDR proteins, MDC1 spreads extensively away from the site of the lesion, so that the loss of MDC1 locally at DSBs has negligible impact on the total amount of MDC1 on chromatin. It is equally probable that not all DDR proteins require MRI for their engagement with DNA: in this regard, MDC1 binds directly to γ-H2AX and can be tethered to chromatin through this interaction alone (Stucki M et al. 2005). Consistent with our chromatin fractionation results, Ku70-GFP showed diminished localization to laser-induced DSBs in *MRI*$^{-/-}$ MEFs as compared to WT MEFs (Figure 22B). We conclude that MRI helps to retain other DDR proteins, including the core NHEJ factors Ku70/80 and XRCC4, near DSBs to facilitate efficient NHEJ (discussed below).

4.5 Conclusion

Although MRI has been most recently implicated as a S/G2-specific inhibitor of NHEJ in a human fibrosarcoma cell-lines with deprotected telomeres, we find here that it promotes NHEJ-mediated DSB repair in G1-phase mouse lymphocytes and MEFs, as highlighted by several key lines of experimental evidence. First, as we had shown in the previous chapter, MRI is necessary for V(D)J end joining in *XLF*$^{-/-}$ Abl pre-B cells, indicating it is essential for NHEJ in suboptimal settings. Moreover, *XLF*$^{-/-}$:*MRI*$^{-/-}$ mice display an embryonically lethal phenotype reminiscent of

those presented by other NHEJ-deficient mice. Second, loss of MRI in MEFs leads to increased radiosensitivity and in naive B cells leads to a modest reduction in CSR efficiency, both of which are hallmarks of defective NHEJ. Third, MRI interacts with diverse DDR factors, including those involved in NHEJ and ATM signaling, at each of its termini and thus promotes the association of these proteins with chromatin at DSBs. The N- and C-terminal protein interactions are distinctly required for MRI function in NHEJ, as MRI mutants lacking either the KBM or XLM could only partially restore V(D)J end joining in *XLF*$^{-/-}$:*MRI*$^{-/-}$ Abl pre-B cells. We propose a model in which proteins bound to MRI at one of its termini are stabilized on DNA via the chromatin associations formed by proteins at the other terminus of MRI (Figure 22C). Thus, by means of its various *cis*- and *trans*- protein interactions, MRI can increase the avidity of its binding partners for chromatin and nucleate the protein components necessary for efficient DSB repair. How this is achieved in the context of DNA damage and its implications for the regulation of NHEJ is an emerging topic of interest in our lab. We remain open to the scenario that MRI could perform opposing activities in G1 and S/G2, and we are currently further investigating this possibility by assaying the repair of restriction enzyme-induced DSBs in G1- versus G2-phase cells. Alternatively, MRI may play different roles at RAG and genotoxic DSBs than at uncapped telomeres. We will provide a more thorough discussion of this discrepancy in the next chapter.

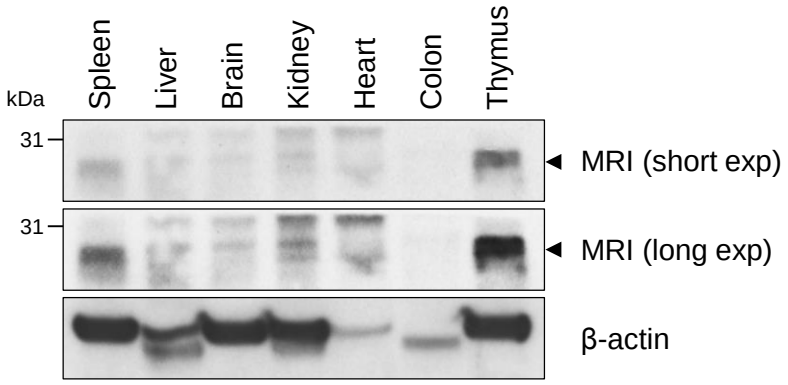
Spleen
Liver
Brain
Kidney
Heart
Colon
Thymus
kDa
31
31
MRI (short exp)
MRI (long exp)
β-actin

Figure 12

Figure 12: MRI protein expression in mouse tissues. Western blot analysis of MRI in the indicated mouse tissue lysates. Equal amounts of protein, as determined by Bradford assay, were loaded into each lane. β-actin is shown as an intended protein loading control, though it is clearly expressed at varying levels with different post-translational modifications in each tissue. This is preliminary data that we are currently trying to optimize.

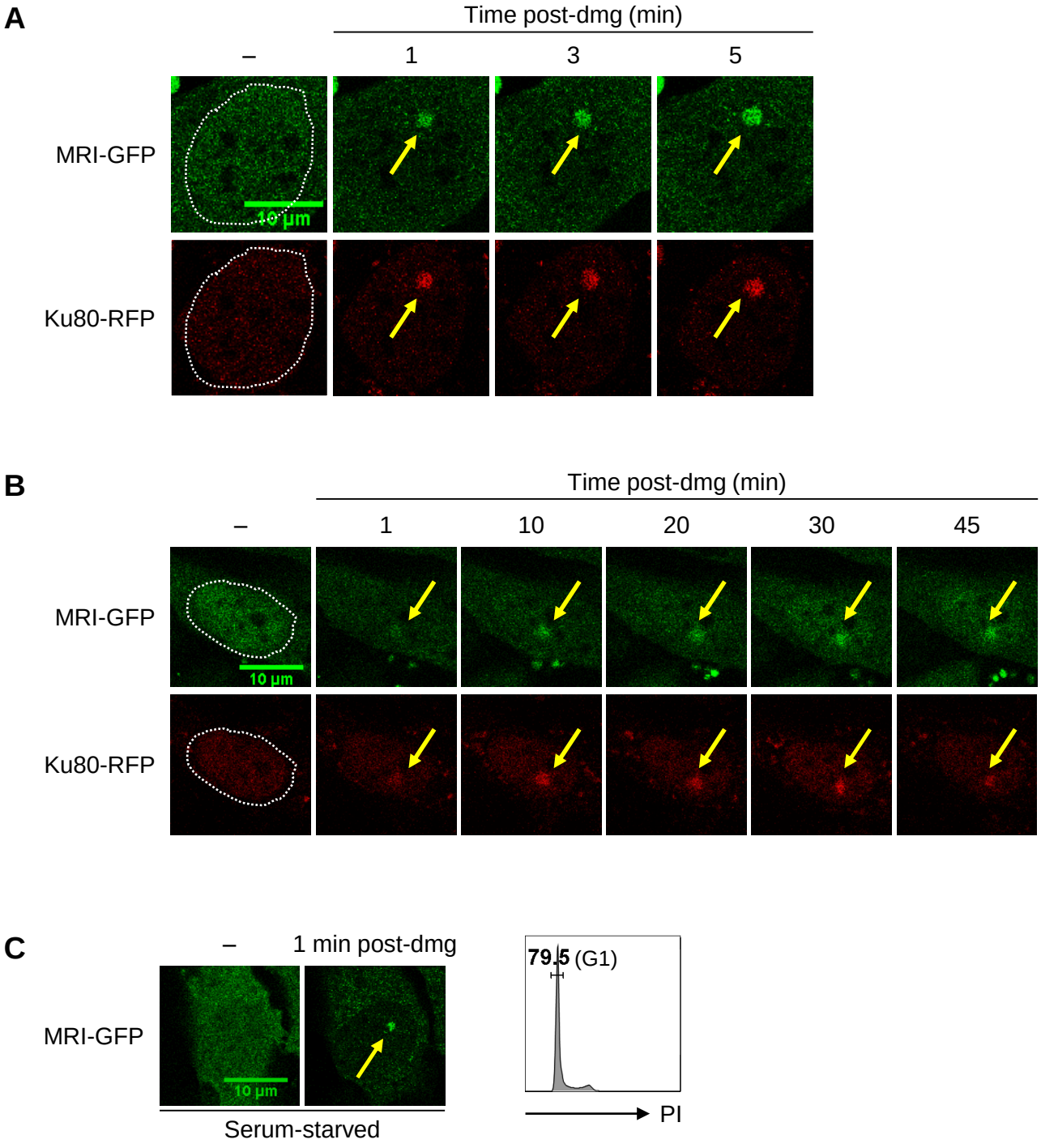
A
Time post-dmg (min)
–
1
3
5
MRI-GFP
Ku80-RFP
10 µm
B
Time post-dmg (min)
–
1
10
20
30
45
MRI-GFP
Ku80-RFP
10 µm
C
–
1 min post-dmg
MRI-GFP
10 µm
Serum-starved
79.5 (G1)
PI

Figure 13

Figure 13: MRI is recruited to DSBs. (A and B) Representative time-lapse micrographs of MRI-GFP and Ku80-RFP recruitment to a site of laser-induced DNA damage (designated by a yellow arrow) in *MRI*$^{-/-}$ MEFs at the indicated times post-damage (minutes). The dotted lines mark the nuclear boundaries. **(C)** Time-lapse micrographs of MRI-GFP localization to a laser-induced DNA damage site in serum-starved *MRI*$^{-/-}$ MEFs (top); flow cytometric analysis of cell cycle phase, as indicated by DNA content, in serum-starved MEFs (bottom).

A

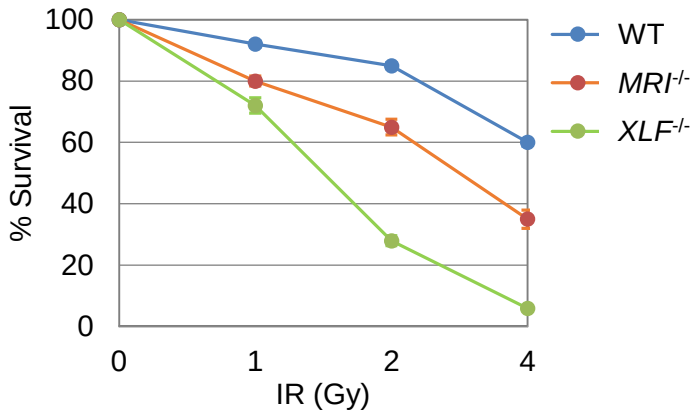
100
80
60
40
20
0
% Survival
0
1
2
4
IR (Gy)
WT
MRI-/-
XLF-/-

B

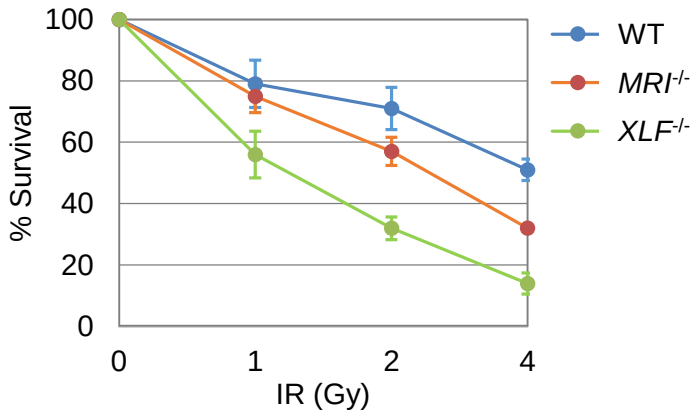
100
80
60
40
20
0
% Survival
0
1
2
4
IR (Gy)
WT
MRI-/-
XLF-/-

Figure 14

Figure 14: MRI deficiency leads to increased radiosensitivity in MEFs. (A and B) Percent survival of WT, *MRI*$^{-/-}$, and *XLF*$^{-/-}$ MEFs four days after exposure to the indicated doses of IR, as determined by PrestoBlue reagent. Cell-lines derived from different mice are shown in each panel. Data are mean ± SEM (n = 3).

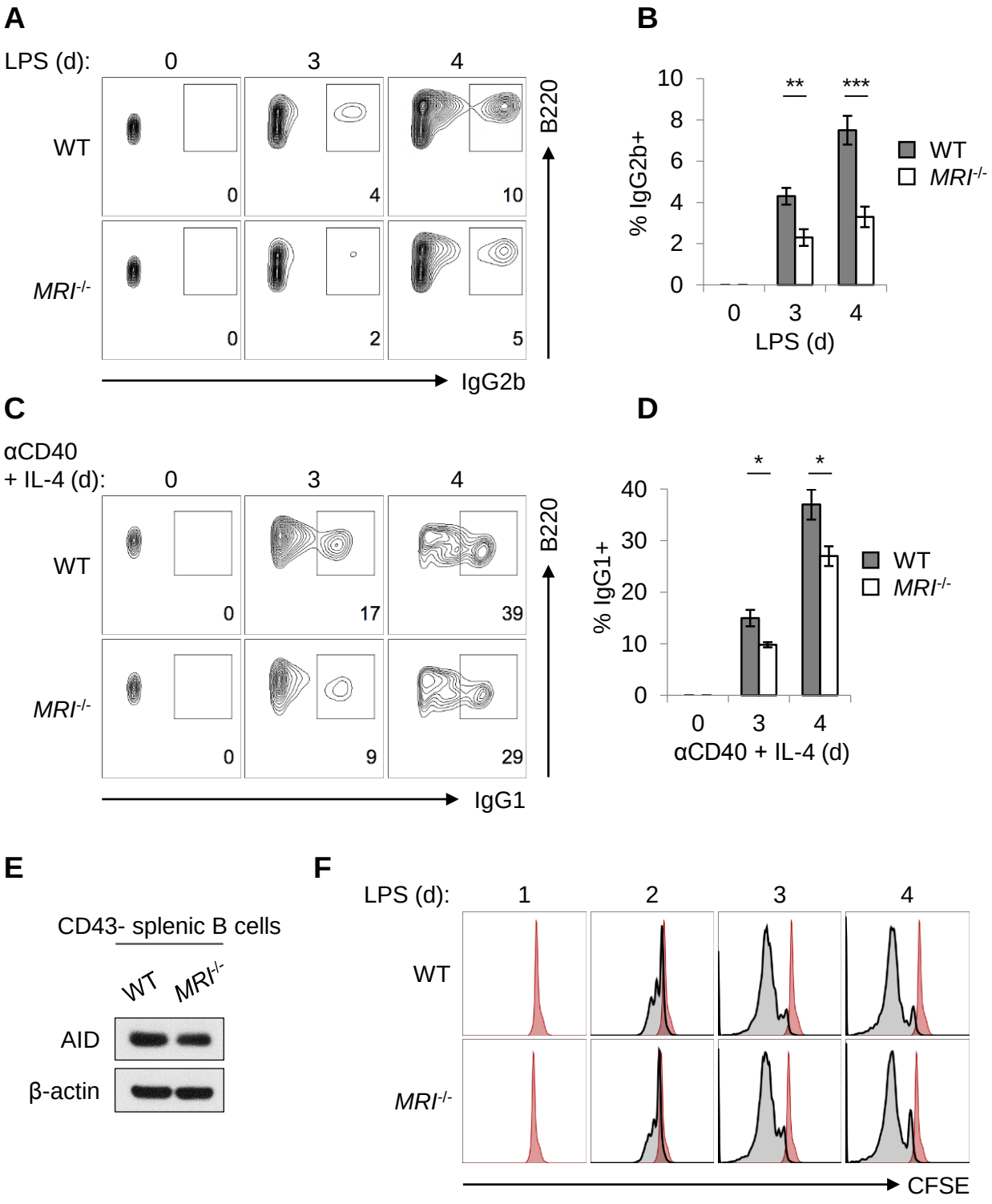
A
LPS (d):
0
3
4
WT
MRI-/-
0
4
10
0
2
5
B220
IgG2b
B
10
8
6
4
2
0
% IgG2b+
**
***
WT
MRI-/-
0
3
4
LPS (d)
C
αCD40
+ IL-4 (d):
0
3
4
WT
MRI-/-
0
17
39
0
9
29
B220
IgG1
D
40
30
20
10
0
% IgG1+
*
*
WT
MRI-/-
0
3
4
αCD40 + IL-4 (d)
E
CD43- splenic B cells
WT
MRI-/-
AID
β-actin
F
LPS (d):
1
2
3
4
WT
MRI-/-
CFSE

Figure 15

Figure 15: MRI-deficient B cells exhibit a CSR defect. (A) Flow cytometric analysis of IgG2b class-switching in WT and *MRI*$^{-/-}$ CD43^{-} splenic B cells stimulated with LPS for 3-4 days. **(B)** Quantification of IgG2b+ cells after stimulation with LPS for the indicated lengths of time. Data are mean ± SEM (n = 6). * P <0.05, ** P <0.01, *** P <0.005. **(C)** Flow cytometric analysis of IgG1 class-switching in WT and *MRI*$^{-/-}$ CD43^{-} splenic B cells stimulated with anti-CD40 and IL-4 for 3-4 days. **(D)** Quantification of IgG1+ cells after stimulation with anti-CD40 and IL-4 for the indicated lengths of time (n = 4). **(E)** Western blot analyses of AID in WT and *MRI*$^{-/-}$ B cells after stimulation with LPS for four days. β-actin is shown as a protein loading control. **(F)** Flow cytometric analysis of CFSE dilution in WT and *MRI*$^{-/-}$ B cells that were stimulated with LPS for the indicated lengths of time. The Day 1 histogram (red) is provided at each time point for reference.

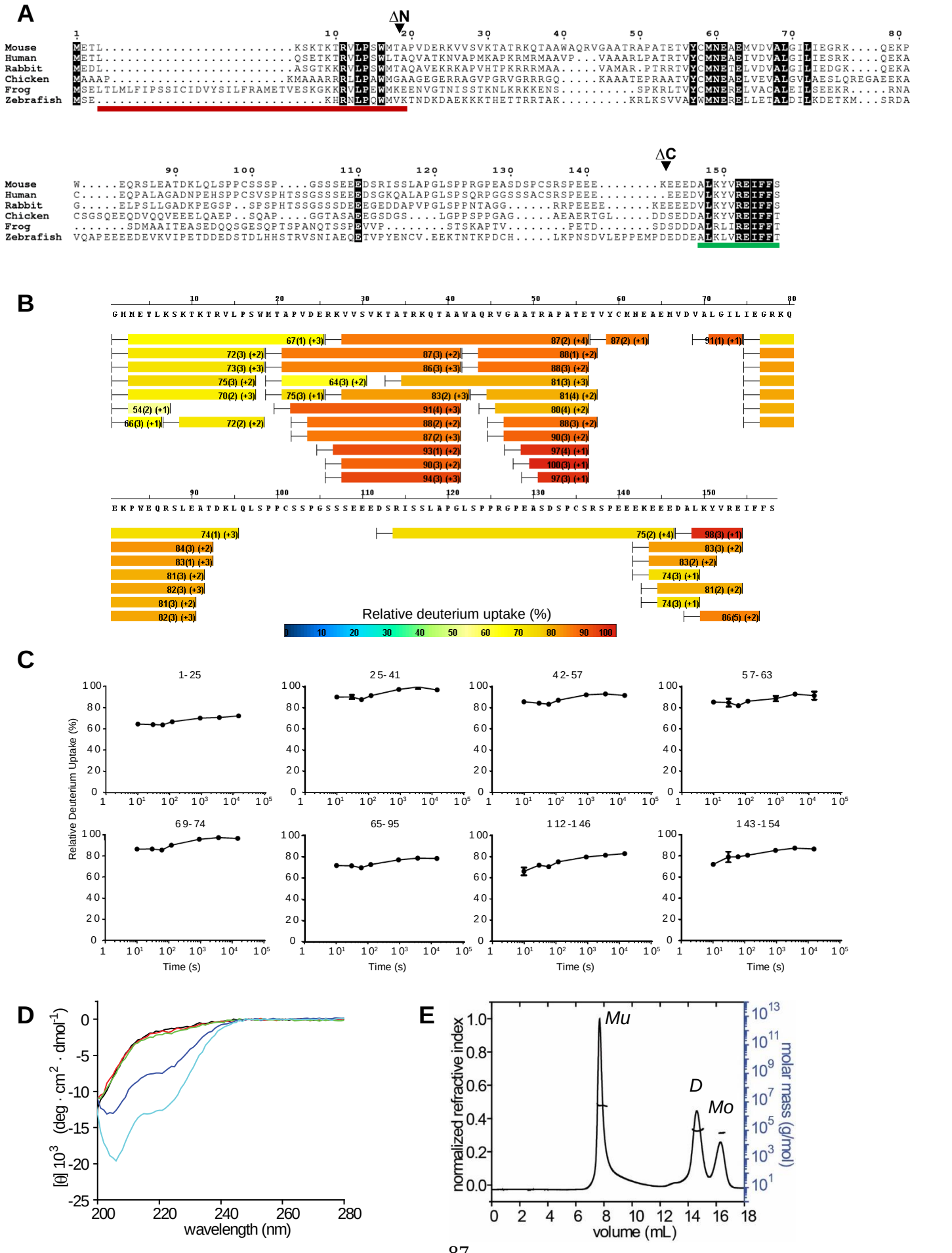
A
ΔN
ΔC
Mouse
Human
Rabbit
Chicken
Frog
Zebrafish
B
Relative deuterium uptake (%)
C
1-25
25-41
42-57
57-63
69-74
65-95
112-146
143-154
Relative Deuterium Uptake (%)
Time (s)
D
[θ] 10^3 (deg · cm^2 · dmol^-1)
wavelength (nm)
E
normalized refractive index
molar mass (g/mol)
volume (mL)
Mu
D
Mo

Figure 16

Figure 16: MRI has structural features of an adaptor. (A) Alignment of the MRI protein sequence across different species. The KBM and XLM are indicated by red and green lines, respectively. The black arrows specify the positions of the aa truncations in $MRI^{\Delta N}$ and $MRI^{\Delta C}$ (mentioned later in the text). Conserved aa residues are shaded in black. **(B)** Hydrogen-deuterium exchange dynamics of MRI. Bars underlining the aa sequence indicate the peptide fragments resolved by mass spectrometry. Numbers displayed in each bar represent the average deuterium percentage over seven incubation times, standard deviation, and peptide charge, respectively. The color code represents the percentage of average deuterium uptake (see legend). **(C)** Representative deuterium uptake curves for select peptic MRI peptides over seven time points (10, 30, 60, 120, 900, 3600, and 14400 seconds). **(D)** Circular dichroism uptake measurements of the mean residue ellipticity for MRI in the absence (black) or presence of 5% (red), 10% (green), 25% (blue), or 50% (cyan) TFE. **(E)** Analysis by SEC-MALS reveals that MRI elutes as three species: 5,550 ± 16 kDa (multimer, *Mu*), 111 ± 7.8 kDa (dimer, *D*), and 62.1 ± 3.7 kDa (monomer, *Mo*). Data shown are representative of at least three independent experiments.

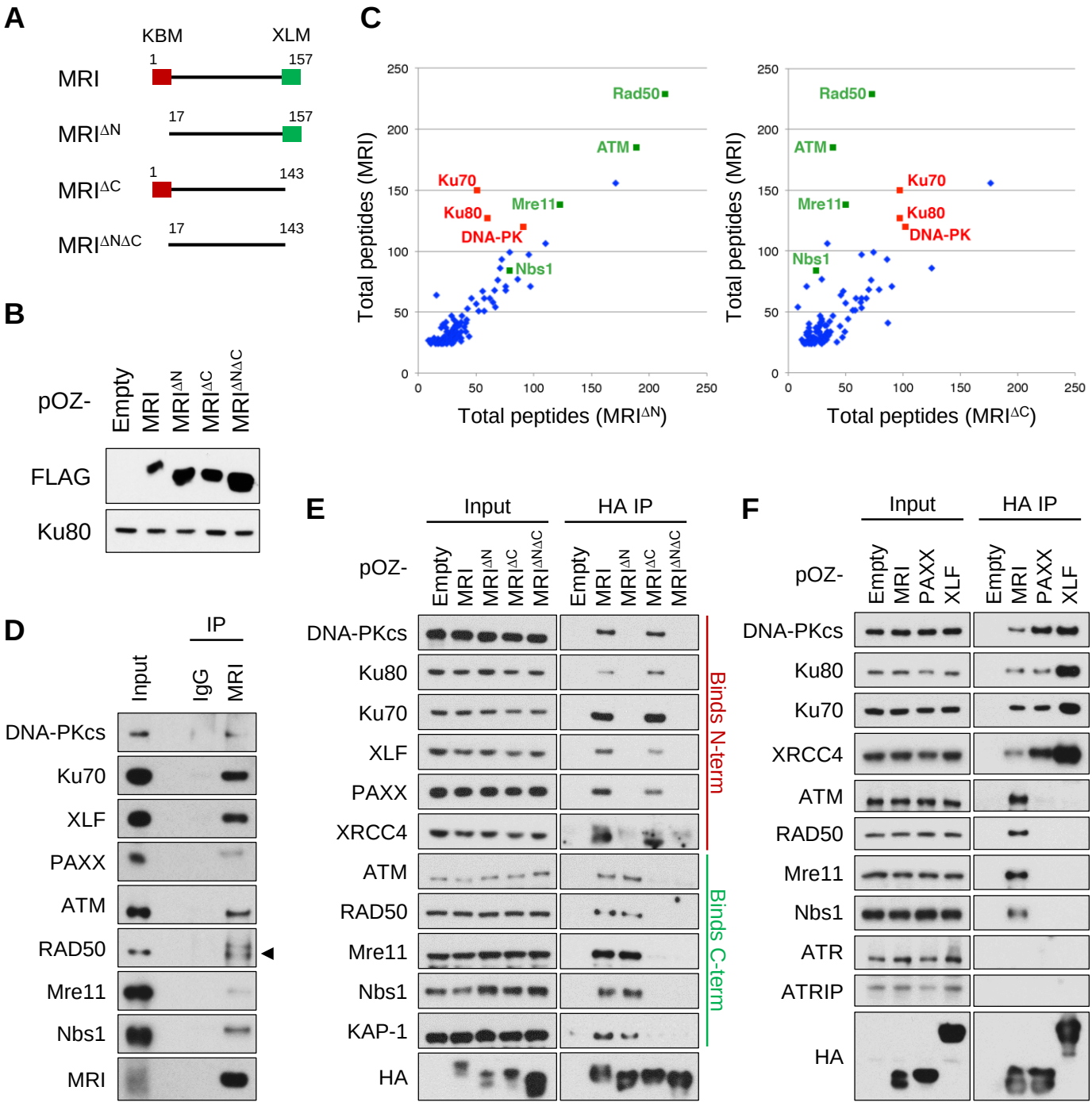
A
KBM
XLM
MRI
MRIΔN
MRIΔC
MRIΔNΔC
1
157
17
143
B
pOZ-
Empty
MRI
MRIΔN
MRIΔC
MRIΔNΔC
FLAG
Ku80
C
Total peptides (MRI)
Total peptides (MRIΔN)
Total peptides (MRIΔC)
Rad50
ATM
Ku70
Mre11
Ku80
DNA-PK
Nbs1
D
IP
Input
IgG
MRI
DNA-PKcs
Ku70
XLF
PAXX
ATM
RAD50
Mre11
Nbs1
MRI
E
Input
HA IP
pOZ-
DNA-PKcs
Ku80
Ku70
XLF
PAXX
XRCC4
ATM
RAD50
Mre11
Nbs1
KAP-1
HA
Binds N-term
Binds C-term
F
Input
HA IP
pOZ-
Empty
MRI
PAXX
XLF
DNA-PKcs
Ku80
Ku70
XRCC4
ATM
RAD50
Mre11
Nbs1
ATR
ATRIP
HA

Figure 17

Figure 17: MRI interacts with diverse DDR proteins at its N- and C-termini. (A) Schematic of the MRI, MRI$^{\Delta N}$, MRI$^{\Delta C}$, and MRI$^{\Delta N\Delta C}$ proteins. The KBM (red box) and XLM (green box) are indicated. **(B)** Western blot analysis of retrovirally expressed FLAG-HA-tagged MRI, MRI$^{\Delta N}$, MRI$^{\Delta C}$, and MRI$^{\Delta N\Delta C}$ in *XLF*$^{-/-}$:*MRI*$^{-/-}$ Abl pre-B cells using anti-FLAG. Ku80 is shown as a protein loading control. **(C)** Scatter plots comparing the total numbers of peptides from MRI-associated proteins in WT Abl pre-B cells expressing MRI versus MRI$^{\Delta N}$ (left plot) or MRI$^{\Delta C}$ (right plot), as determined by mass spectrometry. **(D)** Western blot analysis of DDR proteins that co-immunoprecipitated with endogenous MRI in WT Abl pre-B cell nuclear extract using the 13E10.E12.C10 anti-MRI antibody. **(E)** Western blot analysis of DDR proteins that co-immunoprecipitated with FLAG-HA-tagged MRI, MRI$^{\Delta N}$, MRI$^{\Delta C}$, and MRI$^{\Delta N\Delta C}$ in WT Abl pre-B cell nuclear extract using anti-HA. **(F)** Western blot analysis of DDR proteins that co-immunoprecipitated with FLAG-HA-tagged MRI, PAXX, and XLF in WT Abl pre-B cell nuclear extract using anti-HA.

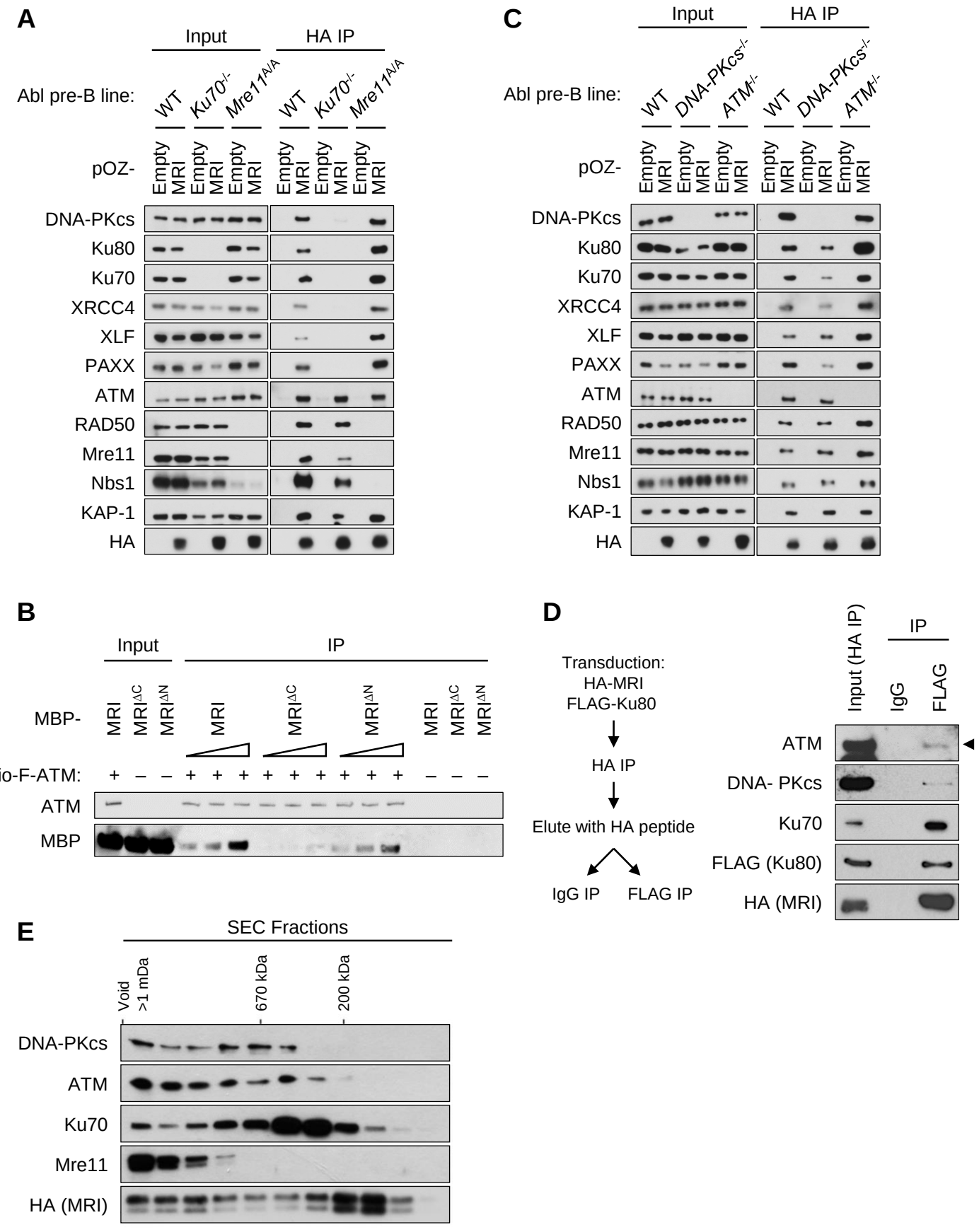
A
Input
HA IP
Abl pre-B line:
WT
Ku70-/-
Mre11A/A
pOZ-
Empty
MRI
DNA-PKcs
Ku80
Ku70
XRCC4
XLF
PAXX
ATM
RAD50
Mre11
Nbs1
KAP-1
HA
C
DNA-PKcs-/-
ATM-/-
B
MBP-
MRI
MRIΔC
MRIΔN
Bio-F-ATM:
ATM
MBP
D
Transduction:
HA-MRI
FLAG-Ku80
HA IP
Elute with HA peptide
IgG IP
FLAG IP
Input (HA IP)
IP
IgG
FLAG
DNA- PKcs
Ku70
FLAG (Ku80)
HA (MRI)
E
SEC Fractions
Void
>1 mDa
670 kDa
200 kDa

Figure 18

Figure 18: MRI forms multi-protein complexes. (A) Western blot analysis of DDR proteins that co-immunoprecipitated with FLAG-HA-tagged MRI in WT, *Ku70*$^{-/-}$, and *Mre11*$^{A/A}$ Abl pre-B cell nuclear extracts using anti-HA. **(B)** Western blot analysis of purified recombinant biotin-FLAG-ATM (bio-F-ATM) co-immunoprecipitated with 50 nM, 100 nM, or 200 nM of MBP-tagged human MRI, MRI$^{\Delta N}$, and MRI$^{\Delta C}$ proteins. **(C)** Western blot analysis of DDR proteins that co-immunoprecipitated with FLAG-HA-tagged MRI in WT, *DNA-PKcs*$^{-/-}$, and *ATM*$^{-/-}$ Abl pre-B cell nuclear extracts using anti-HA. **(D)** Schematic of sequential immunoprecipitations of MRI followed by Ku80 in cells expressing HA-MRI and FLAG-Ku80 (left). Western blot analysis of ATM, DNA-PKcs, Ku70, FLAG-Ku80, and HA-MRI from *MRI*$^{-/-}$ Abl pre-B cell nuclear extract after first immunoprecipitating with anti-HA (Input HA IP) and then immunoprecipitating with anti-FLAG or an IgG isotype control (right). **(E)** Western blot analysis of DDR proteins that associated with FLAG-purified MRI in different-sized fractions separated by a sucrose gradient column. Molecular weights of known markers (200 kDa and 670 kDa) are indicated.

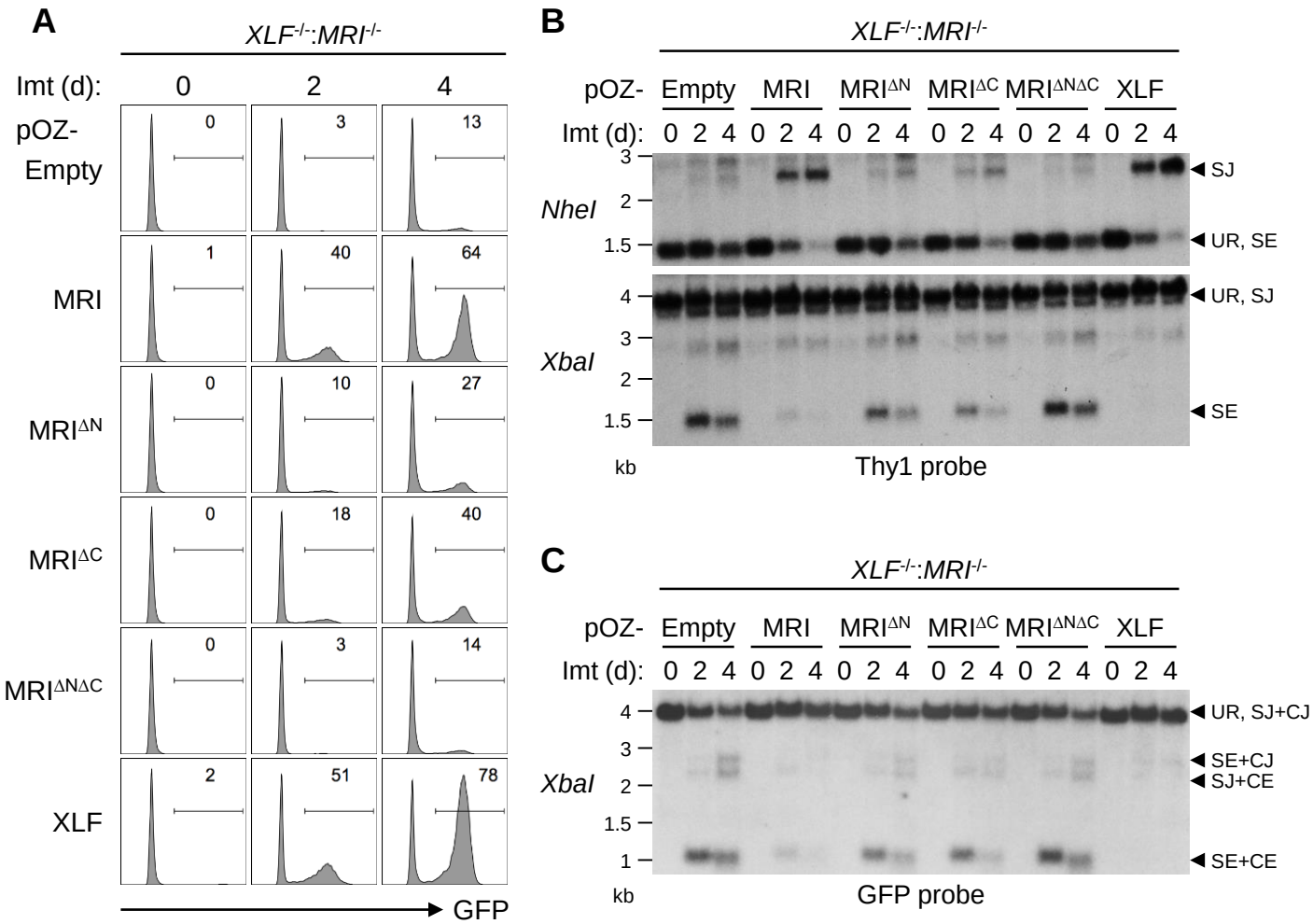
A
XLF-/-:MRI-/-
Imt (d): 0 2 4
pOZ-
Empty
MRI
MRIΔN
MRIΔC
MRIΔNΔC
XLF
0
3
13
1
40
64
0
10
27
0
18
40
0
3
14
2
51
78
GFP
B
XLF-/-:MRI-/-
pOZ- Empty MRI MRIΔN MRIΔC MRIΔNΔC XLF
Imt (d): 0 2 4 0 2 4 0 2 4 0 2 4 0 2 4 0 2 4
NheI
XbaI
3
2
1.5
4
3
2
1.5
kb
SJ
UR, SE
UR, SJ
SE
Thy1 probe
C
XLF-/-:MRI-/-
pOZ- Empty MRI MRIΔN MRIΔC MRIΔNΔC XLF
Imt (d): 0 2 4 0 2 4 0 2 4 0 2 4 0 2 4 0 2 4
XbaI
4
3
2
1.5
1
kb
UR, SJ+CJ
SE+CJ
SJ+CE
SE+CE
GFP probe

Figure 19

Figure 19: The N- and C-termini of MRI are both required for its function in NHEJ. (A) Flow cytometric analysis of GFP expression in *XLF*$^{-/-}$:*MRI*$^{-/-}$ Abl pre-B cells transduced with MRI, MRI$^{\Delta N}$, MRI$^{\Delta C}$, MRI$^{\Delta N\Delta C}$, or XLF and treated with imatinib (Imt) for the indicated lengths of time (days). **(B)** Southern blot analysis of genomic DNA from cells in (A) that were digested with *NheI* (top) or *XbaI* (bottom) and hybridized to the Thy1 probe. **(C)** Southern blot analysis of genomic DNA from cells in (A) that were digested with *XbaI* and hybridized to the GFP probe. Bands corresponding to different MGINV arrangements are indicated at the right as described in Figure 1. Molecular weights (kilobases) are also shown.

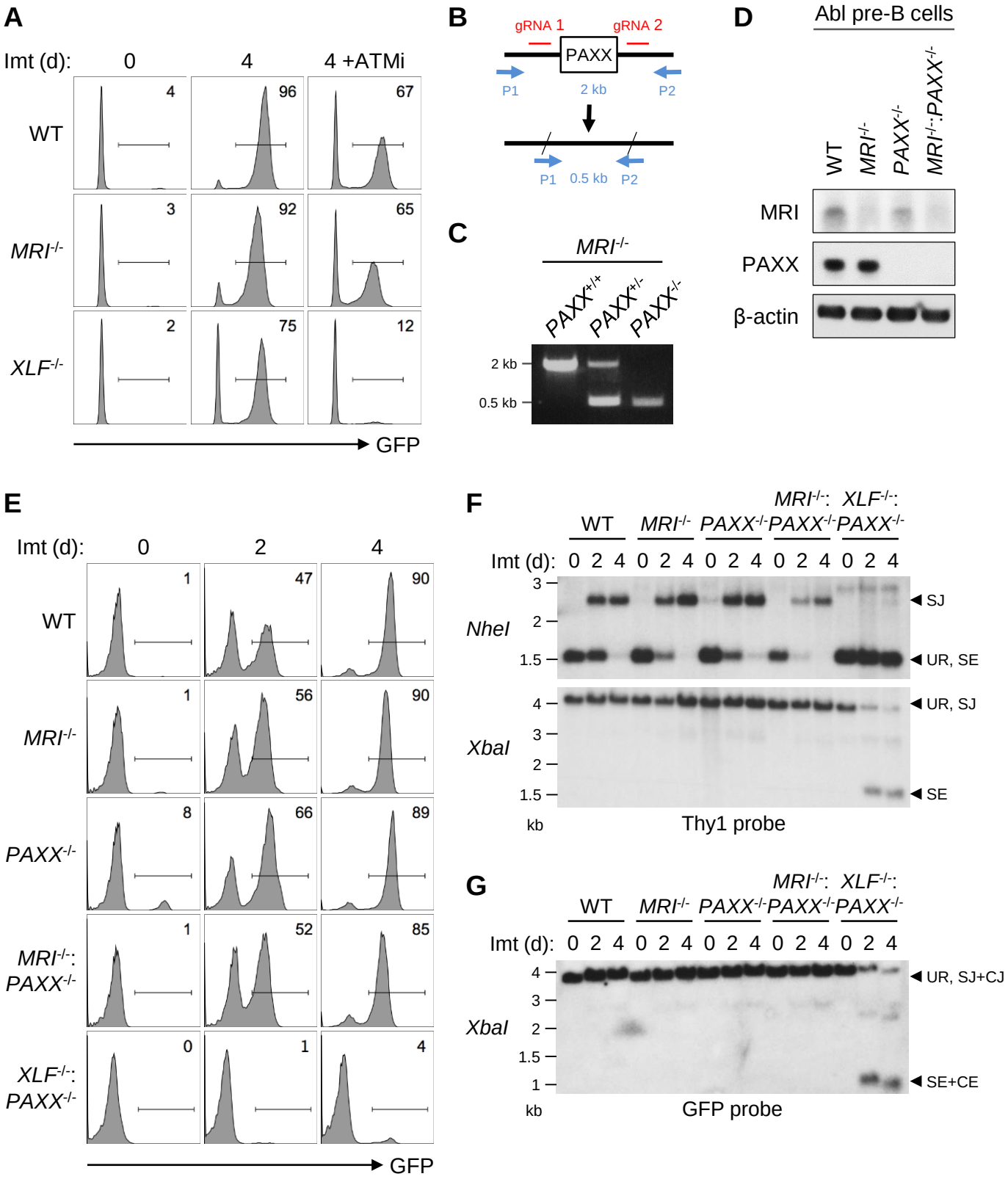
A
Imt (d): 0 4 4 +ATMi
WT
MRI-/-
XLF-/-
4
96
67
3
92
65
2
75
12
GFP
B
gRNA 1
gRNA 2
PAXX
P1
2 kb
P2
P1
0.5 kb
P2
C
MRI-/-
PAXX+/+
PAXX+/-
PAXX-/-
2 kb
0.5 kb
D
Abl pre-B cells
WT
MRI-/-
PAXX-/-
MRI-/-:PAXX-/-
MRI
PAXX
β-actin
E
Imt (d): 0 2 4
WT
MRI-/-
PAXX-/-
MRI-/-: PAXX-/-
XLF-/-: PAXX-/-
1
47
90
1
56
90
8
66
89
1
52
85
0
1
4
GFP
F
MRI-/-: XLF-/-:
WT MRI-/- PAXX-/- PAXX-/- PAXX-/-
Imt (d): 0 2 4 0 2 4 0 2 4 0 2 4 0 2 4
NheI
3
2
1.5
SJ
UR, SE
XbaI
4
3
2
1.5
UR, SJ
SE
kb
Thy1 probe
G
MRI-/-: XLF-/-:
WT MRI-/- PAXX-/- PAXX-/- PAXX-/-
Imt (d): 0 2 4 0 2 4 0 2 4 0 2 4 0 2 4
XbaI
4
3
2
1.5
1
UR, SJ+CJ
SE+CE
kb
GFP probe

Figure 20

Figure 20: MRI is not functionally redundant with ATM or PAXX in NHEJ. (A) Flow cytometric analysis of GFP expression in WT, *MRI*$^{-/-}$, and *XLF*$^{-/-}$ Abl pre-B cells that were treated with imatinib (Imt) in the absence or presence of an ATM kinase inhibitor KU55933 (ATMi) for four days. **(B)** Schematic of the *PAXX* knockout strategy using CRISPR/Cas9 with a pair of gRNAs flanking the entire *PAXX* gene. Primers used for screening are shown as blue arrows (P1 and P2). **(C)** PCR analysis of genomic DNA from *MRI*$^{-/-}$:*PAXX*$^{+/+}$ (parent line), *MRI*$^{-/-}$:*PAXX*$^{+/-}$, and *MRI*$^{-/-}$:*PAXX*$^{-/-}$ Abl pre-B cells using primers P1 and P2. **(D)** Western blot analysis of MRI and PAXX in WT, *MRI*$^{-/-}$, *PAXX*$^{-/-}$, and *MRI*$^{-/-}$:*PAXX*$^{-/-}$ Abl pre-B cells. β-actin is shown as a protein loading control. **(E)** Flow cytometric analysis of GFP expression in WT, *MRI*$^{-/-}$, *PAXX*$^{-/-}$, *MRI*$^{-/-}$:*PAXX*$^{-/-}$, and *XLF*$^{-/-}$:*PAXX*$^{-/-}$ Abl pre-B cells that were treated with imatinib (Imt) for the indicated lengths of time (days). **(F)** Southern blot analysis of genomic DNA from cells in (E) that were digested with *NheI* (top) or *XbaI* (bottom) and hybridized to the Thy1 probe. **(G)** Southern blot analysis of genomic DNA from cells in (E) that were digested with *XbaI* and hybridized to the GFP probe. Bands corresponding to different MGINV arrangements are indicated as described in Figure 1. Molecular weights (kilobases) are also shown.

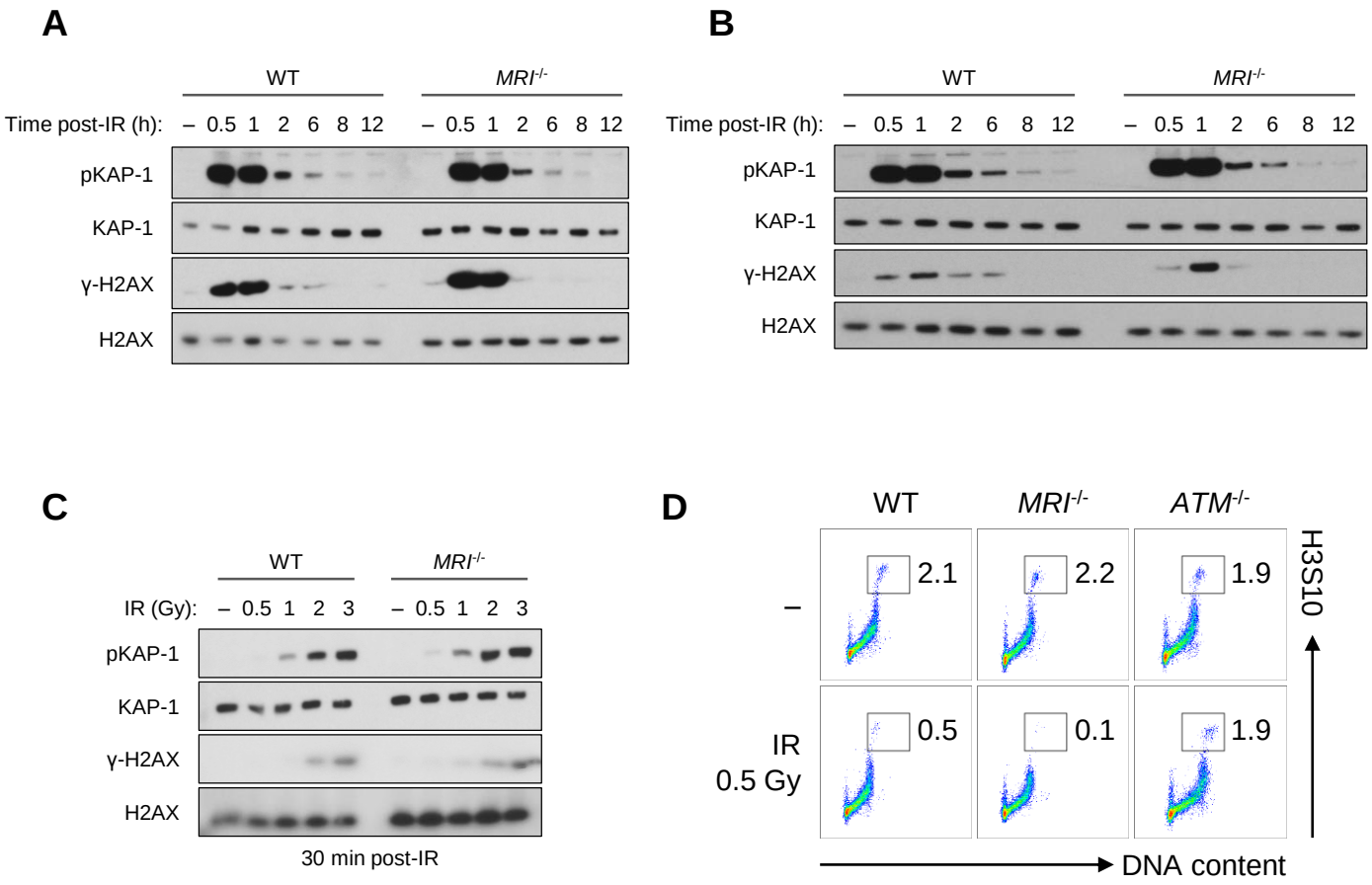
A
WT
MRI-/-
Time post-IR (h):
– 0.5 1 2 6 8 12
– 0.5 1 2 6 8 12
pKAP-1
KAP-1
γ-H2AX
H2AX
B
WT
MRI-/-
Time post-IR (h):
– 0.5 1 2 6 8 12
– 0.5 1 2 6 8 12
pKAP-1
KAP-1
γ-H2AX
H2AX
C
WT
MRI-/-
IR (Gy):
– 0.5 1 2 3
– 0.5 1 2 3
pKAP-1
KAP-1
γ-H2AX
H2AX
30 min post-IR
D
WT
MRI-/-
ATM-/-
–
IR
0.5 Gy
2.1
2.2
1.9
0.5
0.1
1.9
H3S10
DNA content

Figure 21

Figure 21: MRI deficiency does not impair DDR signaling. (A and B) Western blot analysis of DDR signaling events γ-H2AX and phospho-KAP-1 in G1-phase WT and *MRI*$^{-/-}$ Abl pre-B cells at the indicated lengths of time (hours) after exposure to 1 Gy of IR. WT and *MRI*$^{-/-}$ Abl pre-B cells generated from different mice are shown in each panel. **(C)** Western blot analysis of γ-H2AX and phospho-KAP-1 in G1-phase WT and *MRI*$^{-/-}$ Abl pre-B cells 30 minutes after exposure to the indicated doses of IR. **(D)** Flow cytometric analysis of mitotic phase (indicated by the gates) WT and *MRI*$^{-/-}$ Abl pre-B cells before and one hour after exposure to 0.5 Gy of IR.

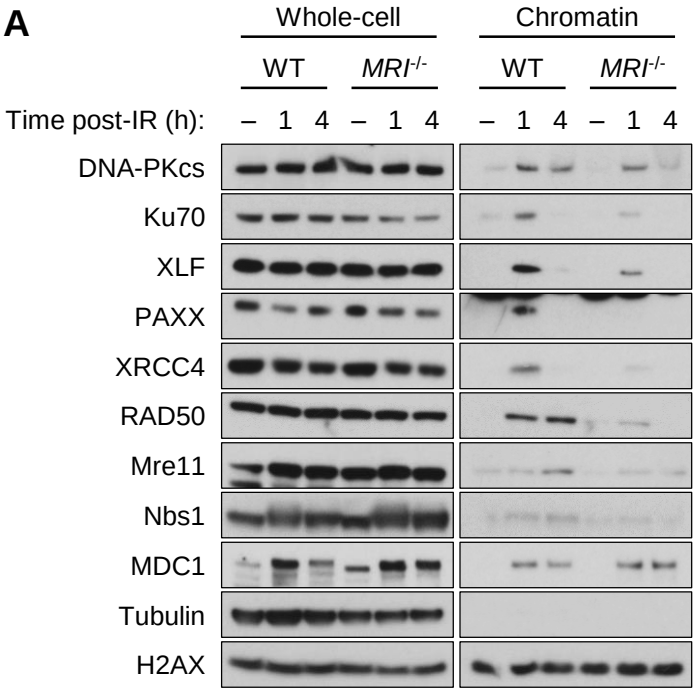
A
Whole-cell
Chromatin
WT
MRI-/-
WT
MRI-/-
Time post-IR (h):
– 1 4 – 1 4 – 1 4 – 1 4
DNA-PKcs
Ku70
XLF
PAXX
XRCC4
RAD50
Mre11
Nbs1
MDC1
Tubulin
H2AX

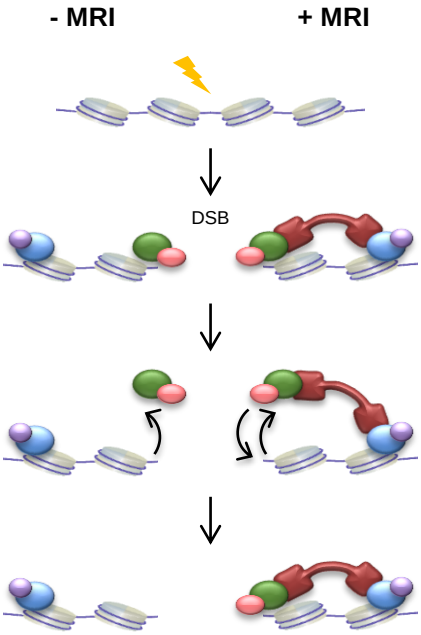
C
- MRI
+ MRI
DSB

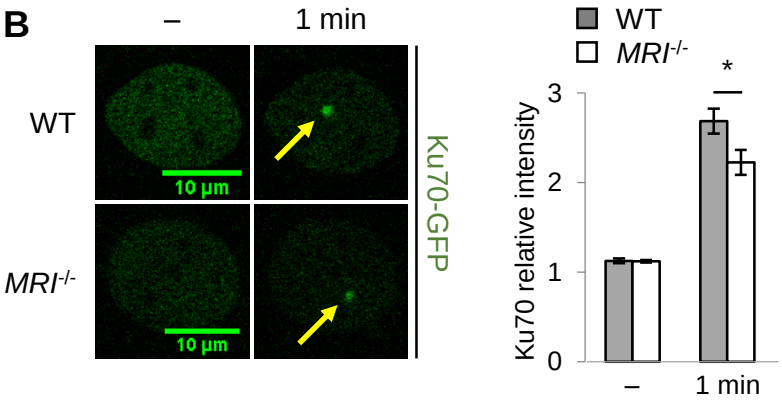
B
–
1 min
WT
MRI-/-
10 µm
10 µm
Ku70-GFP
WT
MRI-/-
*
Ku70 relative intensity
3
2
1
0
–
1 min


DDR proteins
MRI

Figure 22

Figure 22: MRI promotes the retention of DDR proteins at DSBs. (A) Western blot analysis of DDR proteins in the whole-cell extracts and chromatin fractions of G1-arrested (with imatinib) WT and *MRI*$^{-/-}$ Abl pre-B cells at the indicated times (hours) after exposure to 10 Gy of IR or no IR (–). **(B)** Representative micrographs of GFP-Ku70 recruitment to a laser-induced DNA damage site (designated by a yellow arrow) in WT and *MRI*$^{-/-}$ MEFs prior to damage (–) or 1 minute post-damage (1 min). The relative fluorescent intensities of GFP-Ku70 foci in these cells were then quantified (bottom histogram). Data are mean ± SEM. >20 cells of each genotype were analyzed in two independent experiments. * P <0.05. **(C)** Model of how MRI can increase the avidity of its associated DDR proteins for chromatin at a DSB.

Gene	MW (kDa)	# peptides (MRI)	# peptides ($MRI^{\Delta N}$)	# peptides ($MRI^{\Delta C}$)	MRI / $MRI^{\Delta N}$	MRI / $MRI^{\Delta C}$
Mthfd1l	105.66	390	615	487	0.63	0.80
Myo18a	232.61	235	298	373	0.79	0.63
Rad50	153.39	229	214	73	1.07	3.14
Atm	349.2	185	189	39	0.98	4.74
Setx	297.4	156	171	176	0.91	0.89
Xrcc6	69.44	150	51	97	2.94	1.55
Mre11a	80.17	138	123	50	1.12	2.76
Xrcc5	83	127	60	97	2.12	1.31
Prkdc	471.17	120	91	102	1.32	1.18
Mri	17.28	119	50	127	2.38	0.94
Gcn1l1	292.83	106	110	34	0.96	3.12
Dock2	211.57	99	79	74	1.25	1.34
Eef1a1	50.08	97	96	64	1.01	1.52
Chd4	217.61	93	72	86	1.29	1.08
Acta2	41.98	86	71	125	1.21	0.69
Nbn	83.74	84	79	24	1.06	3.50
Gcn1l1	115.35	77	86	29	0.90	2.66
Hspa8	70.83	76	69	72	1.10	1.06
Stk38	54.14	71	76	90	0.93	0.79
Wrn	157.1	71	97	16	0.73	4.44
Sptan1	284.42	68	66	79	1.03	0.86
Stk38l	53.74	68	76	70	0.89	0.97
Msh6	150.99	67	56	48	1.20	1.40
Rfc1	125.91	64	16	46	4.00	1.39
Flii	144.71	61	46	68	1.33	0.90
Ckap5	225.49	61	57	59	1.07	1.03
Top2a	172.68	61	62	64	0.98	0.95
Sptbn1	274.05	58	65	63	0.89	0.92
Ahnak	603.87	57	50	50	1.14	1.14
Mdc1	184.56	54	67	8	0.81	6.75
Gsn	85.89	53	43	64	1.23	0.83
Morc3	106.46	51	52	56	0.98	0.91
Prmt5	72.63	51	57	58	0.89	0.88
Msh2	104.09	47	29	28	1.62	1.68
Chd8	290.67	47	38	39	1.24	1.21
Abl1	122.6	44	31	29	1.42	1.52
Lrrfip1	79.2	44	42	52	1.05	0.85
Hnrnpm	77.6	42	24	36	1.75	1.17
Tuba1a	50.1	42	37	29	1.14	1.45
Arhgef2	111.9	41	34	28	1.21	1.46
Actb	41.71	41	41	87	1.00	0.47

Cep170	174.94	40	21	18	1.90	2.22
Gvin1	280.64	39	32	32	1.22	1.22
Smchd1	225.51	39	34	28	1.15	1.39
Ercc6l2	173.76	39	36	33	1.08	1.18
Tmod3	39.48	38	40	45	0.95	0.84
Prpf8	273.44	37	20	24	1.85	1.54
Trrap	291.37	37	24	18	1.54	2.06
Fermt3	75.59	37	31	26	1.19	1.42
Gtf3c1	237.33	37	33	24	1.12	1.54
Iqgap1	188.62	36	30	25	1.20	1.44
Rif1	266.06	34	25	19	1.36	1.79
Arhgef1	102.74	34	29	24	1.17	1.42
Hcfc1	210.31	34	30	27	1.13	1.26
Synj1	172.51	34	33	34	1.03	1.00
Otud4	122.98	34	37	49	0.92	0.69
Hspa5	72.38	34	41	37	0.83	0.92
Trim28	88.79	33	26	27	1.27	1.22
Smarcc1	122.81	33	29	35	1.14	0.94
Smc4	146.8	33	32	16	1.03	2.06
Smc3	141.47	32	26	17	1.23	1.88
Mdn1	629.94	31	28	16	1.11	1.94
Sf3b3	135.46	31	29	28	1.07	1.11
Hnrnpk	50.94	31	32	35	0.97	0.89
Jak1	133.28	31	35	32	0.89	0.97
Rpa1	68.99	30	23	18	1.30	1.67
Smc2	134.16	30	29	18	1.03	1.67
Hspa9	73.42	30	44	34	0.68	0.88
Sin3a	145	29	14	22	2.07	1.32
Smc1a	143.15	29	22	21	1.32	1.38
Sf3b1	145.72	29	28	31	1.04	0.94
Myh9	226.23	29	37	47	0.78	0.62
Ncor1	270.48	28	17	19	1.65	1.47
Wdfy4	337.15	28	21	22	1.33	1.27
Snrnp200	244.39	28	25	24	1.12	1.17
Eif4b	68.8	28	32	32	0.88	0.88
Dock11	237.62	28	33	29	0.85	0.97
Rfc5	38.07	27	9	19	3.00	1.42
Parp1	113.03	27	10	12	2.70	2.25
Smarca4	181.31	27	19	26	1.42	1.04
Wdr77	36.92	27	20	23	1.35	1.17
Gapdh	35.79	27	23	19	1.17	1.42
Hnrnpu	87.86	27	25	25	1.08	1.08

Tab1	54.58	27	28	33	0.96	0.82
Rfc2	38.7	26	11	19	2.36	1.37
Matr3	94.57	26	19	22	1.37	1.18
Dhx9	149.38	26	23	31	1.13	0.84
Prpf31	55.4	26	37	31	0.70	0.84
Wiz	184.18	25	15	15	1.67	1.67
Clasp2	140.65	25	18	13	1.39	1.92
Pds5a	150.23	25	18	15	1.39	1.67
Ep400	336.97	25	22	16	1.14	1.56
Tubb2a	49.87	25	24	28	1.04	0.89
Flna	281.05	25	30	42	0.83	0.60
Ehmt2	137.95	24	11	20	2.18	1.20
Arid1a	241.94	24	15	18	1.60	1.33
Dock8	238.83	24	17	20	1.41	1.20
Pfkp	85.4	24	20	14	1.20	1.71
Tmpo	75.12	24	21	15	1.14	1.60
Pfkfb3	58.93	24	25	29	0.96	0.83

Table 1: List of the 100-most abundant MRI-interacting proteins. The gene symbol, molecular weight (MW), total number of peptides associated with MRI, $MRI^{\Delta N}$, and $MRI^{\Delta C}$ (# peptides), and ratio of total number of peptides associated with MRI versus with $MRI^{\Delta N}$ (MRI / $MRI^{\Delta N}$) or $MRI^{\Delta C}$ (MRI / $MRI^{\Delta C}$) for each protein is shown.

Chapter 5: Discussion

5.1 Summary

Despite its implicated role in aligning broken DNA ends for ligation during NHEJ, XLF is dispensable for V(D)J end joining in developing mouse lymphocytes – a process that is strictly dependent on NHEJ (Li G et al. 2008). Rather, XLF functions redundantly in NHEJ with several other DDR factors – such as ATM, H2AX, 53BP1, DNA-PKcs, and RAG – that were previously thought to be involved in the repair of only a limited subset of DSBs (Zha S et al. 2011, Liu X et al. 2012, Oksenych V et al. 2012, Oksenych V et al. 2013). The discovery that the combined loss of XLF with any one of these proteins leads to a broadly severe defect in NHEJ strongly implies that they carry out general, not DSB-specific, activities that could cross-complement each other. Unlike the core NHEJ factors Ku70/80, Lig4, and XRCC4, these "non-core" components are not directly responsible for executing an essential step in NHEJ, such as DSB sensing (Ku70/80) or DNA end ligation (Lig4/XRCC4); instead, they likely perform ancillary functions that ultimately serve to increase the efficiency or fidelity of the reaction. We hypothesized that there exist other such non-core NHEJ factors which are likewise concealed behind these functional redundancies and that XLF deficiency creates a suboptimal NHEJ setting in which they become necessary for maintaining the integrity of the process. To explore this premise, we performed a CRISPR/Cas9-based genetic screen to identify novel non-core NHEJ factors in XLF-deficient pre-B cells, using V(D)J end joining as a measure of NHEJ.

Our screen yielded not only hits with well-established roles in V(D)J recombination, such as RAG, Ku70/80, Lig4, XRCC4, and Artemis, from WT and *XLF*$^{-/-}$ Abl pre-B cells, but also two unique candidates, PAXX and MRI, from *XLF*$^{-/-}$ Abl pre-B cells alone. Interestingly, both PAXX

and MRI share several key characteristics with XLF: all three proteins interact with Ku70/80 and contain a similar structural motif at their C-termini known as the XLM (Grundy GJ et al. 2016). In fact, PAXX has recently been demonstrated by crystallography to bear a tertiary conformation closely resembling that of XLF (Ochi T et al. 2015). We subsequently verified that while PAXX and MRI are expendable for V(D)J end joining in WT lymphocytes, loss of either protein almost completely abrogates NHEJ in XLF-deficient lymphocytes such that these cells are only capable of producing rare, mostly imprecise joins. Indeed, in contrast to *MRI*$^{-/-}$ mice, which do not exhibit any significant defects in lymphocyte development, *XLF*$^{-/-}$:*MRI*$^{-/-}$ mice invariably die in utero due to extensive neuronal apoptosis – a classic presentation of NHEJ deficiency. Because PAXX had already been described in detail by others to promote NHEJ by serving as a scaffold for Ku70/80 at DNA ends, we felt confident in the specificity of our screen and focused instead on elucidating the potential role of MRI – a peptide of unknown function at the time – in DSB repair (Ochi T et al. 2015, Liu X et al. 2017).

Consistent with the idea of it being a non-core NHEJ factor, MRI rapidly colocalizes with Ku70/80 to sites of laser-induced DNA damage and is involved in the repair of IR-induced DSBs in MEFs as well as AID-induced DSBs in mature B cells undergoing CSR. We found that MRI is intrinsically disordered and possesses highly conserved terminal motifs – attributes suggestive of an adaptor. Following this lead, we then determined by IP-MS that MRI associates with a diverse group of DDR proteins at each of its termini, including the NHEJ components Ku70/80, XRCC4, XLF, PAXX, and DNA-PKcs at the N-terminal KBM and the DDR signaling kinase ATM along with its DSB sensor MRN at the C-terminal XLM. Remarkably, MRI appears to nucleate higher order complexes containing many of these proteins at one or both of its termini simultaneously in vivo. Unlike XLF, MRI is not functionally redundant with ATM or PAXX, implying that it may

operate distinctly from XLF. Although MRI interacts with both ATM and DNA-PKcs, canonical DDR signaling events, such as γ-H2AX, phospho-KAP-1 serine 824, and activation of the G2/M checkpoint, are unperturbed in the absence of MRI, indicating that these associations serve some other purpose than the amplification or transduction of DDR signaling. It is admittedly possible that MRI can facilitate the ATM- or DNA-PKcs-dependent phosphorylation of an undetermined substrate, but due to the lack of available antibodies, the most comprehensive way to address this scenario would be to carry out stable isotope labeling with amino acids in cell culture (SILAC). However, chromatin fractionation experiments revealed that, in line with its putative role as an adaptor, MRI functions to retain its associated DDR factors at DSBs, presumably by "anchoring" proteins at one terminus to DNA through DNA:protein interactions established at the same (*cis*) or opposite (*trans*) terminus. In this regard, MRI binds to Ku70/80 and MRN at separate termini, and these DSB sensors, both of which exhibit nanomolar dissociation constants in complex with DNA (K_D for Ku70/80 ~0.5 nM and for MRN ~1.5 nM), can tether all the other DDR proteins to chromatin via their common link to MRI (Cannon B et al. 2013, Chang HHY et al. 2017). Thus, MRI behaves in a mechanistically similar manner to an antibody, which has at least two epitope-binding sites that increase its avidity for an antigen; analogously, the two DNA-binding (through Ku70/80 and MRN) termini of MRI serve to cooperatively augment the avidity of the multimeric MRI protein complex for chromatin.

How would such a function promote NHEJ? First, by maintaining a high concentration of NHEJ factors at DSBs, MRI could prevent nucleases, polymerases, and HR or AEJ proteins from accessing the DNA ends, thereby sustaining the processivity of NHEJ. This could be mediated in part by Ku70/80, which has been shown to block DNA end resection by physically occluding the DNA strand from various nucleases (Clerici M et al. 2008, Shao Z et al. 2008, Reginato G et al.

2017). Second, as MRI can form dimers and multimers in solution, two or more MRI molecules could conceivably bind to each other and couple large multiprotein complexes together across a DSB, effectively stabilizing the DNA ends in a manner reminiscent of XLF/XRCC4. This might logically explain why XLF and MRI are functionally redundant: although they work differently from one another, XLF and MRI may alternatively achieve the same overarching utility of DSB synapsis (more discussed later). Third, as we cannot rule out this possibility, MRI could mediate the phosphorylation of an ATM or DNA-PKcs substrate that is functionally redundant with XLF by bringing it into close proximity with the kinases. This substrate may be either ATM or DNA-PKcs, as there is substantial cross-phosphorylation between them (the physiological relevance of which remains unclear but appears to be inhibitory in nature), or a downstream target other than H2AX and KAP-1 (Chen BP et al. 2007, Neal JA et al. 2011, Zhou Y et al. 2017). In this regard, while ATM and DNA-PKcs also reportedly help to align DNA ends, inhibition of their catalytic activities by pharmacological agents is sufficient to obstruct V(D)J end joining in XLF-deficient lymphocytes, suggesting that these kinases do not physically mediate this function by themselves but rather through one of their substrates (Zha S et al. 2011, Oksenych V et al. 2013). A diagram depicting each of these scenarios, which are not mutually exclusive, is shown in Figure 23.

5.2 Antagonistic Roles for MRI?

Contrary to our main finding that MRI promotes NHEJ in G1-phase mouse lymphocytes, primarily evidenced by its functional redundancy with XLF in V(D)J end joining, a recent study instead concluded that MRI inhibits NHEJ in human fibrosarcoma cells during the S/G2 phases: specifically, the authors showed that MRI prevents the NHEJ-dependent fusions of shelterin-free telomeres (now recognized as DSBs by DDR proteins) at the ends of chromatids, which are only

present during S/G2, but not chromosomes, which predominantly exist during G1 (Arnoult N et al. 2017). Moreover, they found that the interaction between MRI and Ku70/80 increases during S/G2 and proposed a model in which MRI competitively sequesters Ku70/80 away from DSBs to drive repair pathway choice towards HR; by sequencing across Cas9-induced DSBs with varying overhang lengths, the authors determined that asymmetric DSBs, especially ones possessing long 3' overhangs, are repaired with larger deletions, whereas blunt DNA ends are ligated without any apparent defects, in MRI-deficient cells, suggesting that MRI also blocks the resection of single-stranded DNA ends to maintain DNA terminal structures which are more favorably processed by HR (Arnoult N et al. 2017).

This discrepancy can be reconciled by several explanations. First, MRI may differentially regulate NHEJ at blunt-ended RAG DSBs versus uncapped telomeres comprising long, repetitive 3' overhangs, as Arnoult et al. had alluded to in their study. In fact, Ku70/80 and DNA-PKcs had been shown to bind to telomeric ends, where they inhibit inappropriate telomere degradation and interchromosomal recombination (Hsu HL et al. 2000, Samper E et al. 2000, d'Adda di Fagagna F et al. 2001, Gilley D et al. 2001, Goytisolo FA et al. 2001). While the exact mechanism is still unknown, binding of Ku70/80 to the shelterin component TRF2 appears to suppress its ability to join DNA ends but not its role in protecting them from nucleolytic processing (Ribes-Zamora A et al. 2014). Like Ku70/80 and DNA-PKcs, MRI might function differently in the unique DNA-protein local environment at telomeric T-loop ends (where the 3' telomeric overhangs loop back and invade the upstream duplex DNA) than at other DSBs. Second, MRI may carry out separate activities depending on cellular context in a similar vein as XLF, which is paradoxically required for V(D)J end joining in non-lymphoid cells, such as MEFs and ES cells, but not in lymphocytes (Zha S et al. 2007, Li G et al. 2008). These disparities likely reflect differences in the chromatin

landscape (which can affect DSB accessibility) or protein content of lymphoid and non-lymphoid cells. Indeed, many DDR factors seem to display distinct tissue-tropic roles: notably, inactivating mutations in the *BRCA1* and *BRCA2* genes preferentially increase the risks for breast and ovarian cancers, while ATM deficiency primarily predisposes to lymphomas, even though these proteins are ubiquitously expressed (Roy R et al. 2012, Choi M et al. 2016). We had previously observed that there is significant variance in the expression of DDR proteins, such as Ku70/80, ATM, and MRN, between fibroblasts and myeloid cells which ultimately resulted in divergent responses to DNA damage (Morales AJ et al. 2017). Thus, it is conceivable that MRI function can be altered by different protein stoichiometries and interactions in different cell types. In this regard, we did not detect any changes in the levels of MRI-Ku70/80 association by IP between cycling and G1-arrested WT Abl pre-B cells, contrary to what Arnoult et al. had reported in HT1080 6TG human fibrosarcoma cell-lines (data not shown). Third, the antagonistic activities of MRI may be strictly segregated by the G1-to-S phase transition. Since MRI expression remains consistent throughout the cell cycle and is active both G1 and S/G2, the most plausible scenario is that MRI undergoes some form of post-translational modification which reverses its mechanism. HR factors, such as MRN and CtIP, are likewise phosphorylated by cyclin-dependent kinases (CDKs) during G2/S to mediate DNA end resection (Huertas P et al. 2008, Falck J et al. 2012). One of our collaborators, Dr. John Tainer at MD Anderson Cancer Center, has identified a potential phosphorylation site at serine 122 of MRI in mitotic cells using SILAC (personal communication). An important follow-up question is whether this phosphorylation event is functionally relevant in DSB repair, and if so, which kinase is responsible for it.

5.3 Functional Redundancies of XLF

Here, we identified two additional factors, PAXX and MRI, which are required for V(D)J end joining in XLF-deficient lymphocytes. How can the broad functional redundancies between XLF and diverse DDR proteins, including ATM, DNA-PKcs, H2AX, 53BP1, RAG, PAXX, and MRI, be explained? One possibility is that all these non-core NHEJ factors carry out overlapping activities with XLF, presumably in DSB synapsis. Indeed, ATM, DNA-PKcs, and RAG had been implicated in stabilizing DNA ends generated during V(D)J recombination (and potentially other genotoxic processes) by promoting their retention within PCCs and keeping them from diffusing irreversibly apart to establish aberrant joins elsewhere (DeFazio LG et al. 2002, Bredemeyer AL et al. 2006, Spagnolo L et al. 2006, Deriano L et al. 2011). Moreover, the combined loss of ATM and DNA-PKcs leads to a near complete block in V(D)J end joining, suggesting that XLF, ATM, and DNA-PKcs share a common mechanism in NHEJ (Gapud EJ et al. 2011, Zha S et al. 2011). However, this model fails to adequately address the functional redundancies of XLF with H2AX and 53BP1, both of which are not involved in aligning broken DNA ends but rather in protecting them from nucleolytic degradation: in this regard, depletion of H2AX or 53BP1, but not XLF, in NHEJ-deficient Abl pre-B cells causes extensive resection of unrepaired SEs and CEs, and while *XLF*$^{-/-}$:*H2AX*$^{-/-}$ and *XLF*$^{-/-}$:*53BP1*$^{-/-}$ Abl pre-B cells also exhibit a similar phenotype, SEs and CEs remain largely intact in *XLF*$^{-/-}$:*PAXX*$^{-/-}$ and *XLF*$^{-/-}$:*MRI*$^{-/-}$ Abl pre-B cells, implying that XLF does not play a role in counteracting DNA end resection and is therefore not functionally equivalent to H2AX and 53BP1 (Helmink BA et al. 2011, Zha S et al. 2011, Oksenych V et al. 2012, Liu X et al. 2012, Kumar V et al. 2014, Kumar V et al. 2016, Lescale C et al. 2016, Hung PJ et al. 2017, Liu X et al. 2017). Furthermore, PAXX and MRI likewise do not appear to operate identically to XLF. For example, PAXX and MRI facilitate the assembly of other NHEJ factors on chromatin, whereas XLF does not support such a function (Wu PY et al. 2007, Ochi T et al. 2015). Unlike

XLF, PAXX and MRI are not functionally redundant with ATM or with one another, suggesting that they make distinct mechanistic contributions to NHEJ (Zha S et al. 2011, Liu X et al. 2017). One could still argue that these proteins are functionally equivalent, only that XLF plays a more significant role than PAXX and MRI in NHEJ; in other words, the absence of PAXX or MRI is not sufficient to impair NHEJ to the extent that ATM becomes necessary. We cannot completely refute this concept but find it unlikely due to the different protein interactions mediated by XLF, PAXX, and MRI.

A more compelling possibility is that XLF and its redundant non-core NHEJ factors carry out separate activities that may (1) cooperatively achieve the same general purpose, such as DSB synapsis or exclusion of undesirable elements and processes (e.g. components of the HR or AEJ pathway), or (2) independently augment the efficiency and/or fidelity of the reaction. In the first case, for example, the ability of PAXX and MRI to retain XLF and XRCC4 on chromatin could promote the polymerization of XLF/XRCC4 filaments along DNA ends and in effect strengthen the DSB synaptic complex. In the second case, the speed of DNA end joining could be enhanced by XLF/XRCC4 providing proper structural alignment and by PAXX and MRI fostering a higher concentration of Lig4 near DSBs simultaneously. Indeed, we observed that V(D)J end joining is drastically impaired but not abolished in $XLF^{-/-}$:$PAXX^{-/-}$ and $XLF^{-/-}$:$MRI^{-/-}$ Abl pre-B cells, which can still form low frequencies of imprecise SJs, suggesting that the kinetics of NHEJ is slowed in these cells. Thus, instead of performing an essential step in NHEJ, these non-core factors seem to collectively sponsor an optimal local environment for NHEJ – such a "microenvironment" could be particularly beneficial during the repair of complex or inaccessible DSBs, where Ku70/80 and Lig4/XRCC4 would conceivably require assistance in dealing with suboptimal substrates. In the end, all the aforementioned scenarios are not mutually exclusive and may apply to different XLF

functional redundancies. An important question to investigate moving forward is why dissimilar DDR proteins are functionally redundant with XLF but not necessarily with each other. This will entail clarifying the mechanistic role of XLF in vivo – a pursuit that has now eluded the field for over a decade.

5.4 Future Directions

There are two major directions from our study of MRI that we are interested in exploring. First, we had focused only on protein interactions mediated by the conserved N- and C-termini of MRI and would like to follow up on those potentially mediated by a conserved central region (aa 57-72). In this regard, our IP-MS data had revealed several MRI-interacting proteins which were not affected by either the N- or C-terminal truncation, suggesting that they might associate with MRI through its central region. Intriguingly, among these proteins are the DNA mismatch repair (MMR) factors MSH2 and MSH6, which together form a heterodimer MutSα that detects single-nucleotide and short-sequence mismatches in the genome; despite their well-established roles in MMR, MSH2 and MSH6 had been found to participate in multimeric complexes with numerous DDR proteins, such as ATM, MRN, and BRCA1, and had even been implicated in the regulation of HR in mammalian cells (de Wind N et al. 1995, Wang Y et al. 2001, Smith JA et al. 2007). It is also plausible that MMR could promote the ligation of incompatible DNA ends during NHEJ by correcting nucleotide mismatches between a pair of overhangs – an idea we are eager to test. We had already validated the interaction between MRI and MSH2/6 by IP and currently plan to examine whether this association is indeed dependent on the central region of MRI by attempting to pull down MSH2/6 with a MRI mutant lacking the central region (data not shown). Moreover, we can assess the functionality of the central region by trying to use this mutant to rescue V(D)J

end joining in *XLF*$^{-/-}$:*MRI*$^{-/-}$ Abl pre-B cells: failure to reverse the defect would strongly indicate a role for the central region and its interacting proteins in NHEJ. Ultimately, this approach might prove to be useful in discovering new NHEJ protein functions and avenues of crosstalk between separate DNA repair pathways, thus giving us a more complete understanding of the mechanisms underlying the DDR.

Second, we would like to characterize in further detail the post-translational regulation of MRI. Since most intrinsically disordered peptides tend to adopt a more stable conformation once bound to their ligands, we surmised that MRI, when complexed to its interacting proteins, might likewise assume a functional structure which would be informative of its mechanistic purpose in NHEJ. As a pilot study, we are currently collaborating with Dr. John Tainer's lab to look at how MRI may be allosterically modulated through its association with Ku70/80 using small-angle X-ray scattering (SAXS). Admittedly, our results had only demonstrated that Ku70/80 is necessary for the binding of XLF, PAXX, XRCC4, and DNA-PKcs to MRI – not that these proteins bind to MRI via Ku70/80 – so it is equally possible that Ku70/80 binding to MRI induces a secondary or tertiary structure that is amenable to interacting with the NHEJ machinery. Consistent with such a notion, our CD data showed that MRI can form helical structures in solution when treated with a crowding agent. Finally, we also plan to investigate the putative phosphorylation site in MRI at serine 122. Other than validating its functional relevance and identifying the upstream kinase as aforementioned, we are interested in clarifying the conditions that stimulate this phosphorylation event (perhaps DNA damage or cell cycle phase transition?) and how it modifies the activity and protein interactions of MRI. An outstanding question in the field is how NHEJ factors dissociate from chromatin after repair is completed, given their high affinities for DNA, and it is somewhat tempting to speculate that post-translational signals leading to MRI degradation or removal from

chromatin would concurrently promote the disengagement of its associated DDR proteins. Thus, elucidating these details will hopefully not only help us reconcile the discrepant roles of MRI in G1 versus S/G2, but also provide us with deeper insights on how NHEJ is regulated, how it may be corrupted during oncogenesis, and how it can be manipulated for cancer therapeutics and even genome editing technologies.

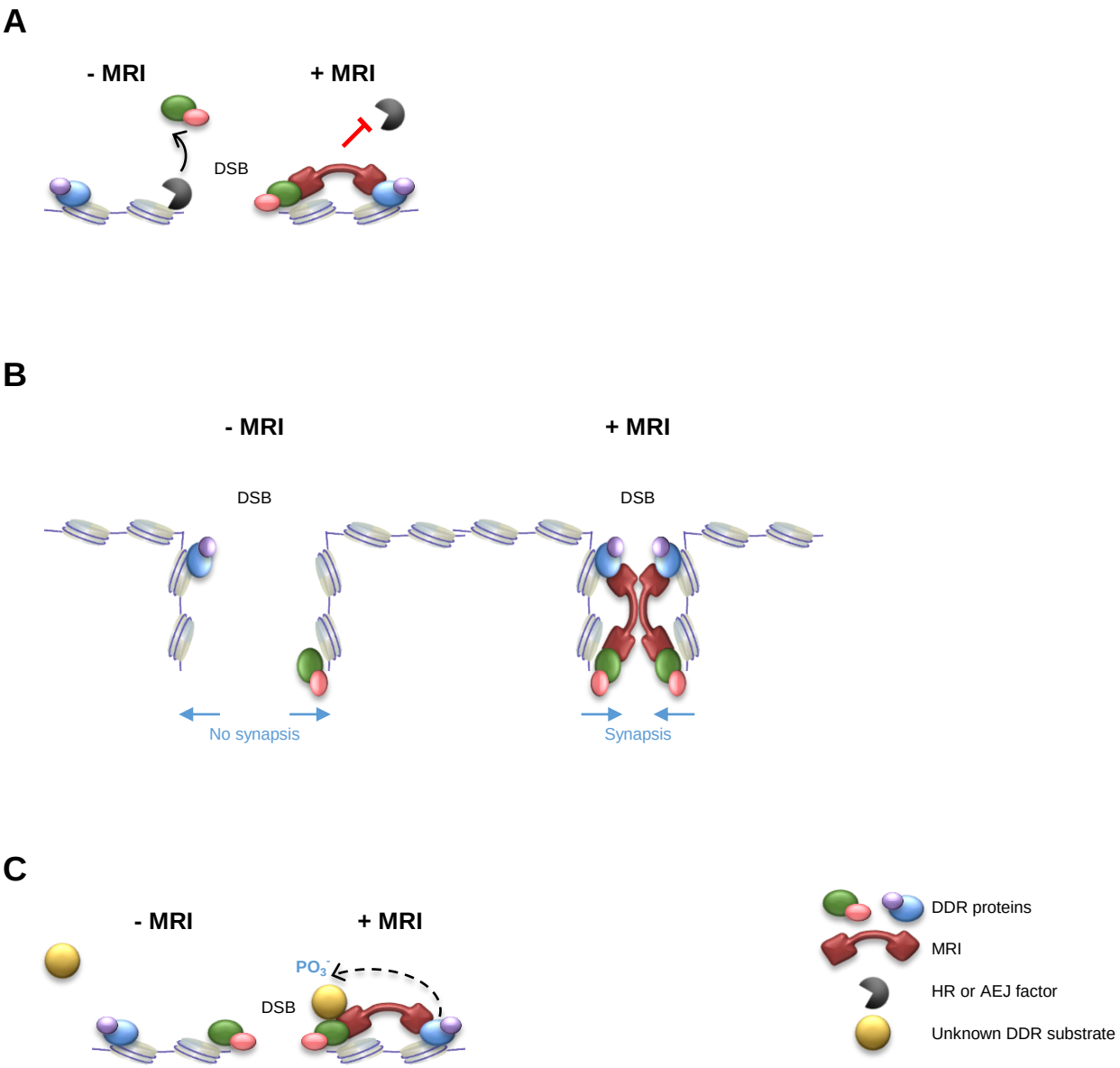
A
- MRI
+ MRI
DSB
B
- MRI
+ MRI
DSB
DSB
No synapsis
Synapsis
C
- MRI
+ MRI
PO3
DSB
DDR proteins
MRI
HR or AEJ factor
Unknown DDR substrate

Figure 23

Figure 23: Models of MRI function in NHEJ. (A) By concentrating other NHEJ factors near a DSB, MRI can prevent components of the HR or AEJ pathway from accessing the exposed DNA ends. **(B)** Two MRI molecules bound to opposing DNA ends via Ku70/80 or MRN can dimerize and mediate DSB synapsis, maintaining the DNA ends in close proximity for ligation. **(C)** MRI can link ATM or DNA-PKcs to a substrate that is functionally redundant with XLF, thus leading to its phosphorylation and activation.

Literature Cited

Abramowski V, Etienne O, Elsaid R, Yang J, Berland A, Kermasson L, Roch B, Musilli S, Moussu JP, Lipson-Ruffert K, Revy P, Cumano A, Boussin FD, de Villartay JP. "PAXX and Xlf interplay revealed by impaired CNS development and immunodeficiency of double KO mice." Cell Death Differ. **2018**;25(2):444-452.

Ahnesorg P, Smith P, Jackson SP. "XLF interacts with the XRCC4-DNA ligase IV complex to promote DNA nonhomologous end-joining." Cell. **2006**;124(2):301-13.

Akopiants K, Zhou RZ, Mohapatra S, Valerie K, Lees-Miller SP, Lee KJ, Chen DJ, Revy P, de Villartay JP, Povirk LF. "Requirement for XLF/Cernunnos in alignment-based gap filling by DNA polymerases lambda and mu for nonhomologous end joining in human whole-cell extracts." Nucleic Acids Res. **2009**;37(12):4055-62.

Almohaini M, Chalasani SL, Bafail D, Akopiants K, Zhou T, Yannone SM, Ramsden DA, Hartman MCT, Povirk LF. "Nonhomologous end joining of complex DNA double-strand breaks with proximal thymine glycol and interplay with base excision repair." DNA Repair. **2016**;41:16-26.

Andres SN, Modesti M, Tsai CJ, Chu G, Junop MS. "Crystal structure of human XLF: a twist in nonhomologous DNA end-joining." Mol Cell. **2007**;28(6):1093-101.

Andres SN, Vergnes A, Ristic D, Wyman C, Modesti M, Junop M. "A human XRCC4-XLF complex bridges DNA." Nucleic Acids Res. **2012**;40(4):1868-78.

Agarwal S, Harada J, Schreifels J, Lech P, Nikolai B, Yamaguchi T, Chanda SK, Somia NV. "Isolation, characterization, and genetic complementation of a cellular mutant resistant to retroviral infection." Proc Natl Acad Sci U S A. **2006**;103(43):15933-8.

Agrawal A, Schatz DG. "RAG1 and RAG2 form a stable postcleavage synaptic complex with DNA containing signal ends in V(D)J recombination." Cell. **1997**;89(1):43-53.

Arnoult N, Correia A, Ma J, Merlo A, Garcia-Gomez S, Maric M, Tognetti M, Benner CW, Boulton SJ, Saghatelian A, Karlseder J. "Regulation of DNA repair pathway choice in S and G2 phases by the NHEJ inhibitor CYREN." Nature. **2017**;549(7673):548-552.

Balmus G, Barros AC, Wijnhoven PW, Lescale C, Hasse HL, Boroviak K, le Sage C, Doe B, Speak AO, Galli A, Jacobsen M, Deriano L, Adams DJ, Blackford AN, Jackson SP. "Synthetic lethality between PAXX and XLF in mammalian development." Genes Dev. **2016**;30(19):2152-2157.

Barlow JH, Faryabi RB, Callén E, Wong N, Malhowski A, Chen HT, Gutierrez-Cruz G, Sun HW, McKinnon P, Wright G, Casellas R, Robbiani DF, Staudt L, Fernandez-Capetillo O, Nussenzweig

A. “Identification of early replicating fragile sites that contribute to genome instability.” Cell. **2013**;152(3):620-32.

Bassing CH, Suh H, Ferguson DO, Chua KF, Manis J, Eckersdorff M, Gleason M, Bronson R, Lee C, Alt FW. “Histone H2AX: a dosage-dependent suppressor of oncogenic translocations and tumors.” Cell. **2003**;114(3):359-70.

Biehs R, Steinlage M, Barton O, Juhász S, Künzel J, Spies J, Shibata A, Jeggo PA, Löbrich M. “DNA double-strand break resection occurs during non-homologous end joining in G1 but is distinct from resection during homologous recombination.” Mol Cell. **2017**;65(4):671-684.e5.

Bohgaki M, Bohgaki T, El Ghamrasni S, Srikumar T, Maire G, Panier S, Fradet-Turcotte A, Stewart GS, Raught B, Hakem A, Hakem R. “RNF168 ubiquitylates 53BP1 and controls its response to DNA double-strand breaks.” Proc Natl Acad Sci U S A. **2013**;110(52):20982-7

Boulton SJ, Jackson SP. “Saccharomyces cerevisiae Ku70 potentiates illegitimate DNA double-strand break repair and serves as a barrier to error-prone DNA repair pathways.” EMBO J. **1996**;15(18):5093-103.

Buck D, Malivert L, de Chasseval R, Barraud A, Fondanèche MC, Sanal O, Plebani A, Stéphan JL, Hufnagel M, le Deist F, Fischer A, Durandy A, de Villartay JP, Revy P. “Cernunnos, a novel nonhomologous end-joining factor, is mutated in human immunodeficiency with microcephaly.” Cell. **2006**;124(2):287-99.

Bredemeyer AL, Sharma GG, Huang CY, Helmink BA, Walker LM, Khor KC, Nuskey B, Sullivan KE, Pandita TK, Bassing CH, Sleckman BP. “ATM stabilizes DNA double-strand-break complexes during V(D)J recombination.” Nature. **2006**;442(7101):466-70.

Brouwer I, Sitters G, Candelli A, Heerema SJ, Heller I, de Melo AJ, Zhang H, Normanno D, Modesti M, Peterman EJ, Wuite GJ. “Sliding sleeves of XRCC4-XLF bridge DNA and connect fragments of broken DNA.” Nature. **2016**;535(7613):566-9.

Callén E, Jankovic M, Wong N, Zha S, Chen HT, Difilippantonio S, Di Virgilio M, Heidkamp G, Alt FW, Nussenzweig A, Nussenzweig M. “Essential role for DNA-PKcs in DNA double-strand break repair and apoptosis in ATM-deficient lymphocytes.” Mol Cell. **2009**;34(3):285-97.

Cannon B, Kuhnlein J, Yang SH, Cheng A, Schindler D, Stark JM, Russell R, Paull TT. “Visualization of local DNA unwinding by Mre11/Rad50/Nbs1 using single-molecule FRET.” Proc Natl Acad Sci U S A. **2013**;110(47):18868-73.

Ceccaldi R, Rondinelli B, D'Andrea AD. “Repair pathway choices and consequences at the double-strand break.” Trends Cell Biol. **2016**;26(1):52-64.

Celeste A, Difilippantonio S, Difilippantonio MJ, Fernandez-Capetillo O, Pilch DR, Sedelnikova OA, Eckhaus M, Ried T, Bonner WM, Nussenzweig A. “H2AX haploinsufficiency modifies genomic stability and tumor susceptibility.” Cell. **2003**;114(3):371-383.

Celeste A, Petersen S, Romanienko PJ, Fernandez-Capetillo O, Chen HT, Sedelnikova OA, Reina-San-Martin B, Coppola V, Meffre E, Difilippantonio MJ, Redon C, Pilch DR, Olaru A, Eckhaus M, Camerini-Otero RD, Tessarollo L, Livak F, Manova K, Bonner WM, Nussenzweig MC, Nussenzweig A. "Genomic instability in mice lacking histone H2AX." Science. **2002**;296:922–7.

Chang HH, Watanabe G1, Lieber MR. "Unifying the DNA end-processing roles of the artemis nuclease: Ku-dependent Artemis resection at blunt DNA ends." J Biol Chem. **2015**;290(40):24036-50.

Chang HHY, Pannunzio NR, Adachi N, Lieber MR. "Non-homologous DNA end joining and alternative pathways to double-strand break repair." Nat Rev Mol Cell Biol. **2017**;18(8):495-506.

Chaudhuri J, Basu U, Zarrin A, Yan C, Franco S, Perlot T, Vuong B, Wang J, Phan RT, Datta A, Manis J, Alt FW. "Evolution of the immunoglobulin heavy chain class switch recombination mechanism." Adv Immunol. **2007**;94:157-214.

Chen BP, Uematsu N, Kobayashi J, Lerenthal Y, Krempler A, Yajima H, Löbrich M, Shiloh Y, Chen DJ. "Ataxia telangiectasia mutated (ATM) is essential for DNA-PKcs phosphorylations at the Thr-2609 cluster upon DNA double strand break." J Biol Chem. **2007**;282(9):6582-7.

Chiruvella KK, Liang Z, Wilson TE. "Repair of double-strand breaks by end joining." Cold Spring Harb. Perspect. Biol. **2013**;5: a012757.

Choi M, Kipps T, Kurzrock R. "ATM mutations in cancer: therapeutic implications." Mol Cancer Ther. **2016**;15(8):1781-91.

Clerici M, Mantiero D, Guerini I, Lucchini G, Longhese MP. "The Yku70-Yku80 complex contributes to regulate double-strand break processing and checkpoint activation during the cell cycle." EMBO Rep. **2008**;9(8):810-8.

Corneo B, Wendland RL, Deriano L, Cui X, Klein IA, Wong SY, Arnal S, Holub AJ, Weller GR, Pancake BA, Shah S, Brandt VL, Meek K, Roth DB. "Rag mutations reveal robust alternative end joining." Nature. **2007**;449(7161):483-6.

Costantini S, Woodbine L, Andreoli L, Jeggo PA, Vindigni A. "Interaction of the Ku heterodimer with the DNA ligase IV/Xrcc4 complex and its regulation by DNA-PK." DNA Repair. **2007**;6(6):712-22.

Coussens MA, Wendland RL, Deriano L, Lindsay CR, Arnal SM, Roth DB. "RAG2's acidic hinge restricts repair-pathway choice and promotes genomic stability." Cell Rep. **2013**;4(5):870-8.

Craxton A, Somers J, Munnur D, Jukes-Jones R, Cain K, Malewicz M. "XLS (c9orf142) is a new component of mammalian DNA double-stranded break repair." Cell Death Differ. **2015**;22(6):890-7.

Curry JD, Schlissel MS. “RAG2's non-core domain contributes to the ordered regulation of V(D)J recombination.” Nucleic Acids Res. **2008**;36(18):5750-62.

d'Adda di Fagagna F, Hande MP, Tong WM, Roth D, Lansdorp PM, Wang ZQ, Jackson SP. “Effects of DNA nonhomologous end-joining factors on telomere length and chromosomal stability in mammalian cells.” Curr Biol. **2001**;11(15):1192-6.

DeFazio LG, Stansel RM, Griffith JD, Chu G. “Synapsis of DNA ends by DNA-dependent protein kinase.” EMBO J. **2002**;21:3192–3200.

Deriano L, Chaumeil J, Coussens M, Multani A, Chou Y, Alekseyenko AV, Chang S, Skok JA, Roth DB. “The RAG2 C terminus suppresses genomic instability and lymphomagenesis.” Nature. **2011**;471(7336):119-23.

Difilippantonio MJ, Zhu J, Chen HT, Meffre E, Nussenzweig MC, Max EE, Ried T, Nussenzweig A. “DNA repair protein Ku80 suppresses chromosomal aberrations and malignant transformation.” Nature. **2000**;404(6777):510-4.

Difilippantonio S, Gapud E, Wong N, Huang CY, Mahowald G, Chen HT, Kruhlak MJ, Callen E, Livak F, Nussenzweig MC, Sleckman BP, Nussenzweig A. “53BP1 facilitates long-range DNA end-joining during V(D)J recombination.” Nature. **2008**;456:529–33.

Dudley DD, Chaudhuri J, Bassing CH, Alt FW. “Mechanism and control of V(D)J recombination versus class switch recombination: similarities and differences.” Adv Immunol. **2005**;86:43-112.

de Wind N, Dekker M, Berns A, Radman M, te Riele H. “Inactivation of the mouse Msh2 gene results in mismatch repair deficiency, methylation tolerance, hyperrecombination, and predisposition to cancer.” Cell. **1995**;82(2):321-30.

Dynan WS, Yoo S. “Interaction of Ku protein and DNA-dependent protein kinase catalytic subunit with nucleic acids. Interaction of Ku protein and DNA-dependent protein kinase catalytic subunit with nucleic acids.” Nucleic Acids Res. **1998**;26(7):1551-9.

Eng JK, McCormack AL, Yates JR. “An approach to correlate tandem mass spectral data of peptides with amino acid sequences in a protein database.” J Am Soc Mass Spectrom. **1994**;5(11):976-89.

Falck J, Forment JV, Coates J, Mistrik M, Lukas J, Bartek J, Jackson SP. “CDK targeting of NBS1 promotes DNA-end resection, replication restart and homologous recombination.” EMBO Rep. **2012**;13(6):561-8.

Fernandez-Capetillo O, Lee A, Nussenzweig M, Nussenzweig A. “H2AX: the histone guardian of the genome.” DNA Repair. **2004**;3:959–67.

Frank KM, Sekiguchi JM, Seidl KJ, Swat W, Rathbun GA, Cheng HL, Davidson L, Kangaloo L, Alt FW. “Late embryonic lethality and impaired V(D)J recombination in mice lacking DNA ligase

IV.” Nature. **1998**;396(6707):173-7.

Frank KM, Sharpless NE, Gao Y, Sekiguchi JM, Ferguson DO, Zhu C, Manis JP, Horner J, DePinho RA, Alt FW. “DNA ligase IV deficiency in mice leads to defective neurogenesis and embryonic lethality via the p53 pathway.” Mol Cell. **2000**;5(6):993-1002.

Fugmann SD, Lee AI, Shockett PE, Villey IJ, Schatz DG. “The RAG proteins and V(D)J recombination: complexes, ends, and transposition.” Annu Rev Immunol. **2000**;18:495-527.

Gao Y, Chaudhuri J, Zhu C, Davidson L, Weaver DT, Alt FW. “A targeted DNA-PKcs-null mutation reveals DNA-PK-independent functions for KU in V(D)J recombination.” Immunity. **1998**;9(3):367-76.

Gao Y, Sun Y, Frank KM, Dikkes P, Fujiwara Y, Seidl KJ, Sekiguchi JM, Rathbun GA, Swat W, Wang J, Bronson RT, Malynn BA, Bryans M, Zhu C, Chaudhuri J, Davidson L, Ferrini R, Stamato T, Orkin SH, Greenberg ME, Alt FW. “A critical role for DNA end-joining proteins in both lymphogenesis and neurogenesis.” Cell. **1998**;95(7):891-902.

Gapud EJ, Dorsett Y, Yin B, Callen E, Bredemeyer A, Mahowald GK, Omi KQ, Walker LM, Bednarski JJ, McKinnon PJ, Bassing CH, Nussenzweig A, Sleckman BP. “Ataxia telangiectasia mutated (Atm) and DNA-PKcs kinases have overlapping activities during chromosomal signal joint formation.” Proc Natl Acad Sci U S A. **2011**;108:2022–7.

Gigi V, Lewis S, Shestova O, Mijušković M, Deriano L, Meng W, Luning Prak ET, Roth DB. “RAG2 mutants alter DSB repair pathway choice in vivo and illuminate the nature of 'alternative NHEJ'.” Nucleic Acids Res. **2014**;42(10):6352-64

Gilley D, Tanaka H, Hande MP, Kurimasa A, Li GC, Oshimura M, Chen DJ. “DNA-PKcs is critical for telomere capping.” Proc Natl Acad Sci U S A. **2001**;98(26):15084-8.

Grundy GJ, Rulten SL, Arribas-Bosacoma R, Davidson K, Kozik Z, Oliver AW, Pearl LH, Caldecott KW. “The Ku-binding motif is a conserved module for recruitment and stimulation of non-homologous end-joining proteins” Nat Commun. **2016**;7:11242.

Goodarzi AA, Kurka T, Jeggo PA. “ KAP-1 phosphorylation regulates CHD3 nucleosome remodeling during the DNA double-strand break response.” Nat. Struct. Mol. Biol. **2008**;18:831–839.

Goodarzi AA, Noon AT, Deckbar D, Ziv Y, Shiloh Y, Lobrich M, Jeggo PA. “ATM signaling facilitates repair of DNA double-strand breaks associated with heterochromatin.” Mol. Cell. **2008**;31:167–177.

Goodarzi AA, Yu Y, Riballo E, Douglas P, Walker SA, Ye R, Härer C, Marchetti C, Morrice N, Jeggo PA, Lees-Miller SP. “DNA-PK autophosphorylation facilitates Artemis endonuclease activity.” EMBO J. **2006**;25(16):3880-9.

Goytisolo FA, Samper E, Edmonson S, Taccioli GE, Blasco MA. "The absence of the dna-dependent protein kinase catalytic subunit in mice results in anaphase bridges and in increased telomeric fusions with normal telomere length and G-strand overhang." Mol Cell Biol. **2001**;21(11):3642-51.

Graham TG, Walter JC, Loparo JJ. "Two-stage synapsis of DNA ends during n-homologous end joining." Mol Cell. **2016**;61(6):850-8.

Grawunder, U., Wilm, M., Wu, X., Kulesza, P., Wilson, T.E., Mann, M., and Lieber, M.R. "Activity of DNA ligase IV stimulated by complex formation with XRCC4 protein in mammalian cells". Nature. **1997**;388(6641):492-5.

Grawunder U, Zimmer D, Lieber MR. "DNA ligase IV binds to XRCC4 via a motif located between rather than within its BRCT domains." Curr Biol. **1998**;8(15):873-6.

Gu J, Lu H, Tsai AG, Schwarz K, Lieber MR. "Single-stranded DNA ligation and XLF-stimulated incompatible DNA end ligation by the XRCC4-DNA ligase IV complex: influence of terminal DNA sequence." Nucleic Acids Res. **2007**;35(17):5755-62.

Hammel M, Rey M, Yu Y, Mani RS, Classen S, Liu M, Pique ME, Fang S, Maha ney BL, Weinfeld M, Schriemer DC, Lees-Miller SP, Tainer JA. "XRCC4 protein interactions with XRCC4-like factor (XLF) create an extended grooved scaffold for DNA ligation and double strand break repair." J Biol Chem. **2011**;286(37):32638-50.

Helmink BA, Bredemeyer AL, Lee BS, Huang CY, Sharma GG, Walker LM, Bednarski JJ, Lee WL, Pandita TK, Bassing CH, Sleckman BP. "MRN complex function in the repair of chromosomal Rag-mediated DNA double-strand breaks." J Exp Med. **2009**;206(3):669-79.

Helmink BA, Sleckman BP. "The response to and repair of RAG-mediated DNA double-strand breaks." Annu Rev Immunol. **2012**;30:175-202.

Helmink BA, Tubbs AT, Dorsett Y, Bednarski JJ, Walker LM, Feng Z, Sharma GG, McKinnon PJ, Zhang J, Bassing CH, Sleckman BP. "H2AX prevents CtIP-mediated DNA end resection and aberrant repair in G1-phase lymphocytes." Nature. **2011**;469(7329):245-9.

Hentges P, Ahnesorg P, Pitcher RS, Bruce CK, Kysela B, Green AJ, Bianchi J, Wilson TE, Jackson SP, Doherty AJ. "Evolutionary and functional conservation of the DNA non-homologous end-joining protein, XLF/Cernunnos." J Biol Chem. **2006**;281(49):37517-26.

Hiom K, Gellert M. "Assembly of a 12/23 paired signal complex: a critical control point in V(D)J recombination." Mol Cell. **1998**;1(7):1011-9.

Hsu HL, Gilley D, Galande SA, Hande MP, Allen B, Kim SH, Li GC, Campisi J, Kohwi-Shigematsu T, Chen DJ. "Ku acts in a unique way at the mammalian telomere to prevent end joining." Genes Dev. **2000**;14(22):2807-12.

Huang CY, Sharma GG, Walker LM, Bassing CH, Pandita TK, Sleckman BP. "Defects in coding joint formation in vivo in developing ATM-deficient B and T lymphocytes." J Exp Med. **2007**;204:1371–81.

Huertas P, Cortés-Ledesma F, Sartori AA, Aguilera A, Jackson SP. "CDK targets Sae2 to control DNA-end resection and homologous recombination." Nature. **2008**;455(7213):689-92.

Hung PJ, Chen BR, George R, Liberman C, Morales AJ, Colon-Ortiz P, Tyler JK, Sleckman BP, Bredemeyer AL. "Deficiency of XLF and PAXX prevents DNA double-strand break repair by non-homologous end joining in lymphocytes." Cell Cycle. **2017**;16(3):286-295.

Jiang H, Chang FC, Ross AE, Lee J, Nakayama K, Nakayama K, Desiderio S. "Ubiquitylation of RAG-2 by Skp2-SCF links destruction of te V(D)J recombinase to the cell cycle." Mol Cell. **2005**;18(6):699-709.

Jiang W, Crowe JL, Liu X, Nakajima S, Wang Y, Li C, Lee BJ, Dubois RL, Liu C, Yu X, Lan L, Zha S. "Differential phosphorylation of DNA-PKcs regulates the interplay between end-processing and end-ligation during nonhomologous end-joining." Mol Cell. **2015**;58(1):172-85.

Kabotyanski EB, Gomelsky L, Han JO, Stamato TD, Roth DB. "Double-strand break repair in Ku86- and XRCC4-deficient cells." Nucleic Acids Res. **1998**;26(23):5333-42.

Keppel TR, Howard BA, Weis DD. "Mapping unstructured regions and synergistic folding in intrinsically disordered proteins with amide H/D exchange mass spectrometry." Biochemistry. **2011**;50(40):8722-32.

Klein IA, Resch W, Jankovic M, Oliveira T, Yamane A, Nakahashi H, Di Virgilio M, Bothmer A, Nussenzweig A, Robbiani DF, Casellas R, Nussenzweig MC. "Translocation-capture sequencing reveals the extent and nature of chromosomal rearrangements in B lymphocytes." Cell. **2011**;147(1):95-106.

Koike-Yusa H, Li Y, Tan EP, Velasco-Herrera Mdel C, Yusa K. "Genome-wide recessive genetic screening in mammalian cells with a lentiviral CRISPR-guide RNA library." Nat Biotechnol. **2014**;32(3):267-73.

Kurosawa A, Koyama H, Takayama S, Miki K, Ayusawa D, Fujii M, Iiizumi S, Adachi N. "The requirement of Artemis in double-strand break repair depends on the type of DNA damage." DNA Cell Biol. **2008**;27(1):55-61.

Kumar V, Alt FW, Frock RL. "PAXX and XLF DNA repair factors are functionally redundant in joining DNA breaks in a G1-arrested progenitor B-cell line." Proc Natl Acad Sci U S A. **2016**;113(38):10619-24

Kumar V, Alt FW, Oksenych V. "Functional overlaps between XLF and the ATM-dependent DNA double strand break response." DNA Repair. **2014**;17:52-63.

Lamarche BJ, Orazio NI, Weitzman MD. “The MRN complex in double-strand break repair and telomere maintenance.” FEBS letters. **2010**;584(17):3682-3695.

Lescale C, Abramowski V, Bedora-Faure M, Murigneux V, Vera G, Roth DB, Revy P, de Villartay JP, Deriano L. “RAG2 and XLF/Cernunnos interplay reveals a novel role for the RAG complex in DNA repair.” Nat Commun. **2016**;7:10529

Lescale C, Lenden Hasse H, Blackford AN, Balmus G, Bianchi JJ, Yu W, Bacoccina L, Jarade A, Clouin C, Sivapalan R, Reina-San-Martin B, Jackson SP, Deriano L. “Specific roles of XRCC4 paralogs PAXX and XLF during V(D)J recombination.” Cell Rep. **2016**;16(11):2967-2979.

Li G, Alt FW, Cheng HL, Brush JW, Goff PH, Murphy MM, Franco S, Zhang Y, Zha S. “Lymphocyte-specific compensation for XLF/cernunnos end-joining functions in V(D)J recombination.” Mol Cell. **2008**;31(5):631-40.

Li Y, Chirgadze DY, Bolanos-Garcia VM, Sibanda BL, Davies OR, Ahnesorg P, Jackson SP, Blundell TL. “Crystal structure of human XLF/Cernunnos reveals unexpected differences from XRCC4 with implications for NHEJ.” EMBO J. **2008**;27(1):290-300.

Li Z, Dordai DI, Lee J, Desiderio S. “A conserved degradation signal regulates RAG-2 accumulation during cell division and links V(D)J recombination to the cell cycle.” Immunity. **1996**;5(6):575-89.

Liao MJ, Van Dyke T. “Critical role for Atm in suppressing V(D)J recombination-driven thymic lymphoma.” Genes Dev. **1999**;13:1246–50.

Lieber MR. “The mechanism of double-strand DNA break repair by the nonhomologous DNA end-joining pathway.” Annu Rev Biochem. **2010**;79:181-211.

Liu P, Gan W, Guo C, Xie A, Gao D, Guo J, Zhang J, Willis N, Su A, Asara JM, Scully R, Wei W. “Akt-mediated phosphorylation of XLF impairs non-homologous end-joining DNA repair.” Mol Cell. **2015**;57(4):648-61.

Liu X, Jiang W, Dubois RL, Yamamoto K, Wolner Z, Zha S. “Overlapping functions between XLF repair protein and 53BP1 DNA damage response factor in end joining and lymphocyte development.” Proc Natl Acad Sci U S A. **2012**;109(10):3903-8.

Liu X, Shao Z, Jiang W, Lee BJ, Zha S. “PAXX promotes KU accumulation at DNA breaks and is essential for end-joining in XLF-deficient mice.” Nat Commun. **2017**;8:13816.

Liyanage M, Weaver Z, Barlow C, Coleman A, Pankratz DG, Anderson S, Wynshaw-Boris A, Ried T. “Abnormal rearrangement within the alpha/delta T-cell receptor locus in lymphomas from Atm-deficient mice.” Blood. **2000**;96:1940–6.

Lopes JL, Miles AJ, Whitmore L, Wallace BA. “Distinct circular dichroism spectroscopic signatures of polyproline II and unordered secondary structures: applications in secondary

structure analyses." Protein Sci. **2014**;23(12):1765-72.

Lou Z, Minter-Dykhouse K, Franco S, Gostissa M, Rivera MA, Celeste A, Manis JP, van Deursen J, Nussenzweig A, Paull TT, Alt FW, Chen J. "MDC1 maintains genomic stability by participating in the amplification of ATM-dependent DNA damage signals." Mol Cell. **2006**;21(2):187–200

Lu H, Pannicke U, Schwarz K, Lieber MR. "Length-dependent binding of human XLF to DNA and stimulation of XRCC4.DNA ligase IV activity." J Biol Chem. **2007**;282(15):11155-62.

Lu H, Shimazaki N, Raval P, Gu J, Watanabe G, Schwarz K, Swanson PC, Lieber MR. "A biochemically defined system for coding joint formation in V(D)J recombination." Mol Cell. **2008**;31(4):485-97.

Ma Y, Lu H, Tippin B, Goodman MF, Shimazaki N, Koiwai O, Hsieh CL, Schwarz K, Lieber MR. "A biochemically defined system for mammalian nonhomologous DNA end joining." Mol Cell. **2004**;16(5):701-13.

Ma Y, Pannicke U, Lu H, Niewolik D, Schwarz K, Lieber MR. "The DNA-dependent protein kinase catalytic subunit phosphorylation sites in human Artemis." J Biol Chem. **2005**;280(40):33839-46.

Ma Y, Pannicke U, Schwarz K, Lieber MR. "Hairpin opening and overhang processing by an Artemis/DNA-dependent protein kinase complex in nonhomologous end joining and V(D)J recombination." Cell. **2002**;108(6):781-94.

Manis JP, Morales JC, Xia Z, Kutok JL, Alt FW, Carpenter PB. "53BP1 links DNA damage-response pathways to immunoglobulin heavy chain class-switch recombination." Nat Immunol. **2004**;5(5):481-7.

Mao Z, Bozzella M, Seluanov A, Gorbunova V. "Comparison of nonhomologous end joining and homologous recombination in human cells." DNA Repair. **2008**;7(10):1765-71.

Matsuoka S, Ballif BA, Smogorzewska A, McDonald ER 3rd, Hurov KE, Luo J, Bakalarski CE, Zhao Z, Solimini N, Lerenthal Y, Shiloh Y, Gygi SP, Elledge SJ. "ATM and ATR substrate analysis reveals extensive protein networks responsive to DNA damage." Science. **2007**;316(5828):1160-6.

Menon V, Povirk LF. "XLF/Cernunnos: An important but puzzling participant in the nonhomologous end joining DNA repair pathway." DNA Repair. **2017**;58:29-37.

Mimitou EP, Symington LS. "Ku prevents Exo1 and Sgs1-dependent resection of DNA ends in the absence of a functional MRX complex or Sae2." EMBO J. **2010**;29(19):3358-69.

Morales AJ, Carrero JA, Hung PJ, Tubbs AT, Andrews JM, Edelson BT, Calderon B, Innes CL, Paules RS, Payton JE, Sleckman BP. "A type I IFN-dependent DNA damage response regulates the genetic program and inflammasome activation in macrophages." Elife. **2017**;6. pii: e24655.

Muljo SA, Schlissel MS. “A small molecule Abl kinase inhibitor induces differentiation of Abelson virus-transformed pre-B cell lines.” Nat Immunol. **2003**;4(1):31-7.

Neal JA, Dang V, Douglas P, Wold MS, Lees-Miller SP, Meek K. “Inhibition of homologous recombination by DNA-dependent protein kinase requires kinase activity, is titratable, and is modulated by autophosphorylation.” Mol Cell Biol. **2011**;31(8):1719-33.

Noon AT, Shibata A, Rief N, Lobrich M, Stewart GS, Jeggo PA, Goodarzi AA. “53BP1-dependent robust localized KAP-1 phosphorylation is essential for heterochromatic DNA double-strand break repair.” Nat. Cell Biol. **2010**;12:177–184.

Normanno D, Négrel A, de Melo AJ, Betzi S, Meek K, Modesti M. “Mutational phospho-mimicry reveals a regulatory role for the XRCC4 and XLF C-terminal tails in modulating DNA bridging during classical non-homologous end joining.” Elife. **2017**;6. pii: e22900.

Ochi T, Blackford AN, Coates J, Jhujh S, Mehmood S, Tamura N, Travers J, Wu Q, Draviam VM, Robinson CV, Blundell TL, Jackson SP. “PAXX, a paralog of XRCC4 and XLF, interacts with Ku to promote DNA double-strand break repair.” Science. **2015**;347(6218):185-188.

Oksenych V, Alt FW, Kumar V, Schwer B, Wesemann DR, Hansen E, Patel H, Su A, Guo C. “Functional redundancy between repair factor XLF and damage response mediator 53BP1 in V(D)J recombination and DNA repair.” Proc Natl Acad Sci U S A. **2012**;109(7):2455-60.

Oksenych V, Kumar V, Liu X, Guo C, Schwer B, Zha S, Alt FW. “Functional redundancy between the XLF and DNA-PKcs DNA repair factors in V(D)J recombination and nonhomologous DNA end joining.” Proc Natl Acad Sci U S A. **2013**;110(6):2234-9.

Pan-Hammarström Q, Jones AM, Lähdesmäki A, Zhou W, Gatti RA, Hammarström L, Gennery AR, Ehrenstein MR. “Impact of DNA ligase IV on nonhomologous end joining pathways during class switch recombination in human cells.” J Exp Med. **2005**;201(2):189-94.

Pascal BD, Willis S, Lauer JL, Landgraf RR, West GM, Marciano D, Novick S, Goswami D, Chalmers MJ, Griffin PR. “HDX workbench: software for the analysis of H/D exchange MS data.” J Am Soc Mass Spectrom. **2012**;23(9):1512-21.

Petiniot LK, Weaver Z, Barlow C, Shen R, Eckhaus M, Steinberg SM, Ried T, Wynshaw-Boris A, Hodes RJ. “Recombinase-activating gene (RAG) 2-mediated V(D)J recombination is not essential for tumorigenesis in Atm-deficient mice.” Proc Natl Acad Sci U S A. **2000**;97:6664–9.

Qian J, Wang Q, Dose M, Pruett N, Kieffer-Kwon KR, Resch W, Liang G, Tang Z, Mathé E, Benner C, Dubois W, Nelson S, Vian L, Oliveira TY, Jankovic M, Hakim O, Gazumyan A, Pavri R, Awasthi P, Song B, Liu G, Chen L, Zhu S, Feigenbaum L, Staudt L, Murre C, Ruan Y, Robbiani DF, Pan-Hammarström Q, Nussenzweig MC, Casellas R. “B cell super-enhancers and regulatory clusters recruit AID tumorigenic activity.” Cell. **2014**;159(7):1524-37.

Qiu JX, Kale SB, Yarnell Schultz H, Roth DB. “Separation-of-function mutants reveal critical roles for RAG2 in both the cleavage and joining steps of V(D)J recombination.” Mol Cell. **2001**;7(1):77-87.

Reginato G, Cannavo E, Cejka P. “Physiological protein blocks direct the Mre11–Rad50–Xrs2 and Sae2 nuclease complex to initiate DNA end resection.” Genes Dev. **2017**;31(23-24):2325-2330.

Reid DA, Keegan S, Leo-Macias A, Watanabe G, Strande NT, Chang HH, Oksuz BA, Fenyo D, Lieber MR, Ramsden DA, Rothenberg E. “Organization and dynamics of the nonhomologous end-joining machinery during DNA double-strand break repair.” Proc Natl Acad Sci U S A. **2015**;112(20):E2575-84.

Riballo E, Kühne M, Rief N, Doherty A, Smith GC, Recio MJ, Reis C, Dahm K, Fricke A, Krempler A, Parker AR, Jackson SP, Gennery A, Jeggo PA, Löbrich M. “A pathway of double-strand break rejoining dependent upon ATM, Artemis, and proteins locating to gamma-H2AX foci.” Mol Cell. **2004**;16(5):715-24.

Riballo E, Woodbine L, Stiff T, Walker SA, Goodarzi AA, Jeggo PA. “XLF-Cernunnos promotes DNA ligase IV-XRCC4 re-adenylation following ligation.” Nucleic Acids Res. **2009**;37(2):482-92.

Ribes-Zamora A, Indiviglio SM, Mihalek I, Williams CL, Bertuch AA. “TRF2 interaction with Ku heterotetramerization interface gives insight into c-NHEJ prevention at human telomeres.” Cell Rep. **2013**;5(1):194-206.

Rogakou EP, Pilch DR, Orr AH, Ivanova VS, Bonner WM. “DNA double-stranded breaks induce histone H2AX phosphorylation on serine 139.” J Biol Chem. **1998**;273(10):5858-68.

Rooney S, Sekiguchi J, Zhu C, Cheng HL, Manis J, Whitlow S, DeVido J, Foy D, Chaudhuri J, Lombard D, Alt FW. “Leaky Scid phenotype associated with defective V(D)J coding end processing in Artemis-deficient mice.” Mol Cell. **2002**;10(6):1379-90.

Ropars V, Drevet P, Legrand P, Baconnais S, Amram J, Faure G, Márquez JA, Piétrement O, Guerois R, Callebaut I, Le Cam E, Revy P, de Villartay JP, Charbonnier JB. “Structural characterization of filaments formed by human Xrcc4-Cernunnos/XLF complex involved in nonhomologous DNA end-joining.” Proc Natl Acad Sci U S A. **2011**;108(31):12663-8.

Roy R, Chun J, Powell SN. “BRCA1 and BRCA2: different roles in a common pathway of genome protection.” Nat Rev Cancer. **2011**;12(1):68-78.

Roy S, de Melo AJ, Xu Y, Tadi SK, Négrel A, Hendrickson E, Modesti M, Meek K. “XRCC4/XLF interaction is variably required for DNA repair and is not required for ligase IV stimulation.” Mol Cell Biol. **2015**;35(17):3017-28.

Samper E, Goytisolo FA, Slijepcevic P, van Buul PP, Blasco MA. “Mammalian Ku86 protein

prevents telomeric fusions independently of the length of TTAGGG repeats and the G-strand overhang." EMBO Rep. **2000**;1(3):244-52.

Savic V, Yin B, Maas N, Bredemeyer A, Carpenter A, Helmink B, Yang-Iott K, Sleckman B, Bassing C. "Formation of dynamic γ-H2AX domains along broken DNA strands is distinctly regulated by ATM and MDC1 and dependent upon H2AX densities in chromatin." Mol Cell. **2009**;34(3):298–310.

Sibanda BL, Critchlow SE, Begun J, Pei XY, Jackson SP, Blundell TL, Pellegrini L. "Crystal structure of an Xrcc4-DNA ligase IV complex." Nat Struct Biol. **2001**;8(12):1015-9.

Shao Z, Davis AJ, Fattah KR, So S, Sun J, Lee KJ, Harrison L, Yang J, Chen DJ. "Persistently bound Ku at DNA ends attenuates DNA end resection and homologous recombination." DNA Repair. **2012**;11(3):310-6.

Sheehan, K.C., Ruddle, N.H., and Schreiber, R.D. "Generation and characterization of hamster monoclonal antibodies that neutralize murine tumor necrosis factors." J Immunol. **1989**;142:3884-3893.

Skalka AM, Katz RA. "Retroviral DNA integration and the DNA damage response." Cell Death Differ. **2005**;12 Suppl 1:971-8.

Slavoff SA, Heo J, Budnik BA, Hanakahi LA, Saghatelian A. "A human short open reading frame (sORF)-encoded polypeptide that stimulates DNA end joining." J Biol Chem. **2014**;289(16):10950-7.

Smith JA, Bannister LA, Bhattacharjee V, Wang Y, Waldman BC, Waldman AS. "Accurate homologous recombination is a prominent double-strand break repair pathway in mammalian chromosomes and is modulated by mismatch repair protein Msh2." Mol Cell Biol. **2007**;27(22):7816-27.

Spagnolo L, Rivera-Calzada A, Pearl LH, Llorca O. "Three-dimensional structure of the human DNA-PKcs/Ku70/Ku80 complex assembled on DNA and its implications for DNA DSB repair." Mol Cell. **2006**;22(4):511-9.

Steen SB, Han JO, Mundy C, Oettinger MA, Roth DB. "Roles of the "dispensable" portions of RAG-1 and RAG-2 in V(D)J recombination." Mol Cell Biol. **1999**;19(4):3010-7.

Stewart GS, Wang B, Bignell CR, Taylor AM, Elledge SJ. "MDC1 is a mediator of the mammalian DNA damage checkpoint." Nature. **2003**;421(6926):961–966

Stucki M, Clapperton J, Mohammad D, Yaffe M, Smerdon S, Jackson S. "MDC1 directly binds phosphorylated histone H2AX to regulate cellular responses to DNA double-strand breaks." Cell. **2005**;123(7):1213–1226.

Symington, L.S. and Gautier, J. "Double-strand break end resection and repair pathway choice."

Annu. Rev. Genet. **2011**;45: 247–271.

Tadi SK, Tellier-Lebègue C, Nemoz C, Drevet P, Audebert S, Roy S, Meek K, Charbonnier JB, Modesti M. "PAXX Is an accessory c-NHEJ factor that associates with Ku70 and has overlapping functions with XLF." Cell Rep. **2016**;17(2):541-555.

Teng G, Maman Y, Resch W, Kim M, Yamane A, Qian J, Kieffer-Kwon KR, Mandal M, Ji Y, Meffre E, Clark MR, Cowell LG, Casellas R, Schatz DG. "RAG represents a widespread threat to the lymphocyte genome." Cell. **2015**;162(4):751-65.

Theunissen JW, Kaplan MI, Hunt PA, Williams BR, Ferguson DO, Alt FW, Petrini JH. "Checkpoint failure and chromosomal instability without lymphomagenesis in Mre11(ATLD1/ATLD1) mice." Mol Cell. **2003**;12(6):1511-23.

Timney BL, Raveh B, Mironska R, Trivedi JM, Kim SJ, Russel D, Wente SR, Sali A, Rout MP. "Simple rules for passive diffusion through the nuclear pore complex." J Cell Biol. **2016**;215(1):57-76.

Tsai CJ, Kim SA, Chu G. "Cernunnos/XLF promotes the ligation of mismatched and noncohesive DNA ends." Proc Natl Acad Sci U S A. **2007**;104(19):7851-6.

Tubbs AT, Dorsett Y, Chan E, Helmink B, Lee BS, Hung P, George R, Bredemeyer AL, Mittal A, Pappu RV, Chowdhury D, Mosammaparast N, Krangel MS, Sleckman BP. "KAP-1 promotes resection of broken DNA ends not protected by γ-H2AX and 53BP1 in G_1-phase lymphocytes." Mol Cell Biol. **2014**;34(15):2811-21.

Vera G, Rivera-Munoz P, Abramowski V, Malivert L, Lim A, Bole-Feysot C, Martin C, Florkin B, Latour S, Revy P, de Villartay JP. "Cernunnos deficiency reduces thymocyte life span and alters the T cell repertoire in mice and humans." Mol Cell Biol. **2013**;33(4):701-11.

Walker JR, Corpina RA, Goldberg J. "Structure of the Ku heterodimer bound to DNA and its implications for double-strand break repair." Nature. **2001**;412(6847):607-14.

Wang Y, Cortez D, Yazdi P, Neff N, Elledge SJ, Qin J. "BASC, a super complex of BRCA1-associated proteins involved in the recognition and repair of aberrant DNA structures." Genes Dev. **2000**;14(8):927-39.

Ward IM, Difilippantonio S, Minn K, Mueller MD, Molina JR, Yu X, Frisk CS, Ried T, Nussenzweig A, Chen J. "53BP1 cooperates with p53 and functions as a haploinsufficient tumor suppressor in mice." Mol Cell Biol. **2005**;25(22):10079-86.

Ward IM, Minn K, van Deursen J, Chen J. "p53 Binding protein 53BP1 is required for DNA damage responses and tumor suppression in mice." Mol Cell Biol. **2003**;23:2556–63.

Ward IM, Reina-San-Martin B, Olaru A, Minn K, Tamada K, Lau JS, Cascalho M, Chen L, Nussenzweig A, Livak F, Nussenzweig MC, Chen J. "53BP1 is required for class switch

recombination." J Cell Biol. **2004**;165(4):459-64.

Williams RS, Moncalian G, Williams JS, Yamada Y, Limbo O, Shin DS, Groocock LM, Cahill D, Hitomi C, Guenther G, Moiani D, Carney JP, Russell P, Tainer JA. "Mre11 dimers coordinate DNA end bridging and nuclease processing in double-strand-break repair." Cell. **2008**;135:97–109.

Wright PE, Dyson HJ. "Intrinsically disordered proteins in cellular signalling and regulation." Nat Rev Mol Cell Biol. **2015**;16(1):18-29.

Wu Q, Ochi T, Matak-Vinkovic D, Robinson CV, Chirgadze DY, Blundell TL. "Non-homologous end-joining partners in a helical dance: structural studies of XLF-XRCC4 interactions." Biochem Soc Trans. **2011**;39(5):1387-92, suppl 2 p following 1392.

Wu PY, Frit P, Malivert L, Revy P, Biard D, Salles B, Calsou P. "Interplay between Cernunnos-XLF and nonhomologous end-joining proteins at DNA ends in the cell." J Biol Chem. **2007**;282(44):31937-43.

Xiao Z, Dunn E, Singh K, Khan IS, Yannone SM, Cowan MJ. "A non-leaky Artemis-deficient mouse that accurately models the human severe combined immune deficiency phenotype, including resistance to hematopoietic stem cell transplantation." Biol Blood Marrow Transplant. **2009**;15(1):1-11.

Xing M, Yang M, Huo W, Feng F, Wei L, Jiang W, Ning S, Yan Z, Li W, Wang Q, Hou M, Dong C, Guo R, Gao G, Ji J, Zha S, Lan L, Liang H, Xu D. "Interactome analysis identifies a new paralogue of XRCC4 in non-homologous end joining DNA repair pathway." Nat Commun. **2015**;6:6233.

Xu B, Kim St, Kastan MB. "Involvement of Brca1 in S-phase and G(2)-phase checkpoints after ionizing irradiation." Mol Cell Biol. **2001**;21(10):3445-50.

Yan CT, Boboila C, Souza EK, Franco S, Hickernell TR, Murphy M, Gumaste S, Geyer M, Zarrin AA, Manis JP, Rajewsky K, Alt FW. "IgH class switching and translocations use a robust non-classical end-joining pathway." Nature. **2007**;449(7161):478-82.

Yano K, Morotomi-Yano K, Wang SY, Uematsu N, Lee KJ, Asaithamby A, Weterings E, Chen DJ. "Ku recruits XLF to DNA double-strand breaks" EMBO Rep. **2008**;9(1):91-6.

Yano K, Morotomi-Yano K, Lee KJ, Chen DJ. "Functional significance of the interaction with Ku in DNA double-strand break recognition of XLF." FEBS Lett. **2011**;585(6):841-6.

Yu Y, Mahaney BL, Yano K, Ye R, Fang S, Douglas P, Chen DJ, Lees-Miller SP. "DNA-PK and ATM phosphorylation sites in XLF/Cernunnos are not required for repair of DNA double strand breaks." DNA Repair. **2008**;7(10):1680-92.

Zha S, Alt FW, Cheng HL, Brush JW, Li G. "Defective DNA repair and increased genomic

instability in Cernunnos-XLF-deficient murine ES cells." Proc Natl Acad Sci U S A. **2007**;104(11):4518-23.

Zha S, Guo C, Boboila C, Oksenych V, Cheng HL, Zhang Y, Wesemann DR, Yuen G, Patel H, Goff PH, Dubois RL, Alt FW. "ATM damage response and XLF repair factor are functionally redundant in joining DNA breaks." Nature. **2011**;469(7329):250-4.

Zha S, Jiang W, Fujiwara Y, Patel H, Goff PH, Brush JW, Dubois RL, Alt FW. "Ataxia telangiectasia-mutated protein and DNA-dependent protein kinase have complementary V(D)J recombination functions." Proc Natl Acad Sci U S A. **2011**;108:2028–33.

Zhang Y, Hefferin ML, Chen L, Shim EY, Tseng HM, Kwon Y, Sung P, Lee SE, Tomkinson AE. "Role of Dnl4-Lif1 in nonhomologous end-joining repair complex assembly and suppression of homologous recombination." Nat Struct Mol Biol. **2007**;14(7):639-46.

Zhou Y, Lee JH, Jiang W, Crowe JL, Zha S, Paull TT. "Regulation of the DNA Damage Response by DNA-PKcs Inhibitory Phosphorylation of ATM." Mol Cell. **2017**;65(1):91-104.

Zhu C, Mills KD, Ferguson DO, Lee C, Manis J, Fleming J, Gao Y, Morton CC, Alt FW. "Unrepaired DNA breaks in p53-deficient cells lead to oncogenic gene amplification subsequent to translocations." Cell. **2002**;109(7):811-21.

Zierhut C, Diffley JF. "Break dosage, cell cycle stage and DNA replication influence DNA double strand break response." EMBO J. **2008**;27(13):1875-85.

Ziv Y, Bielopolski D, Galanty Y, Lukas C, Taya Y, Schultz DC, Lukas J, Bekker-Jensen S, Bartek J, Shiloh Y. "Chromatin relaxation in response to DNA double-strand breaks is modulated by a novel ATM- and KAP-1 dependent pathway." Nat. Cell Biol. **2006**;8:870–876.